Investigation of ion mass diagnostics for plasma processing

C. Hayden

January 23, 2009

Investigation of ion mass diagnostics for plasma processing

A thesis for the degree of

PHILOSOPHIAE DOCTOR

Presented to

DUBLIN CITY UNIVERSITY

By

Chanel Hayden
School of Physical Sciences
Dublin City University

Research Supervisors:
Dr. Mike B. Hopkins and
Prof. Miles M. Turner

External Examiner: Dr. Charles Mahony
Internal Examiner: Dr. Paul Swift

November 2008

Declaration

I hereby certify that this material which I now submit for assessment on the programme of study leading to the award of Philosophiae Doctor is entirely my own work, that I have exercised reasonable care to ensure that the work is original, and does not to the best of my knowledge breach any law of copyright, and has not been taken from the work of others save and to the extent that such work has been cited and acknowledged within the text of this work.

Signed:.....Candidate ID No.:.....

Chanel Hayden, 24th November 2008

Abstract

Plasma properties can be characterised with a multitude of diagnostic techniques which are as varied as the many industrial applications that employ them, from etching microchips to surface treatment and cleaning. A particular manufacturing technique may require a certain plasma characteristic at a given condition. In order to get the necessary properties, other characteristics must be fine tuned and monitored. In some cases there is an offset in the degree of control and what can be measured accurately without disturbing the overall process, thus the ability to monitor and control these parameters is crucial. Of these parameters, the plasma density, n_0, the electron temperature, T_e, the ion bombarding energy, E_i, and the ion current density, J_i, are the most important quantities for processing plasma applications. Monitoring plasma parameters is often difficult due to poor access or operating condition limitations and so there is an ever-increasing need for improved techniques. Electrical properties of plasmas can be measured relatively easily over a broad range of conditions however ion mass on the other hand is generally only measured using mass-spectrometry. A novel electrostatic probe, arranged so that a cylindrical probe is oriented normal to a planar probe with a retarding potential applied to the normal and a dc pulse to the other is investigated with a view to inferring ion mass. A Retarding Field Energy Analyser (RFEA) is used to investigate Ion Energy Distributions (IED's) and to indicate the average ion mass in gas mixtures. The goal of this thesis is to investigate methods for measuring mass and to use this as feedback for process control.

Acknowledgements

Above and beyond all others I would like to thank my supervisor Dr. Mike Hopkins aka *Mr Motivator*, whose encouragement and intuition brought my research to this stage. His guidance and never ending supply of ideas propelled me to reach my ultimate goal, and for that I am truly grateful. I would like to thank Dr. Bert Ellingboe and Professor Miles Turner for introducing me to plasma physics, for their direction in the early stages of my research and for giving me the opportunity to undertake an internship at Lam Research Corporation. This experience has proved to be invaluable. The BEOL diagnostics group at Lam took me under their wing and I would like to thank all those I worked with in particular, Eric Hudson, Doug Keil, Alexei Marakhtanov and Neil Benjamin.

I have also benefited greatly from many discussions with my fellow students past and present, Felipe, Derek, Angus, Shane, Peter, Taghrid, Niall, Cezar, Muhammad and Huw. I am also grateful to the administrative, technical and academic team in the NCPST, namely Samantha, Sarah, Sheila,

Trish, Des, Paul, Vic, Stuart, Ronan, Jim, James, Shantanu, Petar and Bernard. I must also mention Dr David Gahan whose kind encouraging nature and willingness to share his knowledge contributed greatly to my research.

Jen, and all those who have been involved with FOCAS DIT where I got my first taste of research, thank you. My final acknowledgements must go to Shane, my family and friends. Shane's inquisitive temperament kept me on the right track even when I didn't want to be on it. My parents, Noel and Deirdre, who have supported me for my whole life with unwavering confidence and encouragement. They have kept me on the path to achieving this goal. Thanks so much, you are the best!

Contents

List of Figures

LIST OF FIGURES

LIST OF FIGURES

List of symbols

A	area (m^{-2})
d	distance (m)
D	diffusion coefficient (m^2s^{-1}); D_a ambipolar diffusion coefficient; drift energy flux (Wm^{-2})
e	absolute electron charge ($\simeq 1.6 \times 10^{19}$ C)
E	electric field (Vm^{-1}); energy (J or eV)
f	frequency (Hz); distribution function ($m^{-2}s$)
H	magnetic field strength (Am^{-1})
I	current (A)
j	$(-1)^{1/2}$
J	current density (Am^{-2})
k	Boltzmann's constant ($\simeq 1.381 \times 10^{-23}$ JK^{-1})
l	length (m)

continued on next page

continued from previous page

m	mass (kg); m_e electron mass ($\simeq 9.1 \times 10^{-31}$ kg); m_i ion mass
n	particle number density (m^{-3}); n_e electron density; n_i ion density; n_g neutral gas density
P	power (W)
p	pressure (Torr)
q	electric charge (C)
Q	heat flux (Wm^{-2})
s	sheath position (m)
S	energy flux (Wm^{-2})
t	time (s)
T	temperature (K or Volts)
u	velocity (ms^{-1}); average velocity; u_B Bohm velocity
v	velocity (ms^{-1})
V	electric potential (V)
$\mathcal{W}$	super-particle weighting factor
x	rectangular coordinate
Γ	particle flux ($\mathrm{m}^{-2}\mathrm{s}^{-1}$)
δ	Dirac delta function; small quantity
Δ	Δt PIC timestep; Δx PIC cell size
ϵ_0	vacuum permittivity ($\simeq 8.8 \times 10^{-12}$ Fm^{-1})
ζ	small displacement (m)
η	normalized potential
θ	angle (rad)
λ	mean free path (m); λ_i ion mean free path; λ_D electron Debye length (m)

continued on next page

continued from previous page

μ_0	permeability of free space ($4\pi \times 10^{-7}\mathrm{Hm}^{-1}$)
ν	collision frequency (Hz)
ρ	charge density (Cm^{-3})
σ	cross section (m^{-2}); electrical conductivity ($\Omega^{-1}\mathrm{m}^{-1}$)
τ	normalized temperature
ϕ	angle (rad)
Φ	potential (V)
ω	angular frequency (rad s^{-1}); ω_{pe} electron plasma frequency; ω_{pi} ion plasma frequency

CHAPTER 1

Introduction

Plasma (the 'fourth state of matter') was formally recognised by Crookes in 1879 [1] when he observed the behaviour of electrified gases in evacuated glass tubes. Plasmas are formed when electrons accelerated in electric fields collide with neutral gas atoms resulting in excitation and ionisation. The term 'plasma' can be attributed to Irving Langmuir who along with Tonks and Mott-Smith [2], conducted vigourous investigations of ionised gases and developed the first electrostatic probe, now known as the Langmuir probe. Since then, plasma properties have been characterised with a myriad of diagnostic techniques which are as varied as the many industrial applications that employ them, from etching microchips to surface treatments and cleaning.

The aim of this thesis is to investigate methods of determining plasma-generated ion species of different mass. Detection of ion species is important in plasma processing as it is the flux and bombardment energy of ions that

determine the effectiveness of a particular process [3]. Plasmas provide energy to either sputter or chemically activate surface reactions and so can be used for etching, surface activation/modification, cleaning or in the case of contact lenses, deposition of optical coatings.

In order to get the desired properties from a particular process, the plasma can be tuned, usually by varying power, pressure, gas flow rate, radio-frequency (rf) or dc bias to a substrate. The most important plasma parameters are density n_e, electron temperature T_e, ion mass m_i, ion energy ε_i and ion flux Γ_i. Most of these parameters can be measured, to varying degrees of accuracy, with electrostatic probes and numerous optical techniques. Mass however, cannot be measured with standard electrostatic probes and is generally measured with a dedicated mass spectrometer. Mass spectrometers are large complex instruments that are costly and often difficult to install in many industrial situations. These are described in more detail in chapter 2. The ability to measure an accurate mass-spectrum of a plasma is very advantageous, and so, the goal of this thesis is to investigate simpler methods of determining ion mass.

1.1 Thesis structure

This thesis begins with an introduction to rf discharges and some basic fundamentals of plasma physics. The diagnostics used to characterise the plasma are briefly described, as are the models. In the second chapter, a mass spectrometer system is connected to a re-entrant type inductive reactor to investigate its use in real-time plasma process control. Further to the outcome of that investigation, alternative diagnostics were investigated. Chapter 3 describes the experimental setup used for the remainder of the thesis. Chapter

4 describes an alternative diagnostic to the mass spectrometer - the Ion Mass Probe (IMP). This probe was designed, constructed and tested. Results were compared with computer simulations. In chapter 5 experiments with a Retarding Field Energy Analyser (RFEA) are reported. Models of ion energy distributions (IEDs) are described and compared with experimental results. Finally, the last chapter summarises this thesis with any conclusions drawn and suggestions for future work.

1.2 Radio frequency (rf) discharges

Plasmas can be produced by a variety of methods, however, for low-temperature plasma processing, capacitive and inductive radio-frequency (rf) power sources are predominantly used. In both cases, various frequencies can be applied typically in the range of 2 - 60 MHz including dual frequency or multiple-frequency systems depending on the particular application. However, some commercial systems employ frequencies much higher than this. The advantage of multi-frequency sources is that plasma density and ion energy can be controlled separately [4].

1.2.1 Capacitive coupled plasmas (CCPs)

The capacitive discharge configuration consists of two electrodes separated by a finite distance within a vacuum chamber. An rf voltage is applied between the two electrodes resulting in excitation and ionisation of the gas with electrons being accelerated by the rf field causing a current to flow through the plasma [5]. A typical CCP arrangement is shown in figure 1.1. At high frequencies the wavelength of the signal affects power transmission so 50 Ω coaxial cables are used in conjunction with a variable impedance

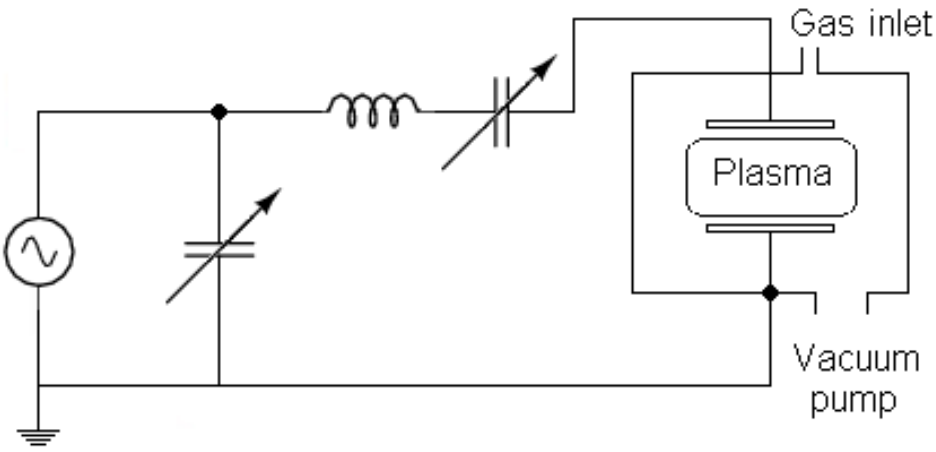

Figure 1.1: *A capacitively coupled plasma (CCP) reactor.*

match box to maximise the power transferred from the source to the plasma. The discharge impedance depends on the type of gas, pressure and power, hence the match box impedance must be variable. The rf source is usually 50 Ω, so, the matchbox attempts to make the load, i.e. the plasma, appear as a 50 Ω impedance. This enables maximum power transfer between the rf source and plasma.

1.2.2 Inductively coupled plasmas (ICPs)

In an inductive discharge, rf power is coupled to the plasma through a dielectric by way of an induction coil. The antenna coil can be arranged in a planar spiral or helical manner. A schematic of the ICP configuration used in this work is given in figure 1.2. When a time-varying electric current passes through the antenna, a time varying magnetic field is created which penetrates the dielectric window and in turn induces an azimuthal electric field in the plasma according to Faraday's law

$$\nabla \times E = -\mu_0 \frac{\partial H}{\partial t} \tag{1.1}$$

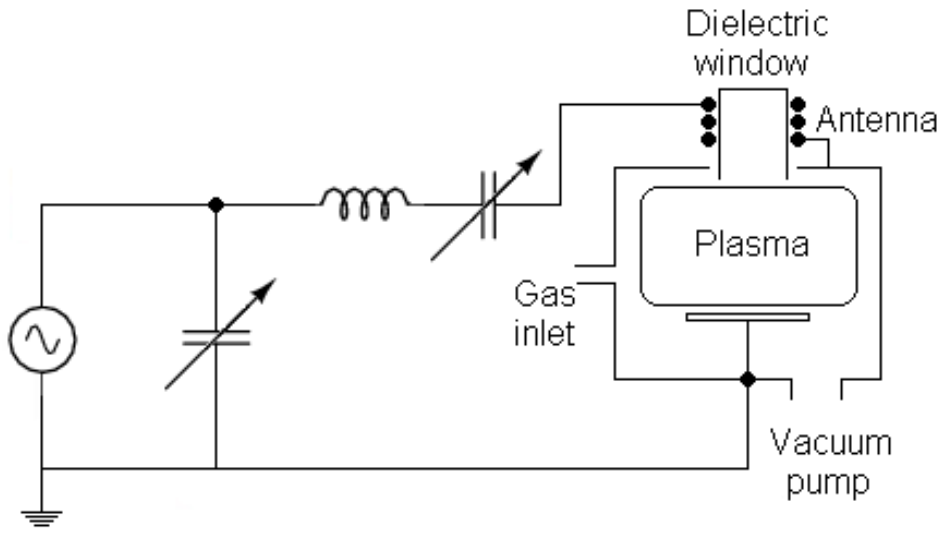

Figure 1.2: *An inductively coupled plasma (ICP) reactor.*

where μ_0 is the permeability of free space, and E and H are the electric and magnetic field vectors respectively. The electrons are accelerated to energies above the ionisation potential resulting in break down of the background gas [6].

Inductive discharges have the advantage that higher plasma densities can be achieved at lower pressure compared to capacitive discharges. At low densities the antenna acts as an electrode and the discharge is initially triggered in capacitive mode as a result of the high antenna voltage. As the plasma density reaches a sufficient level the power coupling switches to the inductive mode.

1.3 Rf sheaths

Sheaths are thin positively charged layers that form the boundary between a plasma and the walls of the vessel it occupies or any electrode/probe in

contact with the plasma [7]. As electrons have a higher mobility than ions, they are rapidly lost to the walls and this initial loss of electrons results in a positive space charge in the bulk. This produces an electric field which points from the plasma to the walls. As a result, electrons are reflected back to the plasma and conversely ions are accelerated to the surface. The sheath region continues to grow until equilibrium is reached and the electron and ion fluxes are balanced. Electrons respond to electric fields produced by the rf driving voltage V_{rf} while the ions, being heavier, can only respond to the time-averaged E-fields [7]. This creates a sheath region in the vicinity of each electrode which holds a net positive charge when averaged over the oscillation period. The sheath voltage may be written as

$$V(t) = \bar{V} + V_{rf} sin(\omega_{rf} t) \tag{1.2}$$

where V_{rf} is the amplitude of the ac signal and $\bar{V}$ is the average voltage. For a small fraction of the rf cycle where the sheath voltage is low enough, electrons can escape and reach the electrode resulting in rectification of the ac signal so that $\bar{V} \approx V_{rf}$. When an electrode is driven with an rf voltage, the sheath front oscillates in time. Ions only respond to the time averaged electric field while the electrons oscillate in phase with the sheath edge. This leads to alternate compression and decompression of electrons resulting in electron heating. A thorough mathematical description of the rf sheath is given by Lieberman in reference [8]. This is an important heating mechanism in low pressure plasmas [9].

1.4 Plasma diagnostics

Arguably the most common plasma diagnostic tool is the Langmuir probe. Langmuir probes can be made in various shapes, such as planar, spherical

and cylindrical. Cylindrical probe tips are most common as they are the easiest to construct and many detailed probe theories have been developed for this configuration. Many other types of electrostatic probes exist, such as: emissive probes, double probes etc. Many of these were essentially designed to overcome difficulties involved with Langmuir probe measurements in oscillating plasmas. Aside from electrostatic probes, there are numerous optical diagnostics such as Laser Induced Fluorescence (LIF), Optical Emission Spectroscopy (OES), absorption spectroscopy as well as non-optical techniques like microwave interferometry. These have the advantage of being non-invasive but are experimentally sensitive, expensive and more difficult to set-up. A detailed knowledge of collisional cross-sections and energy states of the species under investigation is often required for these techniques to be effective.

Planar and cylindrical electrostatic probes are important in the context of this thesis, as understanding the theory of their operation leads to a more detailed understanding of the IMP, described in chapter 4, and also the RFEA described in chapter 5, both of which are essentially electrostatic probes.

1.5 Electrostatic probes - the Langmuir probe

Of the many diagnostics used for measuring plasma parameters, the *Langmuir* probe is undoubtedly the easiest to implement. Its construction is relatively simple, comprising a small conducting electrode (usually made of a high melting point conductor such as tungsten or molybdenum) in contact with the plasma at one end and driven by an external voltage source at the other. By varying the applied dc bias through a low impedance resistor and recording the collected current, a current-voltage (I-V) trace (figure 1.3) can

be generated. From the I-V characteristic a number of important plasma parameters may be obtained such as the ion and electron currents $I_{i,e}$, time-averaged plasma potential, $\overline{\Phi}_p$, ion and electron densities, $n_{i,e}$, electron temperature, T_e, as well as the electron and ion energy distribution functions, EEDF and IEDF, respectively. One of the few important parameters that the Langmuir probe cannot measure, is ion mass. A possible solution to this is investigated in chapter 4.

There are three main sections to the I-V trace as shown in figure 1.3, these are the ion saturation, transition and electron saturation regions. These regions will be described in detail below but first the theories used to interpret the I-V characteristic will be addressed.

1.5.1 Probe theory

Langmuir and Mott-Smith were the first to develop a basic theory for relating the I-V characteristic to the plasma parameters [2]. A simple approach to probe theory may be taken under the following assumptions;

- a Maxwell-Boltzmann electron velocity distribution is assumed,
- plasma perturbations by the probe can be neglected and
- it is assumed that every particle that enters the sheath is collected by the probe.

Under these conditions, the total current, I, in the electron retarding region of the I-V curve, i.e. below the plasma potential, is given by

$$I = -I_i + I_{e_{sat}} exp\left(- \frac{\Phi_p - V_{bias}}{T_e} \right) \tag{1.3}$$

where I_i is the constant ion current and the negative sign indicates positive ion collection. $I_{e_{sat}}$ is the saturation electron current which decreases expo-

nentially for sheath voltage, $V_{sh} < 0$, where $V_{sh} = \Phi_p - V_{bias}$. T_e is in electron volts.

For an ideal planar probe, whose sheath width expands with sheath voltage, but sheath area remains constant, the collection area of the probe does not change throughout the I-V characteristic, and so, the electron and ion saturation currents are given respectively by,

$$I_{e_{sat}} = \frac{1}{4} e n_o A_p \overline{v}_e \tag{1.4}$$

and

$$I_{i_{sat}} = -e n_s A_p v_B \tag{1.5}$$

where A_p is the probe collection area, n_o is the plasma density ($n_o = n_e = n_i$), n_s is the sheath edge density, which is approximately 0.61 times n_o [7]. $\overline{v}_e$ is the average thermal velocity of the electrons ($= \sqrt{8eT_e/\pi m_e}$). v_B is the Bohm velocity, given by,

$$v_B = \sqrt{\frac{eT_e}{m_i}} \tag{1.6}$$

where, m_i is the ion mass, T_e is in eV.

Equation 1.6 is valid for $T_i << T_e$. The sheath edge is often defined as the point at which the ions reach v_B, after gaining energy in the presheath. n_e must always be less than n_i within the sheath (in order for the positive space charge to exist) so the ion energy gain in the presheath is necessary in order for the current fluxes to balance.

Equation 1.3 shows that the total current collected by the probe is a combination of ion and electron current. For $V_{bias} < \Phi_p$, the ion current to the probe is essentially constant (so $I_{i_{sat}} = I_i$). When $V_{sh} > 0$, i.e. when the bias voltage goes above the plasma potential, the electron current is no longer an exponential function of voltage as it begins to saturate. The current above Φ_p is thus given by equation 1.4.

Equations 1.4 and 1.5 are only valid for an ideal planar probe, whose sheath width varies as a function of bias, but collection area remains constant. Most probes for plasma research are cylindrical in nature, due to their simplicity of construction and reduced perturbation compared to planar probes [10]. In reality, the planar sheath tends to take on a hemispherical shape at large voltages [10], thus causing non-ideal results. For cylindrical probes, the collection area is a function of sheath voltage. As the collection area grows with bias, the current tends not to saturate as it does in the ideal planar case, but instead, increases approximately as a square-root dependance on V_{sh}. The effective collection area of a cylindrical probe, A_{eff}, is given by,

$$A_{eff} = A_p\left[1+\left(\frac{d_{sh}}{p_r}\right)\right] \tag{1.7}$$

where A_p is the probe tip area, p_r is the probe tip radius and d_{sh} is the sheath width given by Child's law [7],

$$d_{sh} = \frac{\sqrt{2}}{3}\lambda_D\left(\frac{2V_{sh}}{T_e}\right)^{\frac{3}{4}} \tag{1.8}$$

where λ_d, the Debye length, is given as $(\epsilon_o T_e/en_s)$ and n_s is sheath edge density.

The fact that the sheath expands with V_{sh} is a good demonstration of the collective behaviour of plasmas, as the sheath changes to shield out the increasing electric field from reaching the quasi-neutral bulk plasma. Equations 1.4 and 1.5 need to be modified for cylindrical probes so that sheath expansion is taken into account.

For large negative biases, equation 1.8 is valid, so when used in combination with 1.7 and substituted into 1.5, an approximate value for the incomplete ion saturation could be obtained. However, a more valid equa-

tion to use is that of Laframboise [11], which has been parameterised by Steinbrüchel [12] as,

$$I_i = en_i A_p \sqrt{\frac{eT_e}{2\pi m_i}} \left[a \left(\frac{e(\Phi_p - V_{bias})}{T_e} \right)^b \right] \tag{1.9}$$

The term in square brackets is essentially a correction factor to the saturation ion current, where the values a and b depend on the ratio of r_p/λ_D. For cylindrical probes, with $r_p/\lambda_D < 3$, a and b can be approximated by 1.13 and 0.5 respectively [10].

Equation 1.9 gives the orbital motion limited ion current to a cylindrical probe in a collisionless, Maxwellian plasma. Orbital motion limited(OML) theory, was originally developed by Langmuir and Mott-Smith [2] to take account of the fact that for cylindrical probes, ions entering the sheath with a particular angular momentum may actually miss the probe, even-though they are attracted to it. The effects of collisions are ignored. A sheath is generally considered collisionless if the sheath thickness, Δd_{sh} (= d_{sh} - r_p) is less than the mean free paths of either ions, λ_i, or electrons, λ_e.

Laframboise [11] extended this model and provides an exact numerical solution to the equations governing ion collection in collisionless sheaths. However, this theory is known [10, 13, 14] to overestimate ion densities even in the presence of very weak collisionality (mainly due to destruction of ion orbits) and therefore gives an upper limit to the collected ion current in the low pressure regime.

The electron collection is not affected by collisions to the same extent, due to the higher mobility of the electrons and the fact that electron current collection occurs near the plasma potential where the sheath width is smaller, and so, suffers less from sheath expansion effects.

Equation 1.10 gives the electron saturation, where again, the terms in brackets represent a correction factor for the sheath expansion and the coefficients β and γ depend on the ratio r_p/λ_D.

$$I_e = en_e A_p \sqrt{\frac{eT_e}{2\pi m_e}} \left[\beta \left(\frac{e(\Phi_p - V_{bias})}{T_e} + 1 \right)^{\gamma} \right] \tag{1.10}$$

Recent work by Pletnev and Laframboise [15] shows that as long as the probe potential does not exceed 40 V positive or negative, collisionless theory is valid for electron current measurements over a wide range of densities [10, 13, 14]. For the ion currents to be correctly determined from collisionless theory, the pressure must be below about 2.67 Pa and have sufficiently high plasma density. In all other cases, collisional effects must be included for greater accuracy.

Thus, as shown, the seemingly simple electrostatic probe requires quite a detailed theory, which is still far from perfect even after more than 80 years of research.

1.5.2 I-V characteristic

Figure 1.3 shows the I-V characteristic of an ideal planar probe and also, the more typical, non-ideal characteristic of a cylindrical probe.

When the probe is biased negatively with respect to the plasma potential, positive ions are attracted and electrons are repelled. For a perfect planar probe, where collection area is not a function of bias voltage, the ion current is essentially constant for $V_{bias} < V_{plasma}$.

At large negative potentials, ion current dominates as electrons do not have sufficient energy to cross the sheath and be collected on the probe. Ion saturation occurs when a further increase in negative potential does not

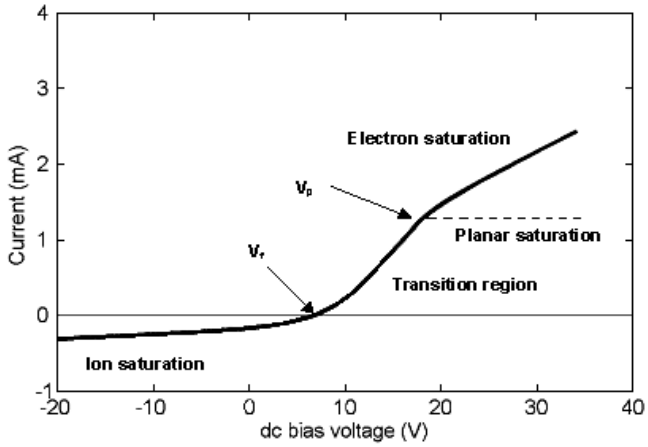

Figure 1.3: *A typical Current-Voltage (IV) characteristic for electrostatic probes*

increase the collected current. In practice, even for planar probes, saturation is rarely seen due to edge effects and also hemispherical distortion of the sheath edge as a function of bias voltage. Guard rings are often used to reduce edge effects, thus allowing planar probes to produce I-V characteristics with more complete saturation regions. Great care is needed in their construction to ensure this experimentally.

For cylindrical probes, collection area changes as a function of bias voltage due to sheath area expansion. Because the sheath area approximately equals the effective collection area of the probe, it acts as though the probe tip dimensions are varying as a function of bias. Hence, as saturation is approached more current is collected, and so, incomplete saturation occurs.

Using ion saturation current, $I_{i_{sat}}$, we can estimate the ion density, from equation (1.5), assuming we know T_e and m_i. From ion saturation, if the bias voltage is gradually made more positive with respect to the plasma potential, V_p, the sheath voltage reduces ($V_{sh} = V_p$ - V_{bias}). With a lower sheath potential, more and more electrons will have enough thermal velocity

to penetrate the sheath completely and get collected by the probe. At some point in bias the majority of electrons entering the sheath will make it to the probe. Ions are still being collected at approximately the same rate as in ion saturation but their signal is now swamped by the larger electron current. The exponential region can be used to calculate the mean electron temperature. This is done by first subtracting $I_{i_{sat}}$ from the total measured current to reveal only electron current. A semi-log plot of electron current versus bias voltage yields a straight line in the electron retardation region (assuming a Maxwellian distribution). The inverse of the slope of this line gives T_e in electron volts (eV). The calculated value of T_e is very sensitive to the exact shape of the exponential region and this can be affected by non-Maxwellian distributions or time-averaging effects [16].

As the bias voltage approaches the plasma potential, the sheath voltage approaches zero. At $V_{bias} = V_p$, the probe is at the same potential as the plasma, so no sheath forms (at least in a dc plasma). The collection area then becomes that of the probe tip. Because there is no sheath, electrons and ions are neither attracted nor repelled, they simply collide randomly against the probe tip. Again, because of the higher thermal velocity of the electrons, it is I_e that dominates. As the bias is increased further, the probe becomes positive with respect to the plasma and electrons are attracted while ions are repelled. Equation 1.10 can be used to calculate the saturation electron current as a function of bias in this region.

The transition from exponential to the $I_{e_{sat}}$ region also marks the position of the plasma potential. This is usually seen as a 'knee' in the I-V curve. V_p is determined by a linear extrapolation from the electron saturation region and an extrapolation from the exponential region. The bias point at which the linear extrapolations cross is V_p [7]. It can also be identified by the peak

of the first derivative, or the zero crossing point of the second derivative of the I-V characteristic. In a dc plasma, the knee can be quite distinctive and V_p can be determined accurately, however, in an rf plasma this is generally not the case due to time-averaged distortion issues.

Obtaining the second derivative is also useful for calculating the electron energy distribution function, EEDF, given by the Druyvesteyn equation [7, 17]

$$g_e(V) = \frac{2m}{e^2 A}\left(\frac{2eV}{m}\right)^{1/2}\frac{d^2 I_e}{dV^2} \tag{1.11}$$

V_p is given by the point at which the second derivative of I_e is equal to zero. The electron energy probability function (EEPF) is

$$g_p(\varepsilon) = \varepsilon^{-1/2} g_e(\varepsilon). \tag{1.12}$$

The integral of the EEDF gives n_e,

$$n_e = \int_0^\infty g_e(\varepsilon)d\varepsilon \tag{1.13}$$

and this in turn can be used to calculate the effective electron temperature, T_{eff} from

$$\langle\varepsilon\rangle = \frac{\int_0^\infty \varepsilon g_e(\varepsilon)d\varepsilon}{n_e} = \frac{3}{2}kT_e \tag{1.14}$$

which gives T_{eff} as

$$T_{eff} = \frac{1}{n_e}\frac{2}{3}\int_0^\infty \varepsilon g_e(\varepsilon)d\varepsilon. \tag{1.15}$$

The EEDF method of calculating plasma parameters is often assumed to be the most accurate method [13, 18], but it requires V_p to be known accurately, which may be difficult to determine from the I-V characteristic in the presence of oscillating currents (explained further in section 1.5.3).

The ion energy distribution, IEDF, is also an important parameter, especially for plasma etch processes where ion energy at the surface of the substrate is extremely important. A technique for measuring accurate IEDF's is explained in detail in chapter 5.

1.5.3 Time-averaged distortion and compensated probes

In a rf plasma, the sheath voltage essentially oscillates with the plasma potential and therefore, rf currents are also generated. The probe experiences many rf cycles at each dc bias point in the I-V characteristic but only time-averaged values are recorded. Due to the non-linear nature of the sheath, the time-averaged current does not equal the dc current. The measured trace is thus distorted by the oscillation. The distortion factor increases with the ratio ($\sim V_{p_{rf}}/T_e$) [19]. The distortion is generally negligible when the ratio is less than unity, at least for calculation of T_e from the semi-log plot of current versus bias voltage (see figure 1.4 [16]).

So called 'rf compensation' techniques can be applied to the probe to alleviate the issue of time-averaged distortion in oscillating plasmas. Gagne and Cantin [20] were the first to show how compensation could be achieved with the use of high impedance inductors. The idea is to create a rf voltage divider between the sheath and the inductors. The oscillating voltage drops across both, in a ratio that depends on the ratio of the impedances. If the inductor impedance is much greater than the sheath impedance then most of the voltage drops on the inductors, which means the sheath oscillates to a smaller extent, and so, the distortion current is reduced. Chen [21], and Godyak [22] show that the conditions for sufficient compensation are:

$$\mid \frac{Z_{sh}}{Z_{circuit}} \mid < (0.3 - 0.5)\frac{T_e}{V_{p_{rf}}} \tag{1.16}$$

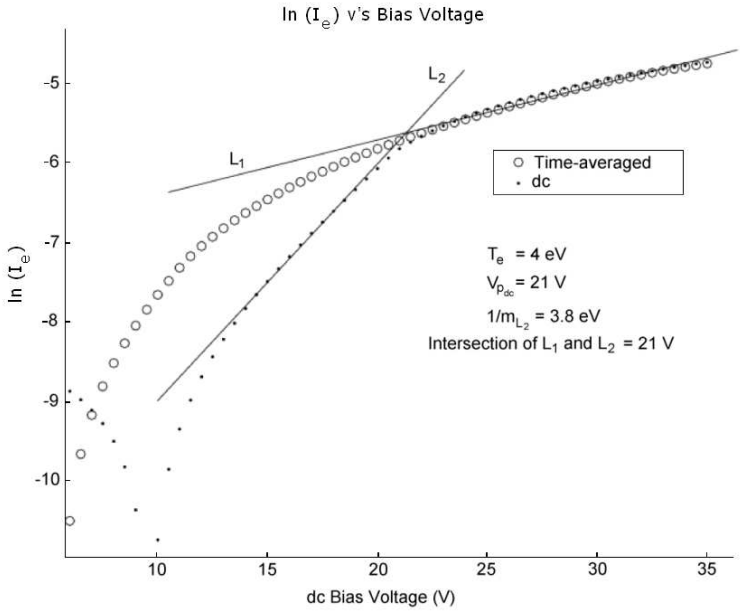

Figure 1.4: *Simulated T_e measurement with DC Characteristic. The time-averaged trace is shown for comparison. L_1 and L_2 are linear fits. The DC trace yields the correct dc plasma potential and approximately correct T_e values, whereas the same procedure on the time-averaged trace would return a serious error on both measurements.*

where $Z_{circuit}$ is the total impedance of the probe and circuitry combined, this includes Z_L and any stray capacitances.

Using this equation, with $T_e = 4$ eV, $V_{p_{rf}} = 20$ V, the circuit impedance must be approximately 32 times the sheath impedance. Assuming a sheath impedance which is dominated by a 1 pf capacitance, $Z_{circuit}$ must exceed about 380 kΩ at 13.56 MHz [16]. Achieving this requires great care and careful selection of appropriate inductors. Generally, high impedances, high Q-factor, self-resonant inductors are used [23–25].

To alleviate the requirements on the inductors, compensation electrodes may also be used. These are essentially large-area conductors ac coupled to

the probe tip. They do not add to the measured dc probe current but simply act to reduce the sheath capacitance, and therefore, sheath impedance. This makes the criteria for satisfactory compensation easier to achieve.

Compensation techniques identical to those used on Langmuir probes were also used on the RFEA in order to reduce the distortion caused by oscillating currents on the IEDF measurements. This will be explained further in chapter 5.

1.6 Summary

The important concepts relevant to the work in this thesis have been presented. A detailed description of Langmuir probes has been given in order to simplify the understanding of the probes developed in chapters 4 and 5. The IMP, described in chapter 4, is based on a combination of planar and cylindrical Langmuir probes and attempts to measure mass - one of the few important plasma parameters which a standard Langmuir probe cannot measure. This is described in detail in the chapter 4. Compensation techniques have been discussed. This is particularly relevant to the RFEA device in chapter 5, which also uses rf compensation to avoid errors in the IEDF measurements. This will be explained further in chapter 5.

CHAPTER 2

Mass Spectrometry and process control

In this chapter, 'real-time' process control of plasma parameters in the BARIS inductive reactor are investigated in an Ar-O_2 plasma. Process control is the dynamic modification of a process based on the results of process monitoring [26]. In essence, it is a quality control procedure in which sampling is done during the transformation process to achieve the desired performance specifications. This is critical in optimising a manufacturing process. However, real-time process control is extremely difficult to implement due to the complexity of industrial plasma systems [27] (real-time control will be described further in section 2.3). The feasibility of diagnostics such as a mass spectrometer and Langmuir probe are analysed for control of specific plasma parameters, namely, ion flux and atomic oxygen density, in a simple laboratory plasma.

Gas phase compounds can be analysed using a technique known as mass-

spectrometry. In 1912, J.J. Thompson built a spectrometer called the *positive ray parabola*, with this device, he obtained mass spectra for a number of species and also discovered metastables [28]. Around this time Thomson began working with Francis Aston to refine the experimental technique of gas phase analysis. Circa 1919, Aston developed a new improved apparatus called a *mass spectrograph*.

Essentially what a mass-spectrometer does is ionise neutral molecules in the gas phase, separate the ions according to their mass-to-charge ratios (m/z) and subsequently record any ions that reach the detector [29].

Analogue signals taken from a mass spectrometer are used as output variables to a process control algorithm with rf power and gas flow rate as the input variables. This control system monitors the mass spectrometer signals and ion flux measured with a Langmuir probe while simultaneously adjusting pressure, flow-rate and ICP power. The results and feasibility of such a system will be discussed.

2.1 Theoretical background

Most mass spectrometers require a differential pumping system to allow ions reach the detector without undergoing collisions. Firstly, the sample under investigation must be introduced to the mass spectrometer system via a suitable inlet aperture. This acts as the interface between the gas phase compounds and the ion source of the spectrometer. From here it travels to the source chamber where it is ionised by an electron beam produced by a hot filament, that is, by electron impact ionisation given by

$$M + e = M^+ + 2e \tag{2.1}$$

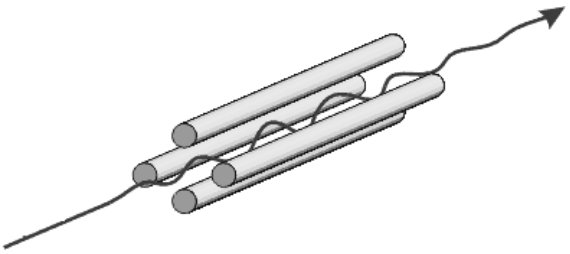

Figure 2.1: *An ions trajectory traversing between rf biased quadrupole rods.*

where M and M^+ represent the molecule and molecular ion respectively. An analyser then separates the ions according to their mass and a detector counts the number of ions coming from the analyser.

Since Thomsons' work began at the turn of the twentieth century many developments have been made and mass analysers are now available in several forms, namely: quadrupole; time-of-flight; magnetic; electromagnetic; ion cyclotron resonance and fourier transform analysers. For the purpose of this project, only the quadrupole mass spectrometer (QMS) will be explained in detail as it is this system that is used for process control of atomic oxygen density.

A quadrupole consists of four cylindrical or hyperbolic metal rods arranged in a parallel manner. These rods are electrically connected in opposing pairs.

A radio-frequency (rf) potential, $V\cos\omega t$, is applied to opposite pairs of rods and a dc voltage, U, is superimposed on the rf voltage as given by equation 2.2. Ions traverse down the quadrupole in between the rods. An ion with a positive charge moving between the rods will be attracted to a negative rod until the potential switches sign and causes the ion to change direction. The potential, Φ_0 on the rods is given by:

$$\Phi_0 = U - V\cos\omega t \text{ and } -\Phi_0 = -U + V\cos\omega t \tag{2.2}$$

where U is the dc potential, V is the zero-to-peak amplitude of the rf voltage, ω is the angular frequency in rads^{-1} = $2\pi f$ and f is the rf frequency. As the ion traverses along the z-axis, it will oscillate between the rods with the alternating voltage until it emerges at the other end (see figure 2.1). Only ions of a particular m/z will reach the detector for a specific ratio of voltages. Ions that have unstable trajectories will collide with the rods and be lost. Thus ion selection is possible by varying the applied potentials [28].

Any ions passing through the analyser will be recorded when they hit the detector. The signal produced in the detector during a scan is recorded as a function of m/z to produce a mass spectrum. In the instrument discussed here, a Faraday cup detector was used as the number of ions leaving the mass analyser is typically quite small, amplification is often necessary to get an adequate signal.

For optimum operation of a mass spectrometer the pressure must be sufficiently low to ensure collisions with other molecules are kept to a minimum and the mean free path of a charged particle is greater than the distance between ionisation and detection. The mean free path, λ is given by

$$\lambda = \frac{kT}{\sqrt{2}p\sigma} \tag{2.3}$$

where T is the temperature, p is the pressure and σ is the collision cross-section; σ=πd^2, where d is the sum of the radii of the stationary molecule and the colliding ion.

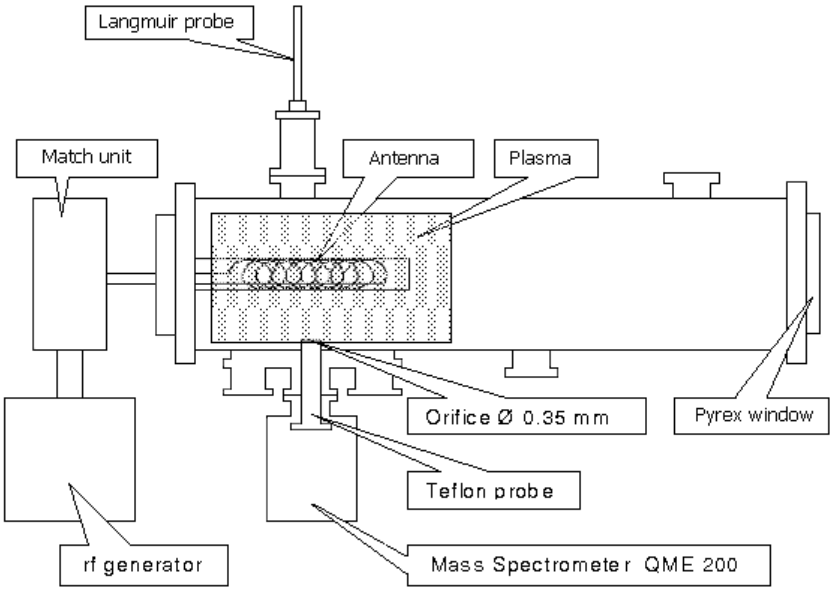

Figure 2.2: *Schematic of the BARIS reactor with the mass spectrometer and Langmuir probe connected.*

2.2 Experimental set-up

2.2.1 The BARIS reactor

The mass spectrometer (described in 2.2.2) is mounted on the BARIS reactor which consists of a helical antenna mounted in the center of a stainless steel cylindrical discharge chamber [30]. This reactor is 900 mm long and has an internal diameter of 200 mm (see figure 2.2). One end of the reactor is closed with a 15 mm thick pyrex window and the other with a stainless steel flange. The flange has a 50 mm port to allow for insertion of a quartz tube in which the helical antenna is positioned. The antenna is isolated from the discharge by a quartz tube and is driven at 13.56 MHz. The impedance of the antenna is matched to that of the rf generator by means of an automatic impedance matching unit.

Rf power coupling

The radio frequency power was supplied by a Marconi ACG-3 rf generator operating at the standard industrial frequency of 13.56 MHz which is capable of delivering 300 W continuous power. The forward and reflected rf power was monitored using two Bird 43 Thruline wattmeters (one for forward and one for reflected power) which were externally adjusted by a PC via an RS232 interface.

The rf power was impedance matched to the plasma load using a standard 'L' configuration RFPP AM20 automatic matching unit (see figure 1.2). The purpose of the matching unit is ensure maximum power transfer by impedance matching the rf source impedance with the plasma discharge impedance to minimise reflected power. Since plasma impedance is a dynamic quantity, a variable matching unit must be used. The standard 'L' configuration matchbox consists of a variable load capacitor in parallel with the discharge, and a variable tune capacitor in series with the discharge.

The rf antenna is arranged in a helical configuration with 11 turns of 3 cm diameter. It is composed of gold plated copper tubing through which water or compressed nitrogen can be pumped for cooling. The antenna was aligned co-axially in the centre of a cylindrical stainless steel discharge chamber and isolated from the discharge by placement inside a quartz dielectric tube. This is known as a re-entrant configuration.

Mass Flow Controllers

Argon and oxygen gas flow was controlled using two STEC SEC-4000 Series Mass Flow Controllers (MFC). The MFC's use a thermal sensor to measure the heat flow of the gas flowing through it and hence the flow rate. The MFC's were calibrated for the particular gas in use and were capable of

delivering 200 sccm for argon and 20 sccm for oxygen. An analogue interface on the MFC allowed control and monitoring of flow rate set points via a PC.

Pressure and Residence time

The base pressure was maintained at 10^{-5} Pa using an Edwards rotary pump and a Pfeiffer Balzers turbomolecular pump. An externally controlled gate valve was also used to regulate pressure and residence time via command sequences sent over an RS232 interface. The controller continuously changes the stepper motor position of the gate valve in order to maintain the target pressure set point or residence time. Pressure was monitored using a Baratron manometer gauge and an Inficon hot ion combi gauge.

2.2.2 Mass spectrometer

A quadrupole mass spectrometer Pfeiffer QME 200 ("Prisma") was used for analysis of the chemical composition of the plasma neutral component within the mass-to-charge ratio (m/z) range of 1 - 199 a.u. The entrance aperture of the mass spectrometer was separated from the discharge chamber by a hollow teflon probe with a 0.35 mm aperture open to the plasma chamber to prevent overloading of the ion source as shown in figure 2.2. Ionisation was achieved by electron impact ionisation with a mean electron energy of ~ 70 eV and electron current of ~ 2.5 mA. A Faraday cup detector senses the ions passing through the analyser. The system is differentially pumped with a Pfeiffer TMH 071P turbomolecular pump equipped with an electronic drive unit TC 600. The base pressure was $\approx 10^{-6}$ Pa.

Teflon probe

The mass spectrometer was designed for partial pressure analysis at pressures below 0.01 Pa although, typically, gas pressures in the discharge were of the order 1.3 - 13.3 Pa. To overcome this pressure differential, a hollow cylindrical teflon probe was used to connect the entrance aperture of the spectrometer with the discharge chamber. The teflon piece was machined in the form of a hollow tube of internal diameter 1.75 cm and length of 10 cm. The plasma facing end of the probe had a diameter of 0.35 mm and length 1 mm thus sustaining the pressure in the spectrometer ionisation chamber at $\sim 10^{-4}$ Pa during the experiments without losses on the walls of the probe. Such a pressure range is required for two reasons, firstly, linearity between the partial pressure of a gas component and intensity of the corresponding m/z signal remains unchanged and secondly, the highest level of experimental signal-to-noise ratio is attained.

2.2.3 Langmuir Probe

A Langmuir probe was employed to monitor ion flux as a function of ICP power. This probe incorporates passive rf compensation so the probe tip can follow the plasma potential oscillations at 13.56 MHz [31]. Removal of rf fluctuations in the plasma potential by rf compensation is required to reduce the plasma-probe sheath impedance. This is achieved by using a compensation electrode that is essentially a large conductor in contact with the plasma and is capacitively coupled to the probe tip [13, 32]. The self resonant inductors are positioned near the tip which serve to increase the probe to ground impedance. This results in a probe-ground impedance that is much greater than the plasma-probe impedance so that the latter

is effectively independent of probe bias. In these experiments, a tungsten probe tip, 5 mm in length with a radius of 0.195 mm is used. The probe is positioned so that it measures in the center of the plasma zone as shown in figure 2.2.

2.3 Real-time control of ion flux and atomic oxygen density in an Ar-O_2 plasma

In this section, real-time control of plasma parameters such as ion flux and atomic oxygen density in an Ar-O_2 plasma is described [33]. Real-time control of such parameters requires diagnostic development and modification of existing techniques [34, 35]. To implement these diagnostics, a control platform was necessary and a control-oriented process model to support control design. In this case, the control-oriented model was created in Matlab Simulink before being compiled and executed in xPC target.

Note: a real-time system is one in which the quality of a result depends on how accurate the calculation is and the time it takes for the result to be available i.e. a real-time task must be able to keep up with the system tasks connected to it [36].

A number of diagnostic techniques were applied to the BARIS reactor to characterise the plasma process. These included a Langmuir probe, a B-dot probe, optical emission spectroscopy (OES), actinometry and mass spectrometry. Following initial control trials, a selection of these diagnostic techniques were individually integrated into the control platform namely, OES; actinometry; mass spectrometry and the Langmuir probe. However, it should be noted that the focus for the work in this thesis is restricted to the mass spectrometer and the Langmuir probe diagnostics.

A control-oriented process model, developed by Keville and Iordanov [34, 35] is used to design a control algorithm. A global model of the chemical kinetics coupled to an analytical model of power deposition is used to simulate the process. The model includes dynamics of actuators such as mass flow controllers and the exhaust throttle as well as sensor characteristics. The application of this control-oriented model to achieve multi-variable closed loop control of selected species such as atomic oxygen and ion density, using rf power; oxygen/argon flow rates and pressure/exhaust flow rate as the actuators, in an Ar-O_2 ICP plasma is described. But first a description of closed loop control will be given.

2.3.1 Closed loop control

Closed loop control or feedback control is designed to attain a desired process condition or set-point, u, by measuring a given process condition, comparing this measured value with a set-point and initiating corrective action based on the difference between the measured and the setpoint value. Open loop (feedforward) control on the other hand, does not use feedback to determine if the setpoint has been reached [37]. An open-loop controller is used for simple processes where feedback is not critical. However, to obtain more accurate control, it is necessary to feed the output of the system back to the inputs of the controller. A simple example of such a system is shown in figure 2.3, this is known as a single-input-single-output (SISO) control system.

Closed-loop transfer function

The output of the system $y(s)$ is fed back through a sensor, $F(s)$, so that the reference signal, $r(s)$, is followed, while rejecting disturbance, d. The

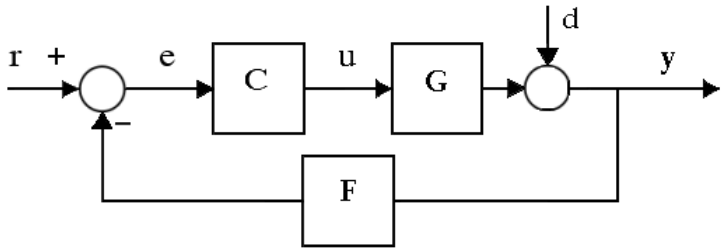

Figure 2.3: *A simple feedback control loop.*

controller, $C(s)$, then takes the error, e, between the reference and the output to change the inputs, u, to the system under control, $G(s)$, giving

$$y = Sr + Td \tag{2.4}$$

where S, the closed loop transfer function is expressed as

$$S(s) = \frac{C(s)G(s)}{1 + F(s)C(s)G(s)}. \tag{2.5}$$

Here, the numerator is the forward (open-loop) gain from r to y, and the denominator is one plus the gain in going around the feedback loop, i.e. the loop gain. T, the transfer function between the disturbance, d and the output, y, given by

$$T = \frac{1}{1 + C(s)G(s)}. \tag{2.6}$$

In an ideal case where $S = 1$ and $T = 0$, simply setting the reference point controls the output.

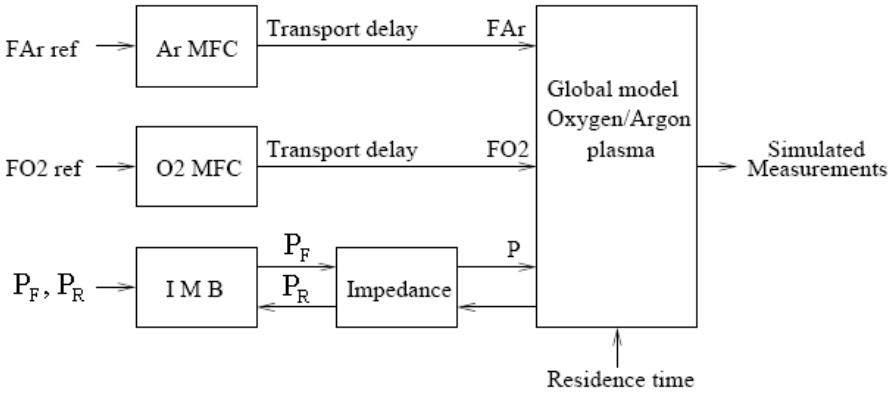

Figure 2.4: *A block diagram of the process.*

2.3.2 Process model for control of atomic oxygen density

The sensors that are presented here are the Langmuir probe and mass spectrometer. Each of these has an independent PID [1] control loop (described in section 2.3.3) with very different time scales. Loop 1, which controls the ion flux (as measured by the Langmuir probe) with rf power, is almost instantaneous while, loop 2, controlling the atomic oxygen density (measured by the mass spectrometer) with O_2 flow rate is of the order of tens of milliseconds.

A complete control model is required for closed loop control of a particular species in the plasma which in this case is atomic oxygen density. In figure 2.4 a block diagram of the process is shown. The control oriented model used is a very simplified global model of oxygen kinetics, outlining the primary production and loss mechanisms for atomic oxygen in the plasma.

Atomic oxygen production is given by:

$$e + \mathrm{O}_2 \longrightarrow \mathrm{O} + \mathrm{O} + e \ , \tag{2.7}$$

[1] Proportional Integral Derivative

and the loss mechanism is:

$$\mathrm{O} \longrightarrow \frac{1}{2}\,\mathrm{O_2}\ . \tag{2.8}$$

The global model was coupled to transfer function models of the mass flow controller and gas flow into and out of the chamber as follows:

$$\frac{d[\mathrm{O_2}]}{dt} = F_{\mathrm{O_2}} - \frac{[\mathrm{O_2}]}{\tau_{diss}} + \frac{[\mathrm{O}]}{2\tau_{rec}} - \frac{[\mathrm{O_2}]}{\tau_{res}} \tag{2.9}$$

$$\frac{d[\mathrm{O}]}{dt} = \frac{2[\mathrm{O_2}]}{\tau_{diss}} - \frac{[\mathrm{O}]}{\tau_{rec}} - \frac{[\mathrm{O}]}{\tau_{res}} \tag{2.10}$$

where $F_{\mathrm{O_2}}$ is the flow rate per unit volume of oxygen, τ_{diss} is the dissociation time constant, τ_{rec} is the diffusion dependent recombination time constant and τ_{res} is the residence time.

Transfer function for atomic oxygen - Laplace transform

A transfer function is a mathematical statement of the influence which a system or individual component has on a signal compared at input and at output terminals i.e. the ratio of the output of a system to the input. Operation of a Laplace transform reveals the open loop transfer function for atomic O:

$$\frac{[\mathrm{O}](s)}{F*(s)} = \underbrace{\left(\frac{2}{1+\tau_{diss}/\tau_{rec}}\right)}_{\text{Diss/rec(static gain term)}} \underbrace{\frac{e^{-sT_d}}{(s\tau_{mfc}+1)(s\tau_{res}+1)}}_{\text{Dynamics of gas flow}} \tag{2.11}$$

Note: Assume τ_{diss}, $\tau_{rec} \ll \tau_{mfc}$, τ_{res}. The dynamics of atomic oxygen production can be decoupled into dissociation and recombination in the plasma and the dynamics of gas flow into the chamber.

The MFC was modeled as:

$$\frac{F(s)}{F*(s)} = \frac{K_{mfc}e^{-s\tau_{delay}}}{s\tau_{mfc}+1} \tag{2.12}$$

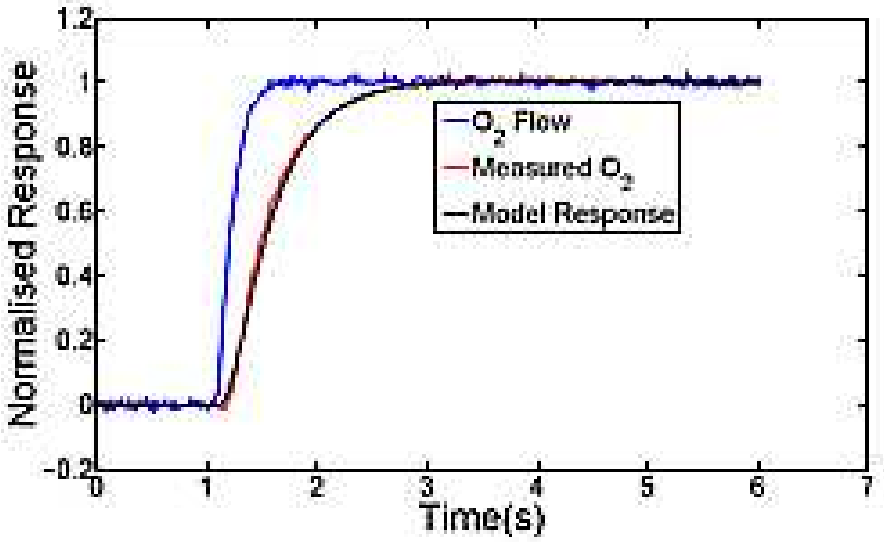

Figure 2.5: *Comparison of chamber residence time model and measured response to a step in O_2 flow rate .*

where the gain of the MFC, $K_{mfc} = 1$, the MFC time constant, $\tau_{mfc} = 120$ ms and a time delay, $\tau_{delay} = 80$ ms.

The chamber residence time was modeled using MATLAB system identification[2] toolbox:

$$\frac{[O_2](s)}{F_{O_2}(s)} = \frac{1}{s + 1/\tau_{res}} \Rightarrow \tau_{res} = 350 \text{ ms} \tag{2.13}$$

In figure 2.5, the measured O_2 response to a step in O_2 flow rate, F_{O_2}, is plotted as a function of time and the corresponding model response is also shown. The model is a good mathematical representation as the measurement and the model outputs overlap, indicating excellent agreement.

Figure 2.6 shows the response of the mass flow controller model and the measured signal to step in O_2 flow rate over time. In this case, the lag is

[2]system identification algorithms determine the model structure and estimate model parameters [38]

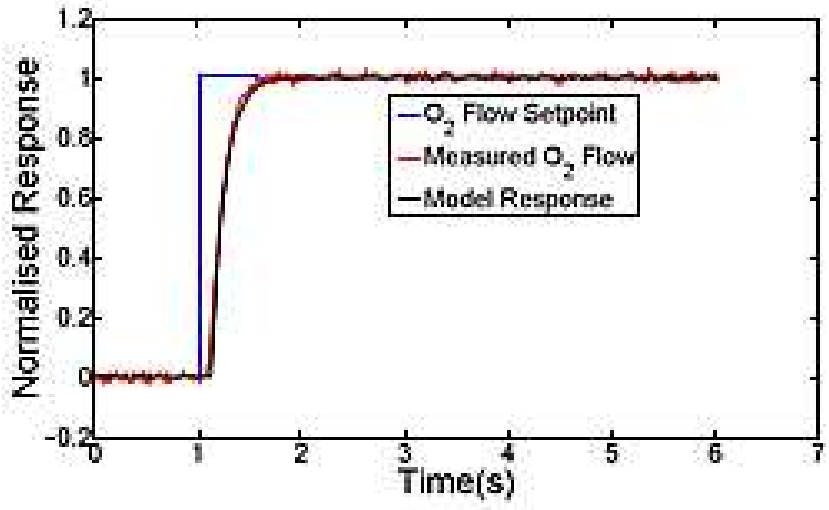

Figure 2.6: *Comparison of Mass flow controller model and measured response to a step in O_2 flow rate.*

shorter but again both the measured and model signals respond in a similar fashion. Thus it has been shown that the characterisation of chamber residence time and the mass flow controller with MATLAB system identification toolbox gave excellent agreement between measurement and model.

The control algorithm for atomic oxygen was implemented using a SISO PID controller with xPC Target (described in the next section) using the O_2 MFC as the actuator and the inferred measurement of relative atomic oxygen density from the O_2 signal of the mass spectrometer as the sensor.

2.3.3 Real-time control via xPC target

Real-time control on the BARIS system was implemented using a specialised real-time platform known as xPC Target (MathWorks Inc.) [35]. xPC Target is a MATLAB toolbox for implementing any control structure modeled in MATLAB Simulink toolbox using standard hardware [39]. It operates with

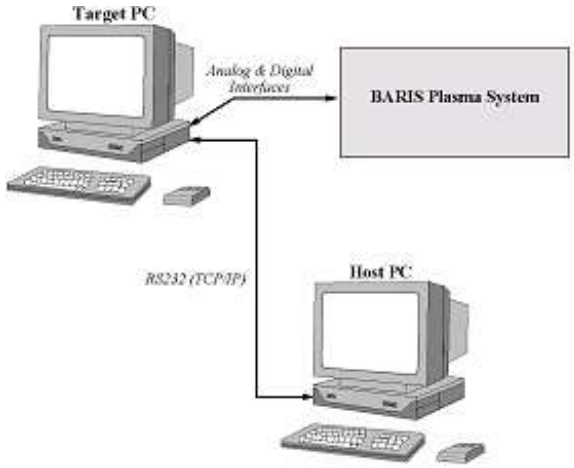

Figure 2.7: *Real-time control configuration with xPC target.*

a two-PC configuration using a 'target' PC and a separate 'host' PC. A simple block diagram that illustrates the xPC Target hardware set-up for the BARIS process is shown in figure 2.7.

The host PC was used for building the executable code, while the target PC runs the deployed module. All input/output (I/O) hardware that operates actuators and sensors is installed on the target PC. Configuration and execution of the control model was performed in the host PC. This has a graphical user interface (GUI) that enables the user change set points, control parameters and system parameters. Communication between both PCs was established with an RS232 interface. Here, a PC with MATLAB and Simulink installed on it was used as the host PC.

A Simulink model of the process was created by Iordanov and Keville [34, 35], and simulations were initially tested in MATLAB in non-real time via xPC Target to ensure the control algorithm worked. xPC Target allows the addition of numerous I/O device blocks to the model, which enables the creation of an executable code by using "Real-Time Workshop", which is

another MATLAB toolbox and a C/C^{++} compiler. The executable code was downloaded from the host PC to the target PC. Measured and manipulated variables can be monitored and recorded on both host and target PCs.

PID controller

The control design used by Simulink is a PID controller. The term PID (Proportional-Integral-Derivative) refers to the three terms operating on the error signal to produce a control signal. If u(t) is the control signal sent to the system, r(t) is the desired output and y(t) is the measured output, with tracking error e(t) = r(t) - y(t), the PID controller can be expressed in the form

$$u(t) = \underbrace{K_P e(t)}_{P} + \underbrace{K_I \int e(t)dt}_{I} + \underbrace{K_D \frac{d}{dt} e(t)}_{D} \tag{2.14}$$

The desired setpoint is obtained by adjusting the three parameters: K_P, K_I and K_D of the controller, using estimates from a separate model. Stability can be ensured using only the proportional term. The integral term permits the rejection of a step disturbance and the derivative term can be used to provide damping or shaping of the response. Figure 2.8 shows the structure of a typical PID controller.

Closed loop response

The closed loop response of the inferred relative atomic oxygen density for three different power levels is depicted in figure 2.9. This figure shows how the PID controller behaviour varies with changes in the process conditions. Decreasing applied power results in reduction of τ_{diss} and thus static gain increases as inferred from equation 2.11.

The atomic oxygen density measurement used in this control regime was

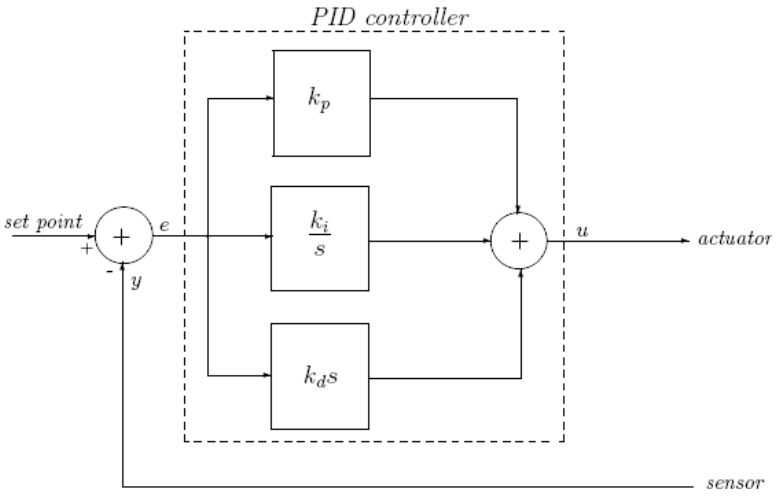

Figure 2.8: *Structure of a closed loop PID controller.*

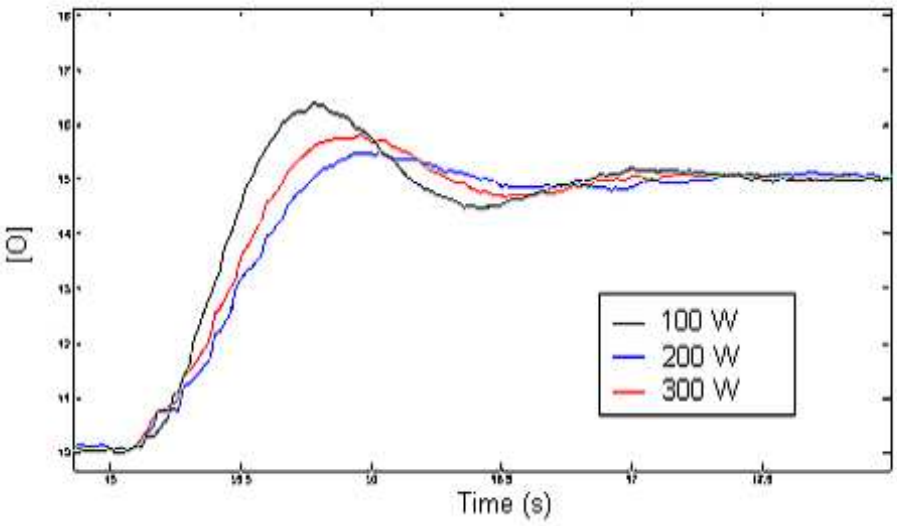

Figure 2.9: *Closed loop response of atomic oxygen density at various rf power levels.*

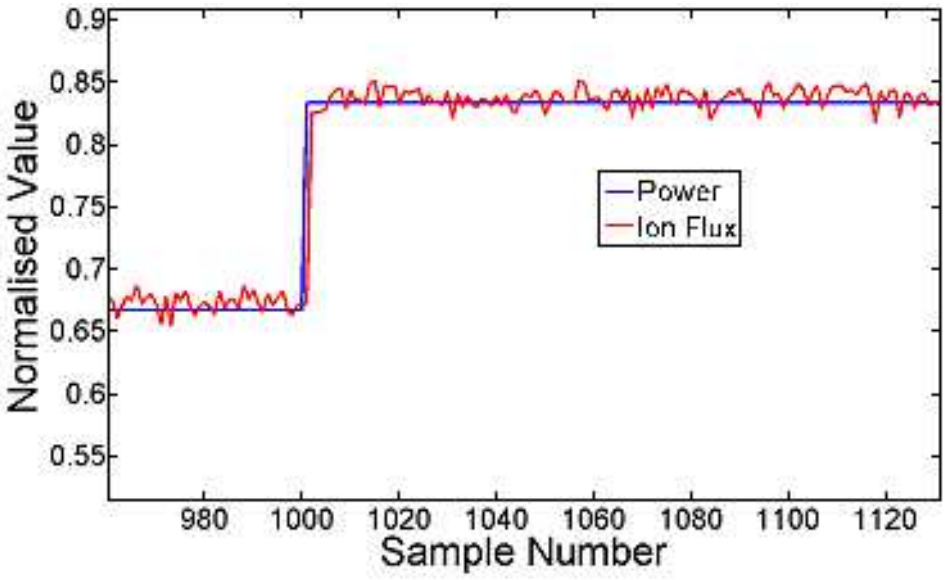

Figure 2.10: *Open loop ion flux response to a step in power in an Ar plasma.*

that inferred from the molecular oxygen signal obtained by mass spectrometry (described in the Appendix A).

A SISO PID controller was first operated on this platform to achieve control of ion flux using rf power as the actuator and the collected ion current to a Langmuir probe biased at -50 V as the sensor. The response of ion flux to changes in rf power was almost instantaneous and thus operates on a much faster time scale than the response time of atomic oxygen density to changes in O_2 flow rate ($\sim$ ms).

The open loop response of ion flux to a step in rf power in an Argon plasma is given in figure 2.10. In this case, the sample time was set to 100 ms but it was later reduced to 20 ms. Figure 2.10 shows that the response to changes in rf power are almost instantaneous.

The closed loop response of ion flux to a step in rf power in an Argon plasma is shown in figure 2.11. Again, the measurement follows the setpoint very closely.

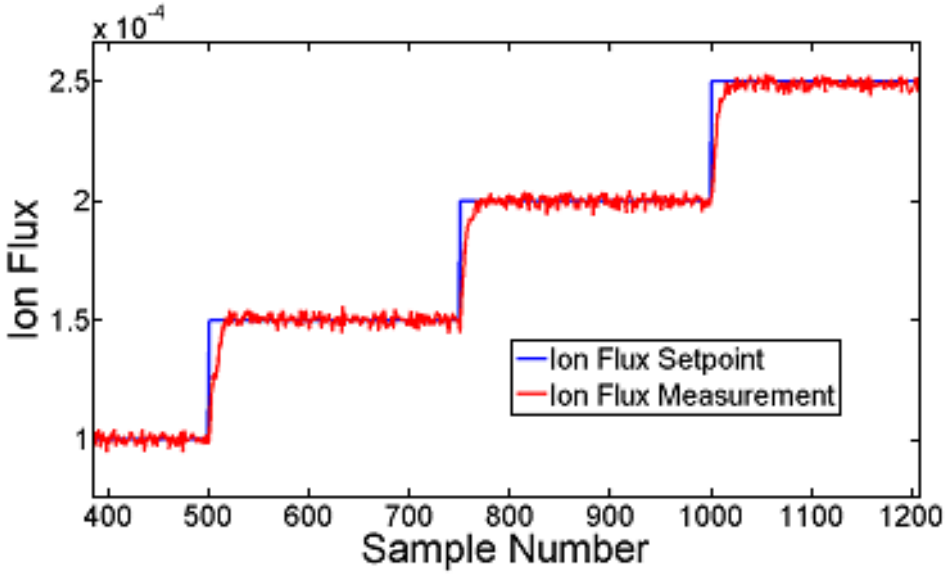

Figure 2.11: *Closed loop ion flux response to a step in ion flux setpoint in an Ar plasma where rf power is the actuator and ion flux is the output.*

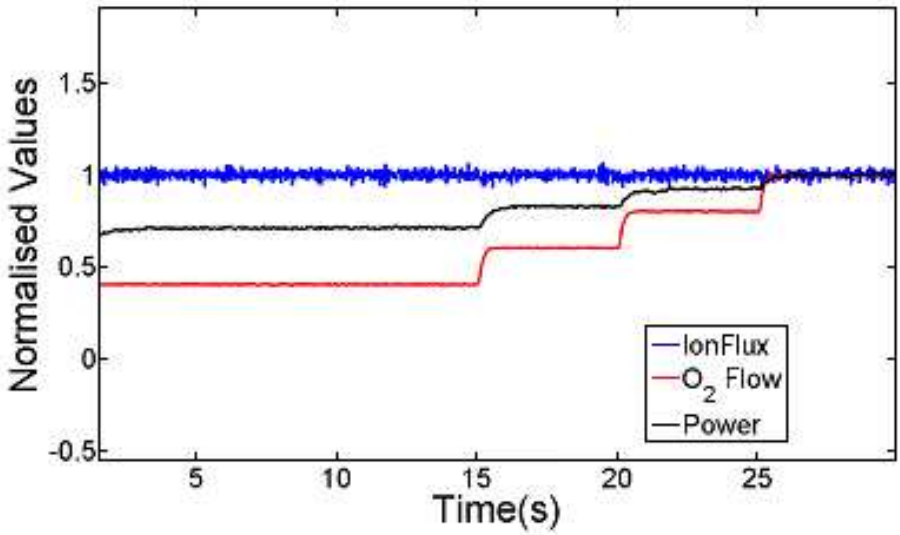

Figure 2.12: *Ion flux response to a step in O_2 flow rate.*

Finally the control of the ion flux set point to a step in O_2 flow rate into the chamber is shown in figure 2.12. This is an example of disturbance rejection. By applying a disturbance to one of the manipulated variables (which is flow rate in this case), the rf power changes to compensate for this disturbance.

2.4 Summary

In this chapter closed loop control of ion flux and atomic oxygen density with a Langmuir probe and mass spectromter was described. Control was achieved by using two separate single input/single output (SISO) PID loops which were optimised experimentally. The control algorithm used for atomic oxygen density control combined the models for gas flow dynamics in the chamber (i.e. residence time and mass flow controller response time) through system identification with a simplified global model of atomic oxygen production. The global model used the chemical kinetic processes of dissociation of molecular oxygen and the recombination of atomic oxygen to describe the dynamics of atomic oxygen production in the chamber.

Given the response times of the SISO loops, it was found that the ion flux as measured by the Langmuir probe responded to changes in rf power almost instantaneously while response time of atomic oxygen density measured by the mass spectrometer to changes in O_2 flow rate was of the order of milliseconds. These changes can modify the plasma parameters considerably. Ultimately, the ability to monitor and tune the ion energy impacting a surface and the electron temperature would be more desirable as it is these parameters that determine the etch rates. In chapter 5, ion energy distributions measured at a remote surface will be discussed.

2.4 Summary

The signal from the mass-spectrometer takes some time to stabilise (~ 30 minutes) so the mass-spectrometer electron emission had to be switched on well in advance of taking measurements. In addition to this, the temperature of the discharge chamber increases over time and consequently drift in the measured ion current from the mass spectrometer was evident during testing. To test the effect of process drift and accelerate stabilisation, the discharge chamber was heated to approximately 100°C by applying a heating coil but this had no significant effect on the results.

CHAPTER 3

Experimental Reactor

3.1 The ARIS reactor

The experimental reactor used in the remainder of this thesis (Applied Radio-frequency Inductive Source or ARIS) is an expanding inductive source configuration which was originally designed for the study of low temperature plasma chemistry [40]. It has also been used in other studies, such as the investigation of collisionless heating [9], and of uncompensated probes [16]. The reactor consists of a source region and an expansion chamber. Ignition of the plasma is by way of rf inductive coupling in the source region. Plasma expands from the open end of the source region into a larger cylindrical chamber. This expansion chamber features numerous ports for applying diagnostics.

An axial dc magnetic field can also be used to excite helicon discharges

in the source region but will not be discussed here. For the most part, the experiments were conducted with the discharge in inductive power coupling mode and a small number in capacitive mode. The majority of the experimental results presented in this thesis were carried out in the expansion region of this chamber.

3.1.1 Chamber geometry

The reactor consists of two discrete regions as shown in figure 3.1 [9]. The source consists of a quartz tube that has 100 mm external diameter, 10 mm wall thickness and a length of 150 mm. It is closed at one end with a stainless steel cap and the other end is connected to the expansion chamber. The larger cylindrical expansion region is made of stainless steel with a 410 mm internal diameter and length of 290 mm which is terminated at both ends with stainless steel plates. One of these plates is connected to the source at one end by an opening of equal diameter to the quartz tube.

A three turn copper antenna surrounding the quartz tube provides rf coupling to the source. Aluminium electrostatic shielding encloses the tube and antenna to prevent the emission of rf radiation. This shielding is mounted to the open end of the stainless expansion chamber securing the source in a fixed position. All metal surfaces of the chamber are grounded.

3.1.2 RF power coupling

Power is inductively coupled through the antenna which is driven at 13.56 MHz with an RFPP (Radio-Frequency Power Products) 3 kW generator. The antenna is impedance matched to the generator output impedance (50 Ω), using a matching network to ensure maximum power transfer.

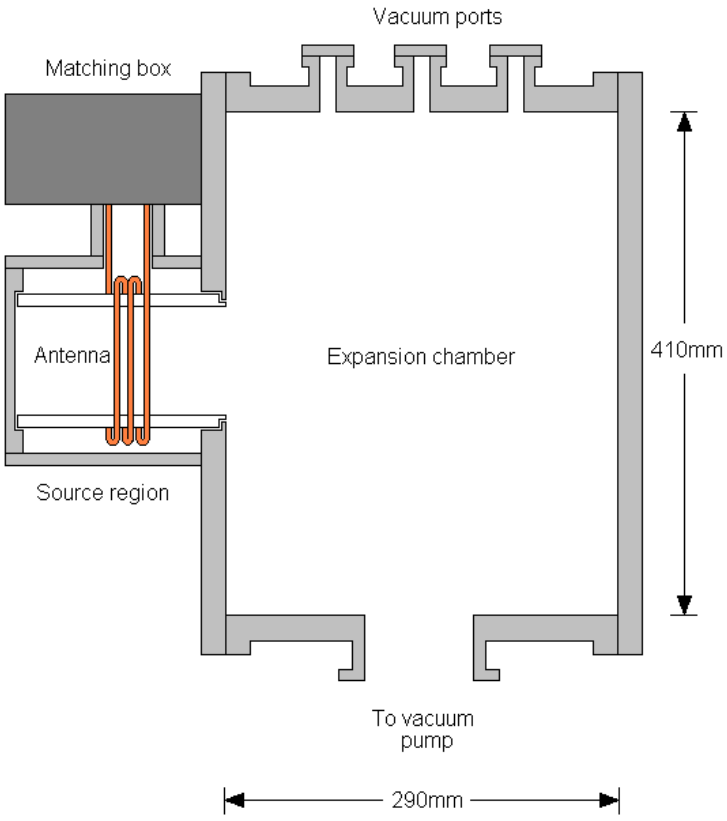

Figure 3.1: *Schematic of the ARIS device showing source and expansion regions.*

The match box is positioned in a manner that allows direct connection of the antenna to the output capacitor of the matching network minimizing ohmic power loss at the antenna side of the matching network. The match box is used in automatic matching mode so that the power delivered to the discharge is held constant.

A small amount of rf power is absorbed in the antenna, as a result the source is heated and air cooling is required. At high frequencies the resistance of the antenna increases due to the skin effect and is accompanied with power dissipation. Ion bombardment of the source walls also leads to heating of the source region.

The plasma is formed in capacitive mode by the large rf voltage on the antenna. When the plasma density increases adequately the discharge proceeds to an inductive mode and is maintained by the time varying magnetic field associated with the rf currents through the antenna.

Predominantly, experiments were performed in the range of 200 - 500 W where the rf power coupling was stable with little or no reflected power, although some were performed at higher powers of up to 700 W.

3.1.3 Vacuum system

A number of gases were used in the experiments such as argon, oxygen, helium and nitrogen although mostly the experiments were conducted in argon. Gas is fed to the expansion chamber using a mass flow controller rated at 100 sccm. Pressure was maintained by a Pfeiffer Vacuum turbomolecular pump (TPH 521 PC, ultimate vacuum $< 1 \times 10^{-6}$ Pa) backed with an Edwards rotary pump (E2M28 ultimate vacuum ~ 0.1 Pa) and monitored using a Leybold Vakuum Ionivac combi hot ion-Pirani gauge (ITR 90, pressure range: 5×10^{-8} - 1×10^{5} Pa). The base pressure of the system

is ≈1 x 10^{-4} Pa, but the experimental operating pressure was held around 0.1 Pa. This was the pressure range for which the plasma and matching unit was most stable, thus allowing repeatability. Under these conditions, the plasma density and electron temperature in this chamber are known to be about 4 x 10^{15} m^{-3} and 4 eV respectively [9, 16, 40]. Thus, the mean free path for electron-neutral momentum transfer is about 20 cm. This is much larger than the sheath width or probe radius, so the probe is essentially operated in the collisionless regime. Generally, the gas flow is held constant and the pressure is adjusted using a large gate valve mounted between the turbo pump and the chamber.

3.2 Radio-frequency biased electrode

An electrode is mounted on the end plate of the inductively coupled plasma reactor. This electrode is excited with an rf voltage which is capacitively coupled from a separate generator (and at a different frequency) to that powering the inductive source [9]. No matching network is used to enhance power coupling through this electrode. Instead, an inductive coil is placed in series with the blocking capacitor to step up the voltage at the electrode surface. This method allows relatively large exciting voltages on the electrode for relatively low output power levels of the rf generator. Additionally, as there is only small amounts of power coupled through the remote electrode, the plasma created by the inductive source remains unperturbed. A dc supply is incorporated to allow control of the electron current reaching the electrode surface.

The electrode is a 60 mm copper disc mounted in a PTFE (teflon) holder which prevents plasma formation behind the electrode. A schematic detailing

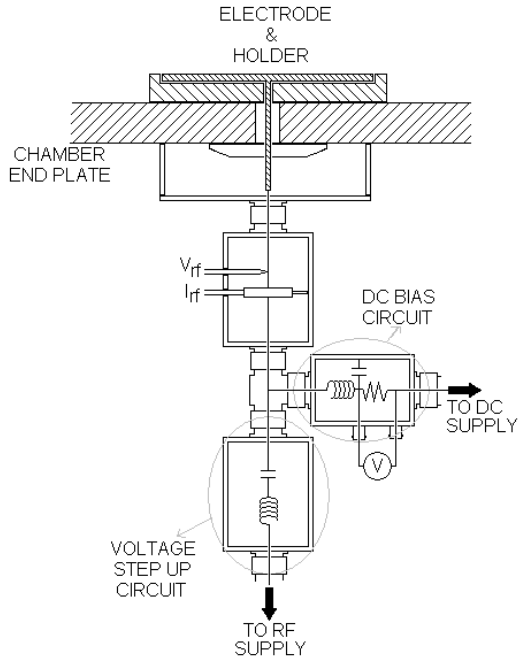

Figure 3.2: *Schematic of the biased electrode system, showing both the rf power coupling circuit and the additional dc biasing circuit.*

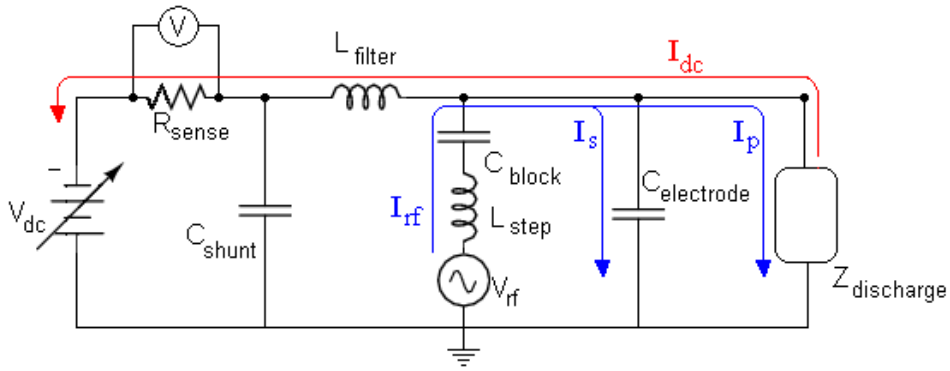

Figure 3.3: *Equivalent circuit model of the electrode system and bias circuitry.* C_{block} *and* C_{shunt} *are blocking and shunt capacitors respectively.* $C_{electrode}$ *is the electrode capacitance to ground and* L_{filter} *blocks rf current reaching the dc supply.* I_s *and* I_p *are the stray and plasma rf current respectively and* I_{dc} *is the dc current drawn by the dc supply.*

the mounting of the electrode and the biasing circuitry is given in figure 3.2. An equivalent circuit model of the system showing both the rf and dc current paths is given in figure 3.3.

3.3 Summary

The experimental reactor and related instrumentation have been detailed. The geometry and operation of the reactor used to generate the discharges has been outlined. The reactor itself is an inductively coupled system made of a source region and a diffusion region. The plasma is ignited in a high density source region and subsequently expands into a much larger cylindrical chamber where various diagnostics are mounted. These diagnostics will be described in turn in the following chapters. The gases used in the experiments are argon, oxygen and helium of various mixtures, at pressures of about 0.1 - 1.2 Pa. The rf power range used was 200 - 700 W at a frequency of 13.56 MHz.

3.3 Summary

The inductive reactor is used to maintain the plasma only, while all Retarding Field Eenergy Analyser (RFEA) results were taken using an independently rf driven electrode mounted far from the inductive source (a thorough investigation of the RFEA sensor is detailed in chapter 5). The remote electrode is driven at a separate frequency from the inductive source so as to avoid interference effects such as beating. Also, the circuitry needed to apply both rf signals and dc bias levels to the electrode have been explained. This circuitry is important so that the rf supply does not affect the dc supply and vice versa.

CHAPTER 4

Ion mass probe

In this chapter, a novel sensor was investigated to establish if the ion mass could be detected by measuring differences in ion current in static fields. Mass detection in discharge chambers is not a trivial matter. Standard equipment used for this purpose such as mass-spectrometers are costly, bulky and difficult to apply in most situations. As a result, numerous efforts have been made in recent years to to develop portable and miniaturised mass-spectrometers [41–47].

Taylor *et al* [44] developed a miniature quadrupole mass spectrometer (QMS) by application of microelectromechanical systems (MEMS) technology. The resultant mass filter which is just 30 mm long, consists of metal coated optical fibers that serve as the cylindrical rods used in a typical QMS. These metalised fibres are mounted on silicon substrates and arranged in line with a commercial ion source at one end connected to a vacuum flange

and a Faraday collector at the other. The MicroQuad mass filter allowed operation at pressures up to 2.5 Pa albeit with limited resolution. Another miniaturisation development was realised with the introduction of a micro-fabricated einzel lens by Syms *et al* [46]. This two-dimensional electrostatic einzel lens provides a line focus ion coupling for the aforementioned mass filter developed by Taylor *et al*. The overall length of the lens, quadrupole and collector assembly is just 40 mm. Given the reduced size of the optics and filter systems, lower drive voltages can be used at higher pressures. However, these scaled down instruments still require additional vacuum systems and so true portability has not been achieved. In the following sections a novel probe known as the ion mass probe (IMP), engineered to measure ion mass without additional pumping systems is presented. This probe was conceived when results of a mach probe used by Doggett *et al* and Sheerin [48, 49] showed some mass dependence in a laser plasma.

Tests have been carried out with the Ion Mass Probe (IMP) on the ARIS reactor in pure Ar plasmas and Ar-O_2 mixtures under various plasma conditions. The fundamental concept is that the rate of change of collected ion current with bias voltage, is expected to vary with ion mass.

Ion optics simulation software, SIMION, has been used to simulate electric fields, ion trajectories and to calculate the time-of-flight (TOF) for various energies within those fields.

4.1 Mechanical design

The ion mass probe (IMP) consists of a cylindrical Langmuir probe oriented perpendicular to a planar probe as shown below in figure 4.1 (a). The planar probe is a 5.6 mm diameter copper disc which is mounted on a machined

teflon holder. An electrical connection is fed along the outer edge of the teflon holder to a semi-rigid coax cable as shown in figure 4.1 (b). The teflon piece is also center bored to support the cylindrical probe. A 1 mm hole in the center of the planar probe allows insertion of the cylindrical probe through non conducting material. The cylindrical probe is made of tungsten, with a length of 2 mm and a radius of 0.2 mm. It is situated 2 mm behind a grounded mesh of 0.5 mm perforations, this acts as the interface between the probe sampling region and the plasma. As the diameter of the probe is relatively small ($\sim$ 12 mm outer diameter), it can be inserted directly into a plasma processing chamber without the need for a separate vacuum system.

The probe bias is supplied by an Impedans electronics unit (IV Scanner) [50] via BNC connections and coaxial cables. The IV Scanner has three output channels with a range of -150 V - +150 V. One of these channels is set to a constant output level to bias an electrode and a second channel is used to sweep the bias on the other electrode. For each step in the voltage scan series, the collector current is determined to construct the current-voltage characteristic. Data is transferred to a PC through a universal serial bus (USB) connection.

4.2 Theory of operation

The principle aim is that application of a bias to the probes will generate an ion flow in the sampling region. The flow velocity can then be adjusted by changing the bias on either electrode. The ion trajectory in the sampling region will be dependent on the ion mass, velocity and energy as shown by the trajectories in figure 4.2. Varying the relative bias between the planar electrode and the cylindrical electrode can alter the flight path resulting in

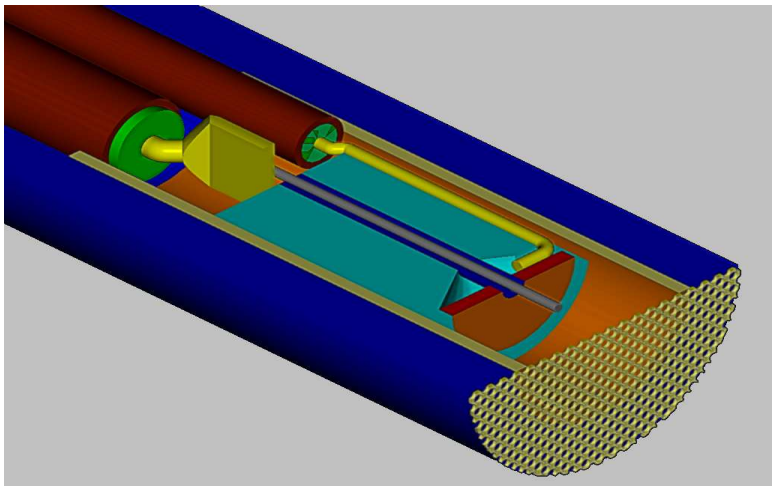

(a) Cross-section

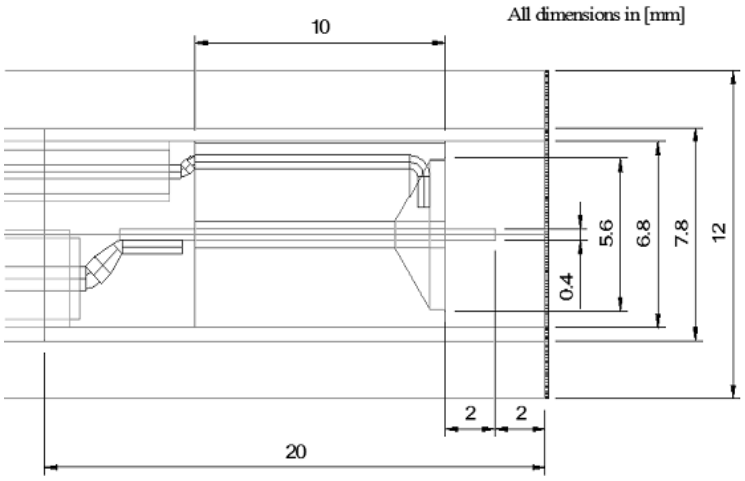

(b) Dimensions

Figure 4.1: *(a) Cross-section and (b) dimensions of the ion mass probe (IMP).*

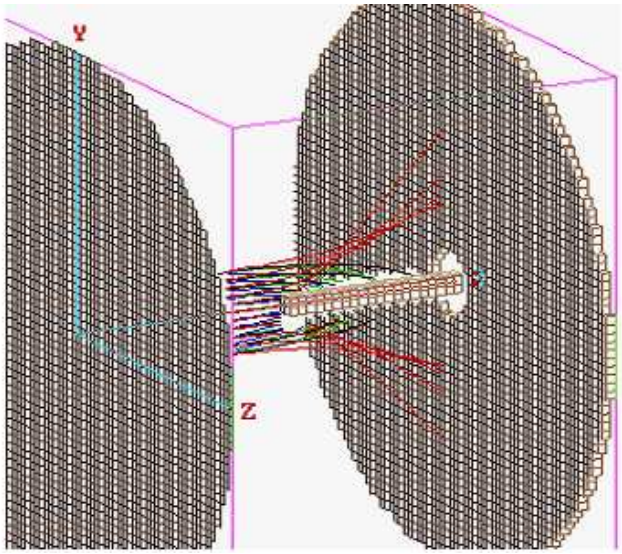

Figure 4.2: *Schematic of particle trajectories in the sampling region of the IMP. Blue = 10eV ions, green = 50 eV ions, black = 100 eV and red = 100 eV electrons [cylindrical probe bias = -10 V, planar probe bias = 0 V].*

a change in the collected ion currents at each probe. The ratio of planar to cylindrical current is assumed to be mass dependent.

While one probe is swept through a range of voltages with the IV Scanner, the other is biased externally in increments for each IV Scanner sweep. Biasing the planar electrode more negative than the cylindrical reduces the ion current measured at the cylindrical electrode, as expected. Initial tests with the Impedans system showed that increasing bias on the measuring probe gave an increase in collected current (in the micro-Amp range). The IMP shows that the rate of change (slope) of each IV trace from the cylindrical electrode varies with planar electrode bias which is indicative of a dependence of the slope on the energy of the ions entering the sampling region. This slope should also change with relative ion mass and experiments with Ar-O_2 mixtures appeared to confirm this.

4.3 Experimental

In this section, initial tests of the probe behaviour in an Ar-O_2 plasma is described. The probes are tested in turn i.e. the current is collected at the cylindrical probe for a range of voltages while the bias on the planar probe is held constant. This measurement is repeated for different bias levels on the planar probe. The current to the planar probe is then measured while the bias on the cylindrical probe is fixed at intervals.

4.3.1 Measured probe currents

In table 4.1, the bias on the planar probe is fixed at intervals of -1 V to -120 V in steps of -20 V while the current to the cylindrical probe is measured over the same range.

Table 4.1: *Ion current on cylindrical probe, planar bias fixed at intervals*

$V_{C(V)}$	$I_{P(-1V)}$	$I_{P(-20V)}$	$I_{P(-40V)}$	$I_{P(-60V)}$	$I_{P(-80V)}$	$I_{P(-100V)}$	$I_{P(-120V)}$
-1	-6.51E-07	-1.36E-07	-4.50E-08	-4.63E-08	-3.34E-08	-1.15E-08	1.07E-08
-20	-1.69E-06	-1.03E-06	-5.81E-07	-2.92E-07	-1.90E-07	-1.29E-07	-9.81E-08
-40	-2.67E-06	-1.91E-06	-1.38E-06	-9.69E-07	-5.80E-07	-3.23E-07	-2.29E-07
-60	-3.59E-06	-2.76E-06	-2.15E-06	-1.70E-06	-1.24E-06	-8.51E-07	-5.34E-07
-80	-4.45E-06	-3.59E-06	-2.89E-06	-2.39E-06	-1.86E-06	-1.41E-06	-1.03E-06
-100	-5.28E-06	-4.36E-06	-3.62E-06	-3.06E-06	-2.48E-06	-1.95E-06	-1.55E-06
-120	-6.08E-06	-5.09E-06	-4.31E-06	-3.71E-06	-3.07E-06	-2.48E-06	-2.06E-06

The IV trace is shown in figure 4.3 (a). As the constant bias on the planar probe is increased, the current to the cylindrical probe is reduced. This is to be expected since the planar probe area, A_{Planar}, is much greater than that of the cylindrical probe, $A_{cylindrical}$.

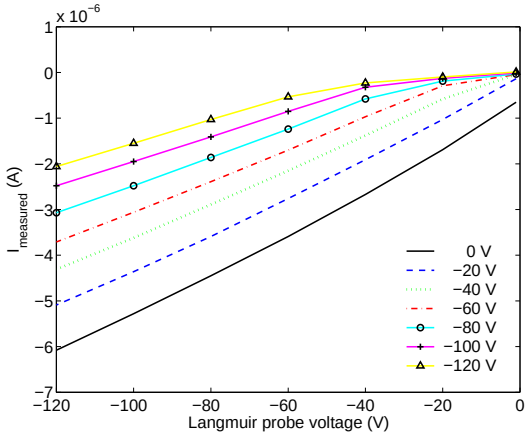

(a) Cylindrical measured, planar bias fixed

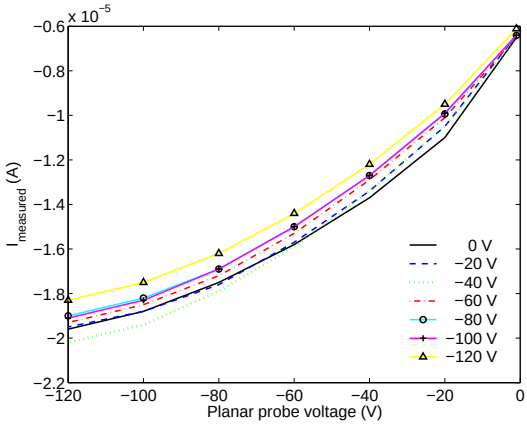

(b) Planar measured, cylindrical bias fixed

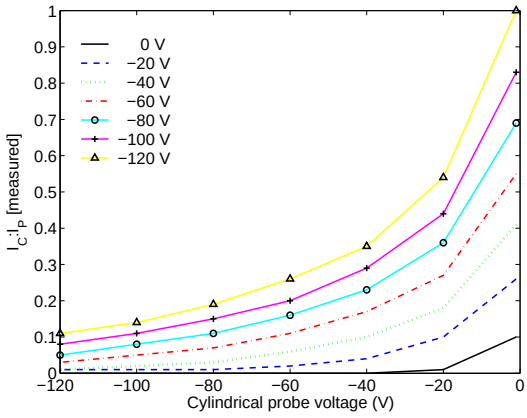

(c) Cylindrical to planar current ratio $I_C : I_P$

Figure 4.3: *Ion current on (a) cylindrical probe with planar bias fixed at intervals, (b) planar probe with cylindrical bias fixed at intervals, (c) Ratio of cylindrical current to Planar current at 0.24 Pa, 300 W ICP power.*

Table 4.2 gives the current measured on the planar probe from -1 V to -120 V with the bias on the cylindrical probe fixed at intervals. The corresponding IV trace is shown in figure 4.3 (b). In this case, increasing the fixed bias on the cylindrical probe had little or no affect on the current measured at the planar probe due the small surface area of the cylindrical which is much less than A_{Planar}.

Table 4.2: *Ion current on planar probe, cylindrical bias fixed at intervals*

$V_{P(V)}$	$I_{C(-1V)}$	$I_{C(-20V)}$	$I_{C(-40V)}$	$I_{C(-60V)}$	$I_{C(-80V)}$	$I_{C(-100V)}$	$I_{C(-120V)}$
-1	-6.51E-06	-6.40E-06	-6.57E-06	-6.47E-06	-6.41E-06	-6.40E-06	-6.11E-06
-20	-1.10E-05	-1.05E-05	-1.05E-05	-1.01E-05	-9.94E-06	-9.90E-06	-9.50E-06
-40	-1.37E-05	-1.34E-05	-1.34E-05	-1.29E-05	-1.27E-05	-1.27E-05	-1.22E-05
-60	-1.58E-05	-1.57E-05	-1.59E-05	-1.53E-05	-1.50E-05	-1.50E-05	-1.44E-05
-80	-1.75E-05	-1.76E-05	-1.79E-05	-1.72E-05	-1.69E-05	-1.69E-05	-1.62E-05
-100	-1.88E-05	-1.88E-05	-1.94E-05	-1.85E-05	-1.82E-05	-1.83E-05	-1.75E-05
-120	-1.96E-05	-1.95E-05	-2.02E-05	-1.93E-05	-1.90E-05	-1.91E-05	-1.83E-05

The ratio of measured cylindrical current to the that of the planar is given in table 4.3 for the range -1 V to 120 V and the corresponding plot is given in figure 4.3 (c).

Table 4.3: *Ratio I_C/I_P where I_C is the current measured on the cylindrical probe and I_P is the current on the planar probe.*

V_{bias}	I_C/I_P	I_C/I_P	I_C/I_P	I_C/I_P	I_C/I_P	I_C/I_P	I_C/I_P
V_P	$V_{C(0)}$	$V_{C(-20)}$	$V_{C(-40)}$	$V_{C(-60)}$	$V_{C(-80)}$	$V_{C(-100)}$	$V_{C(-120)}$
-1	0.10	0.26	0.41	0.55	0.69	0.83	1.00
-20	0.01	0.10	0.18	0.27	0.36	0.44	0.54
-40	0.00	0.04	0.10	0.17	0.23	0.29	0.35
-60	0.00	0.02	0.06	0.11	0.16	0.20	0.26
-80	0.00	0.01	0.03	0.07	0.11	0.15	0.19
-100	0.00	0.01	0.02	0.05	0.08	0.11	0.14
-120	0.00	0.01	0.01	0.03	0.05	0.08	0.11

4.4 *SIMION* Ion trajectory Simulations

In this section an ion optics software package is described and results of simulations given. These can be compared with the measured values obtained in the previous section.

SIMION is a software package for performing charged particle ion optics simulations. It is primarily used to solve 2D/3D electrostatic and magnetic fields and calculate the resultant trajectories of charged particles within those fields. It was originally developed in FORTRAN by D. McGilvery at La Trobe University, Australia to simulate ion motion in an electrostatic lens [51]. The current version (Version 8.0) was developed by Scientific Instrument Services (SIS) Inc. [52].

SIMION has been used to simulate a number of different devices such as quadrupole mass filters, time-of-flight mass spectrometers, ion cyclotron resonance mass spectrometers and quadrupole ion traps [53]. Geometry of electrodes can be configured by the user as well as particle initial conditions, including low frequency time-dependent or rf (MHz range) support, magnetic field, and collisional effects. Customised electrode geometries can be controlled by user programs that govern potentials applied to the electrodes. Geometries can be defined via multiple methods: a 3D paint-like program (Modify), CAD import from stereolithography (.stl) format, solid geometry defined mathematically via a text file (GEM file) and others. An external application called Virtual Device provides a GUI for creating GEM files. A workbench scheme allows the user position, size, and orient instances (3D images) of potential arrays of different grid densities and symmetries in the same simulation.

Particle mass and charges can be defined individually or according to some pattern or distribution in a ".FLY" subroutine. Contour and potential energy

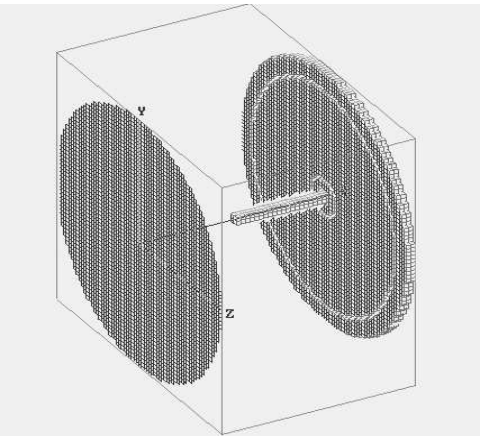

Figure 4.4: *Cross-section of the Ion Mass Probe in SIMION.*

surface plots (optionally with ion trajectories superimposed) are displayed iteratively.

The program uses direct techniques such as finite-difference methods (over-relaxation and multi-mesh methods) and Runge-Kutta for solving the required partial differential equations (PDEs), particularly the Laplace equation and ordinary differential equations (ODEs).

4.4.1 SIMION results

A potential array was created in SIMION which consisted of five electrodes namely: a Langmuir electrode, an electrode separating the probes, a planar electrode, an outer electrode and finally a grid electrode. A schematic of the electrode configuration is shown in figure 4.4. The separating and outer electrodes are held at 0 potential. These are included to give a realistic space configuration of the actual IMP.

Table 4.4 shows the ratio of ion currents to each probe for the same biasing range as that used in the experiments (-1 to -120 V) and the corresponding graph is given in figure 4.5. A kinetic energy of 20 eV was used for the ions.

Table 4.4: *SIMION - 20eV Ions, 5 electrode config*

V_P	$V_{C(0)}$	$V_{C(-20)}$	$V_{C(-40)}$	$V_{C(-60)}$	$V_{C(-80)}$	$V_{C(-100)}$	$V_{C(-120)}$
-1	0.07	0.34	0.62	0.83	0.90	1.11	1.27
-20	0.02	0.20	0.38	0.53	0.68	0.78	0.90
-40	0.02	0.06	0.25	0.36	0.48	0.55	0.64
-60	0.02	0.02	0.14	0.28	0.36	0.48	0.55
-80	0.02	0.02	0.06	0.19	0.30	0.36	0.48
-100	0.02	0.02	0.05	0.14	0.24	0.30	0.40
-120	0.02	0.02	0.02	0.10	0.19	0.22	0.33

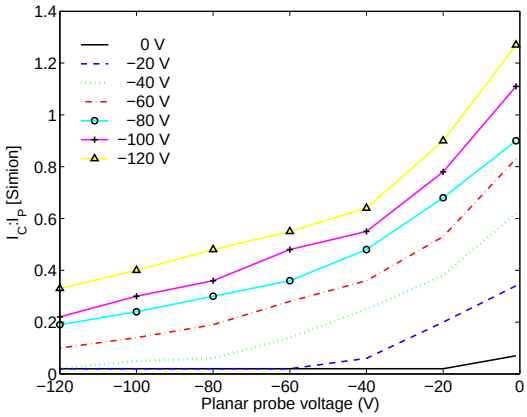

Figure 4.5: *Ratio of cylindrical ion current to planar ion current for 20 eV ions in SIMION.*

Figure 4.5 shows that the ratio of currents to each probe for this particular kinetic energy is in good qualitative agreement with the experimental values in figure 4.3.

Trajectory characteristics

Geometry from previous Simion potential arrays were changed to include a grounded boundary cylinder and an adjusted cylindrical probe length - this was increased so that it almost connects to the front grid. We can see from figure 4.6 that using a longer probe will have a significant effect on

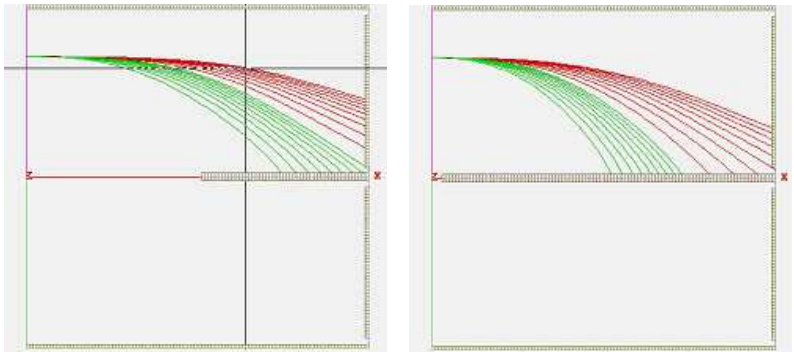

(a) 50mm cylindrical (b) 100mm cylindrical

Figure 4.6: *Effects of changing cylindrical probe length for potentials:* $V_{Cylindrical}$ *= -40 V,* V_{Planar} *= -35 V. Green trajectories = Kinetic Energies of 1 to 5 eV in 0.5 eV steps; red = KE's of 1 to 25 in 2 eV steps, mass = 40.*

the ion paths in the sampling region. Most of the ions are collected on the cylindrical probe even though the potentials are fixed.

Biasing the cylindrical probe positively has a much greater affect on ion trajectories than that of the planar probe: a +10 V bias on the cylindrical deflects all ions to the planar probe and the separation between trajectories is reduced.

A simulation with two ions of the same energy but different mass yielded the exact same trajectory indicating that mass cannot be resolved. The theoretical analysis of an electrostatic field and paraxial trajectories is given in [46] which clearly shows no mass dependence.

4.4.2 Two ion simulation

A heavy ion like Ar entering the sampling region at a particular position y, will slowly be accelerated towards the electrode until impact at position x. A lighter O_2 ion entering at the same position will have a much greater

acceleration, and therefore will hit the probe faster. As both ions experience the same accelerating potential they follow the same path (as $F = qE$ only) but will impact at different times due to their difference in mass.

Table 4.5: *Trajectory dependence on energy*

E_1 15(eV)	TOF(μs)	$x(mm)$	v$(mm/\mu s)$
$m_1 = 2$ amu	0.481735	29.0058	105.336
$m_2 = 40$ amu	2.154380	29.0058	23.5539
E_2 100(eV)	TOF(μs)	$x(mm)$	v$(mm/\mu s)$
$m_1 = 2$ amu	0.325118	36.8351	138.862
$m_2 = 40$ amu	1.453970	36.8351	31.0505

From table 4.5 it can be shown that the impact position x doesn't change when mass ($m_{1,2}$) is increased, therefore the trajectory is fixed for a given energy. This is depicted in figure 4.7. However if the energy is increased, the particle travels further before it strikes the electrode. Thus it can be said that increasing the energy

- *alters the trajectory and decreases the particle TOF and*
- *ions penetrate further with greater velocity.*

Refraction of ion trajectories results from electrostatic and/or magnetic forces normal to the ion's velocity. The radius of refraction can be determined as follows:

Electrostatic radius of refraction

$$\text{Normal electrostatic force} \;=\; \text{Centripetal acceleration}$$

$$-eE_n = \frac{mv^2}{r_n}$$

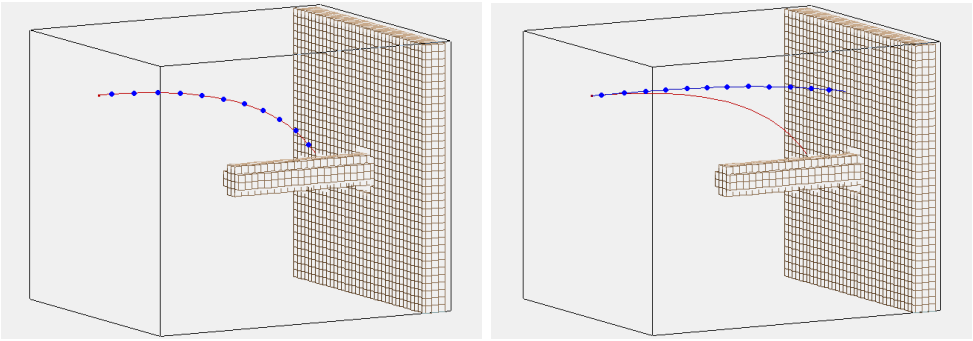

(a) KE = 15 eV (b) KE = 100 eV

Figure 4.7: *Particle trajectories for (a) blue dots [$m_1 = 2$], red [$m_2 = 40$] both at KE = 15 eV. (b) blue dots [$m_1 = 2$] at KE = 100 eV and red [$m_2 = 40$] at KE = 15 eV*

$$r_n = \frac{mv^2}{-eE_n} = \frac{-(m/e)v^2}{E_n}$$

Magnetic radius of refraction

$$\text{Normal magnetic force} \;=\; \text{Centripetal acceleration}$$

$$B_n ev = \frac{mv^2}{r_n}$$

$$r_n = \frac{mv}{B_n e} = \frac{(m/e)v}{B_n}$$

1. The electrostatic radius of refraction is proportional to the ion's kinetic energy per unit charge. Thus all ions starting at the same location, direction and kinetic energy per unit charge will have identical trajectories in electrostatic fields.

2. The magnetic radius of refraction is proportional to the ion's momentum per unit charge. Thus all ions with the same starting point, direction and momentum per unit charge will have the identical trajectories in static magnetic fields.

3. Because of the v versus v^2 effects on the radius of refraction, magnetic ion lenses have superior refractive power at high ion velocities.

Originally it appeared that the experiment followed our initial claim because the slope of the ion current in the I-V characteristic changed when small amounts of O_2 were added to a predominantly Ar plasma. However it is clear that this is due to other effects such as changes in the sheath potential, power absorption with the addition of O_2 and velocity effects. Thus it can be concluded that trajectories are mass independent in electrostatic fields and mass dependent in static magnetic fields. SIMION has shown that for a given energy, changing the mass has no effect on the ratio of currents collected. This is because the ion trajectory does not change for changing mass - only the time of flight (TOF) changes.

It is now clear that the IMP cannot resolve mass with static fields and so other possibilities must be examined. Another option for mass analysis would be the development of a miniature TOF type of analyser (which requires a long flight path with a high accuracy synchronising detector to measure the TOF's for various masses). Alternatively, the current design could be used with the application of an rf bias to one of the probes (where the pulse is used to alter the particle trajectory).

Alternative Ion Mass Probe - *Pulsed* Ion Mass Probe

By applying a constant bias to one of the probes (to repel electrons) and biasing the other probe with a 10 V_{pk-pk} pulse plus a constant potential, we should be able to alter the trajectory without changing the original probe design.

What effects would pulsing one of the probes have on the trajectory? Particles of different mass follow the same path in an E-field - only their time

of flight is dissimilar. So by applying a pulse which turns off after a short period of time, the E-field changes and so should the particle's trajectory.

4.5 Summary

A novel electrostatic probe was developed to measure ion mass. It consists of a cylindrical cylindrical probe oriented perpendicular to a planar probe. The fundamental idea is that biasing the planar probe will generate an ion flow along the length of the cylindrical probe and the ion trajectory in the sampling region will be dependent the ion mass and ion energy.

The IMP was tested in an Ar-O_2 discharges at low pressure. Measurements indicated that changing the ion content of the discharge resulted in a rate of change in the ion current. An ion optics package was used to simulate the ion trajectories and E-fields in the sampling region of the sensor.

It was found that this probe could not differentiate ion mass by dc biasing alone. Simulations in SIMION confirmed this. In SIMION, when the KE of an ion is increased, the time-of-flight decreases for a fixed mass. If KE is fixed however, the time-of-flight increases for a fixed mass but the trajectory remains the same i.e. the same flight path is taken by ions of differing mass but a heavier ion will take longer to get there.

The idea behind this probe was conceived from a mach probe used by Doggett *et al* and Sheerin [48, 49] in a laser plasma. From their simulations, the peak ion current along the length of the probe showed a slight mass dependence. Closer examination of this effect, not described here, has shown that the mass dependence in peak ion currents of species of varying mass would not be sufficient to resolve different ion species. In addition, the laser plasma environment is not a static field.

4.5 Summary

An alternative method for measuring mass with the existing design configuration would be to use an rf pulse on one of the probes. Ions entering the sample region would initially be accelerated by a negative bias on the cylindrical probe while an alternating bias on the planar probe would decelerate the ions according to their mass and the magnitude of the rf bias.

In principle a pulsed or time varying field will resolve mass but adds to the complexity and is not pursued further. However, this would be ideal for future work.

CHAPTER 5

Retarding field energy analyser

Plasma discharges are commonly used to process wafer surfaces in a variety of ways in the semiconductor manufacturing industry. Fabrication of sub-micron integrated circuits requires reliable processes that are repeatable from one tool to another, thus the ability to accurately measure plasma conditions is crucial for chamber matching and avoiding process drift. Etching and deposition rates, anisotropy, as well as surface topography are largely determined by the energy and flux of reactive species generated by the plasma [3]. In inductive discharges the ion flux is governed by the ion plasma density, which is regulated to a large extent by the input power, while the ion bombardment energy to a wafer's surface may be manipulated by the rf bias potential applied to the electrostatic chuck on which the wafer sits. By mounting a retarding field energy analyser directly on a biased electrode in an rf discharge, the ion energy distribution (IED) impacting a wafer under

various processing conditions can be determined.

For a number of decades, retarding field energy analysers (RFEA's) have been used to measure IED's in several plasma discharge configurations [54–76]. An early study by Simpson [54] compared the performance of ion energy analyser designs for a variety of ion beam parameters such as angular divergence, beam diameter, energy spread within the beam and mean energy of the beam. Coburn and Kay [55] recorded IEDs with an analyser coupled to a quadrupole. Kuypers and Hopman [58] used a planar gridded analyser in a cylindrical magnetron reactor to make in-situ energy measurements at a substrate surface, and hence derived the plasma potential, sheath thickness, and total ion current. Dual peak splitting was observed in an oxygen plasma where the peak separation, ΔE, agreed with the theoretically calculated value, which shows that heavier particles are less affected by the oscillating electric field due to their inertia. Ingram and Braithwaite developed a very compact energy analyser (~ 0.75 mm from orifice to collector plate) for measuring ion and electron energies on a grounded electrode in a capacitively coupled plasma (CCP) discharge. The compact design avoided the need for differential pumping [59, 60]. Kuypers and Hopman [61] investigated IED's at a powered electrode in a varying magnetic field. Lui *et al* [62] carried out an extensive study at the grounded electrode in a CCP reactor and compared the results with Monte Carlo simulations. Woodworth conducted a series of studies in a GEC reference cell where the main focus of the research was on measurements of ion energy and ion angular distributions at a grounded electrode [63–67]. Edelberg *et al* developed an analyser for measuring IED's at a wafer surface in a transformer coupled plasma (TCP) reactor in which the analyser was built into the electrostatic chuck [68–70]. In these studies, a sheath model was compared with experimental results and good agreement

was found. Kawamura reviewed IED's in rf sheaths conducting an in-depth analysis of previous studies, theory, experiment and models [71]. More recently, Gahan *et al* developed a floating analyser designed to sit directly on an rf-biased electrode thereby achieving practical measurements of ion distributions impinging a substrate surface [72].

In this chapter, ion energy distribution (IED) measurements taken in the ARIS reactor (an inductively coupled radio-frequency discharge) in argon, oxygen and argon-helium plasmas are discussed. The effects of discharge pressure, ICP power, rf bias voltage, bias frequency and gas composition are analysed. The energy analyser is operated at both a ground and a biased electrode. A Langmuir probe was used to characterise the discharge and a retarding field energy analyser (RFEA) measures the ion flux and energy distributions impacting the remote rf driven electrode. Comparisons are made between capacitive and direct coupling of the rf bias potential. In addition, the sensor was translated across the length of the discharge chamber to investigate the energy distribution as a function of position. Results are shown for Ar, O_2 and Ar-He discharges.

A double layer was observed to emanate from the source region while performing experiments in an O_2 discharge. This phenomenon has been observed and analysed by a number of authors over the last couple of decades [77–80]. More recent studies by Charles *et al* [77] and Plihon *et al* [78] focused on experiments in a reactor very similar to the configuration used here. A number of measurements are carried out in the presence of a double layer and will be discussed in the following sections however the main focus of this chapter will be on the behavior of ions through capacitively and directly coupled plasma sheaths.

5.1 Theoretical background

Ion energy distributions are dependent on sheath characteristics such as potential, sheath thickness and the number of rf periods, $\tau_{rf} = 2\pi/\omega$, it takes an ion to cross the sheath, i.e. the ion transit time, τ_i. The ion transit time is given by $\tau_i = 3\bar{s}\sqrt{m_i/(2e\bar{V}_s)}$ where $\bar{s}$ is the time averaged sheath width, m_i is ion mass and $\bar{V}_s$ is the dc potential across the sheath. For the low pressures ($\leq$ 1.2 Pa) used in this study, a collisionless regime may be assumed and hence the Child-Langmuir law gives the sheath thickness, $\bar{s}$

$$\bar{s} = \frac{2}{3}\left(\frac{2e}{m_i}\right)^{1/4}\left(\frac{\epsilon_0}{\bar{J}_i}\right)^{1/2}\bar{V}_s^{3/4} \tag{5.1}$$

which corresponds to a dc sheath with a potential drop of $\bar{V}_s^{3/4}$, ϵ_0 is the permittivity of free space and ion current density, $\bar{J}_i$, is given by

$$\bar{J}_i = \frac{4\epsilon_0}{9}\left(\frac{2e}{m_i}\right)^{1/2}\frac{\bar{V}_s^{3/2}}{s^2} \approx 0.61 e n_0 u_B. \tag{5.2}$$

Here, n_0 is the bulk plasma density, the Bohm velocity, u_B, is given by $\mathrm{u}_B{=}\sqrt{k_B T_e/m_i}$ where $k_B T_e$ is the electron temperature in eV.

In low frequency cases where $\tau_i/\tau_{rf} \ll 1$, ions cross the sheath in a fraction of an rf cycle and respond to an instantaneous sheath voltage rather than a time averaged value. As a result, their energies depend on the phase of the rf cycle at the time they enter the sheath. This gives a distribution that is broad and bimodal where the separation of the peaks, ΔE, in the IED is approximately equal to the maximum sheath potential. The low and high energy peaks in the distribution correspond to the minimum and maximum sheath potentials respectively.

In high frequency cases ($\tau_i/\tau_{rf} \gg 1$), the ions cross the sheath over a number of rf cycles and respond to an average sheath voltage where the phase of the cycle in which they enter the sheath becomes insignificant. This

results in a narrower IED. Benoit-Cattin and Bernard developed an analytical model for calculating ΔE in a collisionless sheath when $\tau_i/\tau_{rf} \gg 1$ [81].

The flux of ions, Γ_i, that enter the sheath at time t_0 will hit the surface at time t_f with energy E

$$\frac{\omega}{2\pi}\Gamma_i(\omega t_0)dt_0 = f(E)dE \tag{5.3}$$

and the number of ions entering the sheath per unit time must equal the number of ions within an energy interval dE, resulting in an energy distribution given by

$$f(E) = \frac{dn}{dE} = \frac{2n_t}{\omega\Delta E}\left[1 - \frac{4}{\Delta E^2}(E - e\tilde{V}_s)^2\right]^{-1/2} \tag{5.4}$$

where n_t is the number of ions that enter the sheath per unit time, $\tilde{V}_s$ is the amplitude of the rf component of the sheath voltage and the mean energy, E, is equal to $e\bar{V}_s$. The energy splitting of peaks is given by:

$$\Delta E = \left(\frac{8e\tilde{V}_s}{3\omega d_s}\right)\left(\frac{2e\bar{V}_s}{m_i}\right)^{1/2} = \frac{3e\tilde{V}_s}{\pi}\left(\frac{\tau_{rf}}{\tau_i}\right) \tag{5.5}$$

where d_s is the time averaged sheath thickness and $\bar{V}_s + \tilde{V}_s sin(\omega t)$ is the oscillating voltage across the sheath. Thus we can see that ΔE is proportional to τ_{rf}/τ_i and inversely proportional to $\sqrt{m_i}$.

5.2 Experiment

5.2.1 Experimental Apparatus

The experimental reactor used in this study is an expanding inductive source design. A thorough description of the system has been given in chapter 3. Briefly, it consists of a source region and an expansion chamber. A diagram of the apparatus is given in figure 5.1. The source consists of a quartz tube

(100 mm diameter, 150 mm length) closed at one end with a stainless steel cap. The other end is connected to a larger cylindrical expansion region with a 420 mm diameter and length of 290 mm which is terminated with a stainless steel end plate. All metal surfaces of the chamber are grounded. In the source region, power is inductively coupled through a two-turn copper antenna surrounding a quartz tube and is driven at 13.56 MHz. Gas is supplied to the expansion region via a mass flow controller and pumped with a turbo molecular pump.

There are numerous access ports on the walls and end plate of the expansion chamber for applying diagnostics. The RFEA was mounted on the surface of a 60 mm diameter aluminium electrode located in the center of the end plate directly opposite the source. This electrode is mounted in a teflon (PTFE) holder and rf power is supplied to the electrode by a wide band amplifier through a 0.47 pF blocking capacitor when used in capacitive coupling mode. Cabling for the RFEA was fed through one of the vacuum ports on the sidewall of the expansion chamber. Current and voltage probes attached to the power lead of the biased electrode monitored voltage and current waveforms as described by Gahan *et al* [82–84]. For the majority of tests carried out, a constant power of 300 W was used to sustain the plasma at a pressure of 0.2 Pa in argon discharge, unless otherwise stated.

5.2.2 Retarding Field Energy Analyser

The ion energy analyser used in this study is a planar gridded energy analyser [50], which is mounted on an electrode in the expansion chamber of the inductive reactor. As the analyser design is compact ($\approx$ 0.6 mm), differential pumping is not required for the pressure range of interest since the ion mean free path, λ, is greater than the distance traveled by the ions within

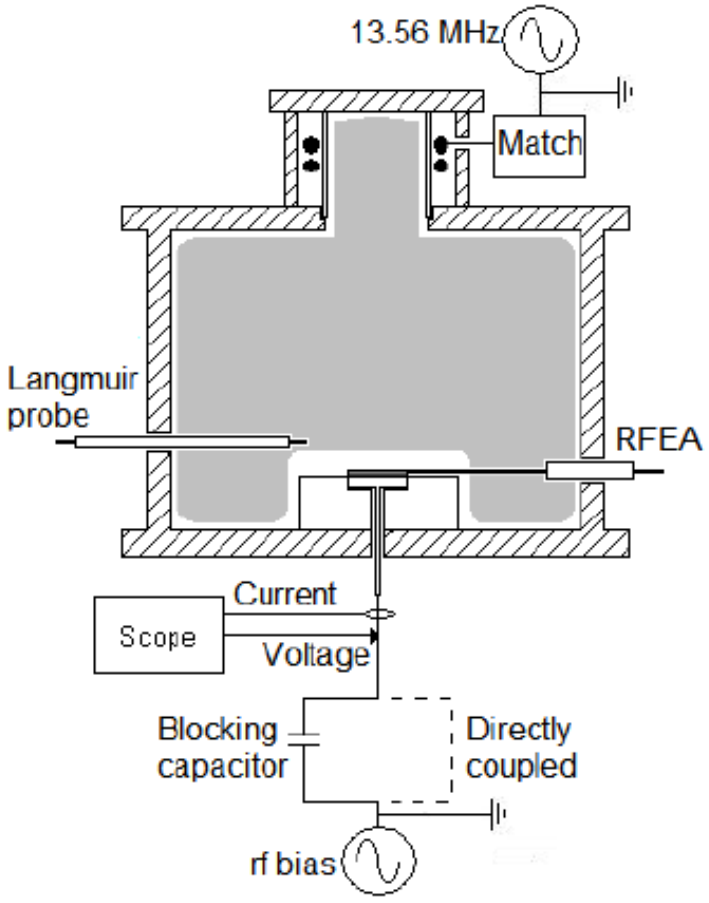

Figure 5.1: *The experimental reactor with the retarding field energy analyser mounted on the end plate.*

the analyser. At the highest pressure used (1.2 Pa), λ is given by $\lambda=1/\sigma n_g$, where σ is momentum transfer collision cross section and n_g is neutral density. Therefore at 1.2 Pa, $\lambda \gg 0.6$ mm. A schematic of the energy analyser is shown in figure 5.2. It consists of a series of grids located behind a sampling aperture and is terminated by a collector plate. The analyser is 60 mm in diameter and 3 mm thick. An array of 800 μm holes over an area of 1 cm^2 is used. The actual sampling area is $\ll 1$ cm^2 and the 800 μm holes are covered by the first grid, G_1, to reduce the orifice size open to the plasma. Insulating spacers separate the grids which have a 18 μm hole size and a transparency of 50%, from the collector plate.

G_1, is electrically connected to the body of the sensor and maintained at the electrode floating potential. A second grid, G_2, is swept to provide the ion retarding potential. Only ions with energies greater than the voltage on this discriminating grid (G_2) will be detected. The third grid, G_3, is biased negatively with respect to G_1 (to repel electrons that may enter the analyser and to inhibit secondary electron emission from the collector). Finally a collector plate, C, which is biased with a negative potential to attract any ions passing through G_2, terminates the analyser. For each bias step applied to G_2, the corresponding current at the collector is recorded. The ion energy distribution is obtained by taking the derivative of the collector current versus retarding potential characteristic.

5.2.3 Cabling, filtering and electronics

Cables are taken from the RFEA and brought to a vacuum feed-through with a re-entrant ceramic tube in which the rf filters are mounted. The cables, sealed in a flexible ceramic shield, are resistant to discharge temperatures up to 400^{o}C and to reactive species that may be present in the processes under

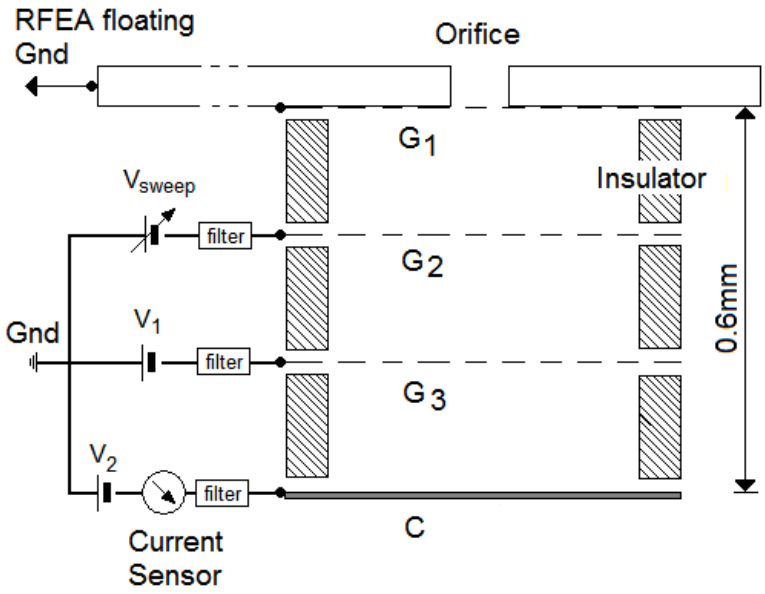

Figure 5.2: *Cross section of the retarding field energy analyser.*

investigation. The re-entrant ceramic tube forms the connection between the vacuum side of the chamber and atmosphere through an o-ring sealed vacuum feed-through. The RFEA cables enter the ceramic tube on the vacuum side where they are connected to the filters. The output end of the filters are then taken to the measurement electronics from the external side of the ceramic tube. This design is similar to that used for commercial compensated Langmuir probes [13].

Each cable connected to the RFEA has a filter arranged in an inductor-resistor-capacitor (LRC) configuration. The attenuation provided by such a filter terminated at the RFEA measurement electronics, is given in figure 5.3 [72]. The rf potential at the output is at least 60 dB lower than that applied to the input over the range from 500 kHz to 60 MHz. This range covers some of the most common frequencies used in low temperature rf plasma processes.

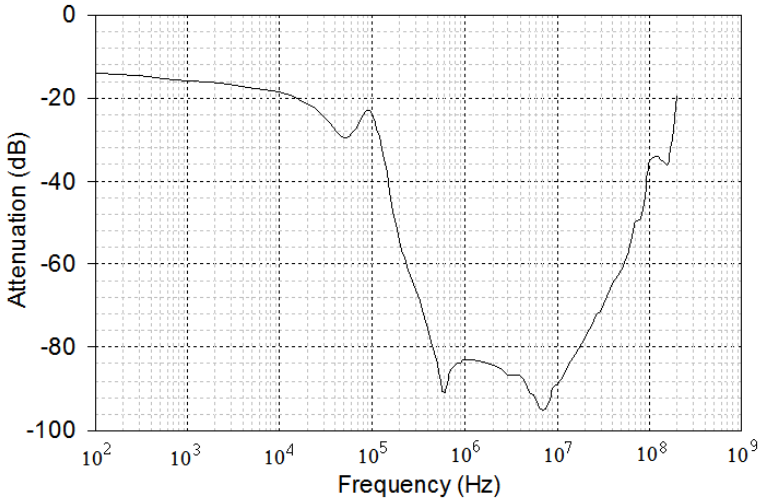

Figure 5.3: *Attenuation provided by filters as a function of frequency.*

The requirements on the filter input impedance are that a) it is large relative to that of the rf electrode on which it is mounted to maintain a fixed impedance to ground and b) it is large compared to the impedance associated with the capacitance between the RFEA internal grids and its outer casing. The first criterion would be important for systems that apply the rf bias through a matching unit. If the electrode impedance to ground is different when the analyser is in place then the matching condition, and thus, rf bias potential, is different. Consequently, for a set rf bias power the IED at the electrode would be different without the analyser - defeating the purpose of the measurement. The second criterion ensures that the rf potential on the electrode/RFEA casing is strongly coupled to the internal grids. This prevents significant potential drop across the grid-casing capacitance. In figure 5.4 [72] the measured input impedance of the filter is given along with the impedance to ground of the electrode (calculated from its capacitance $\approx$ 50 pF) and the impedance between any grid and the RFEA casing (also calculated from its capacitance $\approx$ 300 pF). It is clear that the filter input

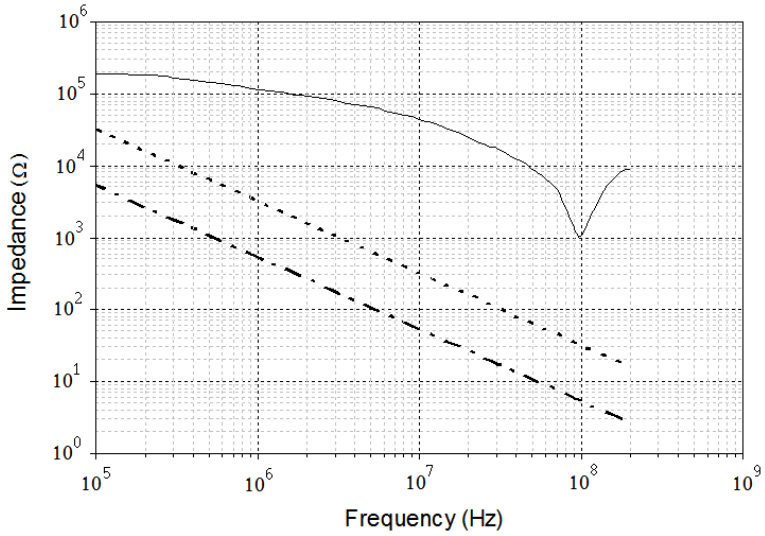

Figure 5.4: *Filter input impedance (solid line), electrode impedance to ground (dashed line) and grid impedance to casing (dot-dashed line) as a function of frequency.*

impedance is significantly greater than both over the frequency range of interest. This means that there is no significant loading of the electrode impedance and that there is a negligible difference between electrode rf bias and grid rf bias.

The measurement electronics used has three output voltage channels with a range of -150 V to +150 V. Two of these channels are set to a constant output level to bias the collector plate and the plasma electron repelling grid. A third channel sweeps the discriminator from the sensor floating potential to about 20 V above the dc plasma potential to cover the range of energies that ions crossing the sheath may have. For each step in the voltage scan series, the collector current is determined to construct the current-voltage characteristic. Data is transferred via a universal serial bus (USB) connection from the I-V scanner to a PC for analysis. As the RFEA is floating at the dc self bias of the rf driven electrode on which it is mounted (as would a

wafer under processing conditions), the bias voltages applied to the grids and collector need to be referenced to this potential to obtain the actual ion energies.

5.2.4 Langmuir Probe

A Langmuir probe [85] was employed to monitor electron density and electron temperature as a function of pressure and ICP power. A detailed description of probe theory has been given in section 1.5 and the probe configuration is described in section 2.2.3. In these experiments, a tungsten probe tip, 5 mm in length with a radius of 0.195 mm is used. The probe is positioned approximately 1 cm above the outer edge of the RFEA platen.

5.3 Source characterisation

In order to understand variations in the structure of IED's measured at the rf biased electrode, as a function of source power and discharge pressure, it is first useful to investigate the dependencies of plasma parameters (near the electrode) on these two main discharge variables.

5.3.1 Langmuir probe measurements of T_e and n_e in argon

In figure 5.5 the variation of plasma parameters T_e and n_e obtained with the Langmuir probe system, versus input power and pressure respectively in an argon discharge is shown. These parameters are used for calculations throughout the results sections. The probe was cleaned periodically between scans by electron bombardment whereby a large bias is applied to the tip

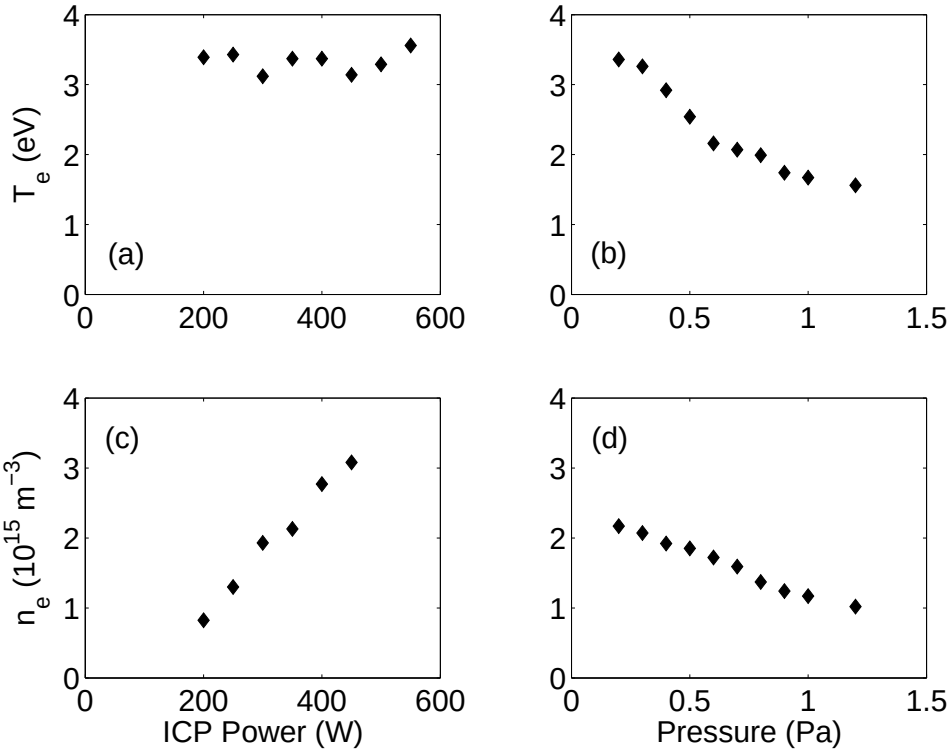

Figure 5.5: *(a) T_e as function of ICP power at 0.2 Pa, (b) T_e as function of pressure at 300 W, (c) n_e as function of ICP power at 0.2 Pa and (d) n_e as function of pressure at 300 W.*

(+150 V). This helps prevent surface contamination which leads to distortion of the IV trace. The plasma potential V_p was determined from the point where the second derivative of the IV trace crosses zero. Here, T_e was determined using a linear fit to the natural log of probe current versus voltage characteristic. The electron density, n_e was determined from

$$n_e = \left(\frac{I_{(V_p)}}{A_p}\right)\left(\frac{2\pi m_e}{eKT_e}\right)^{1/2}, \tag{5.6}$$

where $I_{(V_p)}$ is the current at the plasma potential and $A_p$is the area of the probe.

Increasing the applied power lead to an increase in electron density with

little variation in electron temperature as shown in figure 5.5(a) and (c). It is thought that electron losses due to thermal conductivity may be the reason for an almost constant T_e when the power is increased [86]. In figure 5.5(b) T_e decreases with increasing pressure as expected [7]. At higher pressures, the electron mean free path is reduced causing the decrease in T_e. In figure 5.5(d) a decrease in n_e with increasing pressure is seen. It is expected that n_e in the source region increases with increasing pressure over the range investigated. The ratio between n_e in the diffusion chamber to that in the source region is likely to decrease due to enhanced collisions as the pressure increases. This may explain the drop in n_e shown.

5.3.2 Calibration of RFEA

Initially, the operation of the RFEA was tested with the remote electrode at ground. Figure 5.6 shows the IEDs obtained in an argon discharge for a range of pressures from 0.3 - 2.0 Pa. At low pressure, the ions are accelerated from the bulk to the electrode acquiring an energy equal to the dc sheath potential. The IEDs are narrow single peaked structures relating to the average energy gained by ions crossing the sheath. The peaks of these IEDs were compared with the dc plasma potential measurements taken with a Langmuir probe as shown in figure 5.7. Here it is shown that the plasma potential as measured by the peaks of the IEDs taken with the analyser and the FWHM shown by the bars are in good agreement with those of the Langmuir probe data. These measurements are also in good qualitative agreement with previous authors work [69].

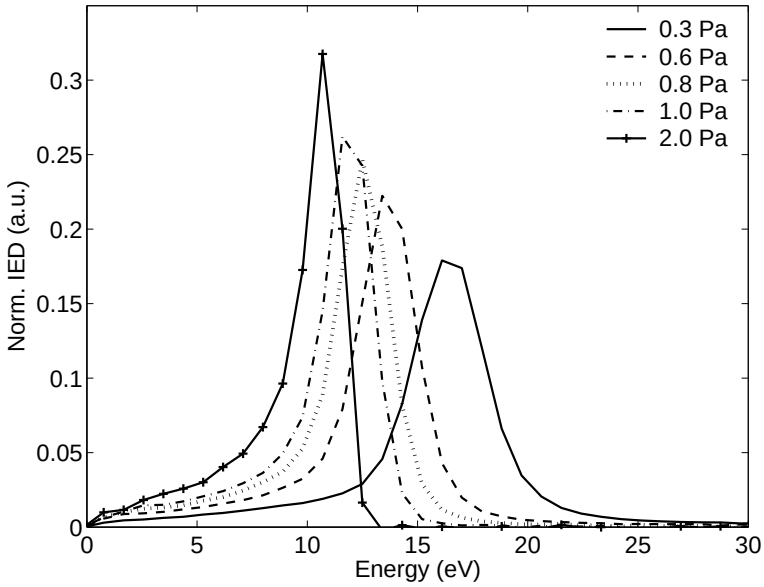

Figure 5.6: *Ion energy distribution of Ar as a function of pressure at 300 W ICP power, with the remote electrode at ground.*

5.3.3 Other source characteristics

In this section some more details on the operation of the source are given. For this purpose the electrode was removed and the RFEA was mounted on a moveable, grounded, feed-through and IED's were measured along the axis of the discharge as illustrated in figure 5.8. It is worth noting that the focus of these experiments is to compare the structure of the IED for capacitive and direct coupling of the rf bias to the remote electrode. The purpose of this section is give the reader a brief insight into the characteristics of this particular reactor configuration.

Axial plasma potential variation

In the following experiments the position where the source region meets the expansion chamber is defined at 0 mm. The range of translation of the

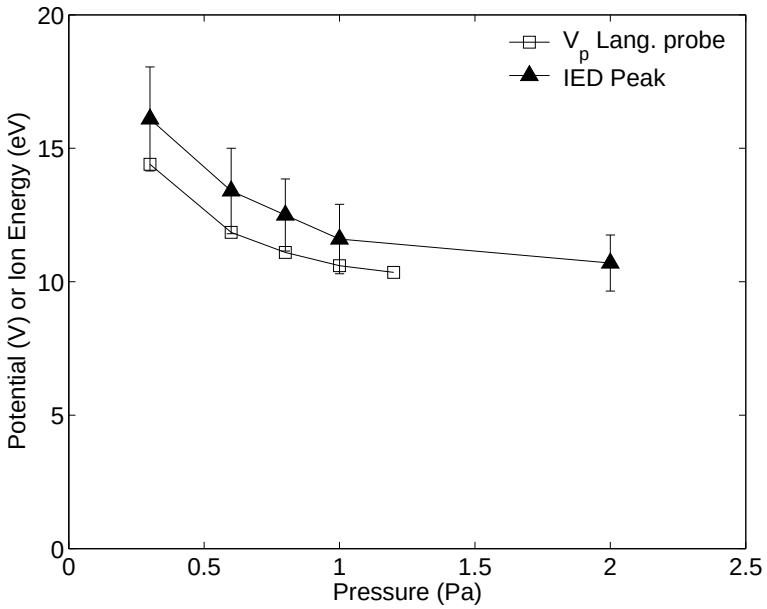

Figure 5.7: *Comparison of the plasma potentials measured with a Langmuir probe and the RFEA as a function of pressure in an Ar plasma at 300 W, with the electrode at ground. Note: the error bars represent the FWHM of the IED measured by the RFEA.*

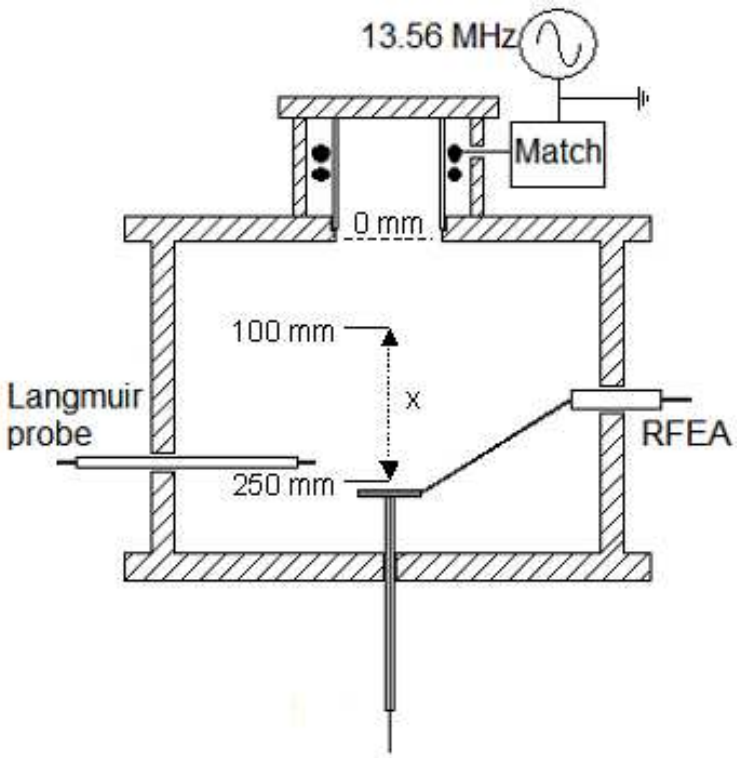

Figure 5.8: *The experimental chamber with the retarding field energy analyser mounted on a translational feed-through moving from 250 mm (at the back of the expansion chamber) to 100 mm (close to the source region).*

feed-through is from 250 mm (where the RFEA is furthest from the source) to a position 100 mm from the source (closest to the source). For these measurements, the ICP power was held constant at 300 W, the RFEA was grounded and the pressure fixed at 0.2 Pa. Figure 5.9 shows axial IED's in (a) argon and (b) oxygen to highlight the source behavior in both electropositive and electronegative discharges.

Since, in this section, the RFEA is grounded the ions reaching its surface have a mean energy equivalent to the dc plasma potential. The plasma potential oscillation due to the source frequency (13.56 MHz), measured with a floating probe, is less than 5 V. The oscillation of the sheath, generated by the small plasma potential oscillation has a period which is short relative to the ion transit time. The ions are not modulated by the source frequency at position x = 250 mm and we can ignore the 13.56 MHz voltage oscillation, effectively yielding dc sheath behavior. Therefore the IED responds mainly to the time averaged sheath potential and is essentially mono-energetic.

Figure 5.9(a) shows a series of IED's taken in an argon discharge starting at the position where the electrode is normally located and moving towards the source region. Similarly in figure 5.9(b) IED's in an oxygen discharge as a function of position are shown. In figure 5.9(c) the dc plasma potential variation for both are compared. The plasma potential is taken to be at the peak of the IED. For the argon case the dc plasma potential rises almost linearly from the back of the chamber towards the source from 17.9 V to 25.0 V. The IED's measured in oxygen have a more complicated structure. At the 250 mm location a narrow bimodal IED was obtained. Towards the source the IED becomes single peaked again. When a bimodal structure is observed it means that the ions are responding to the oscillation in the plasma potential. This is possible in oxygen as the positive ions are lighter

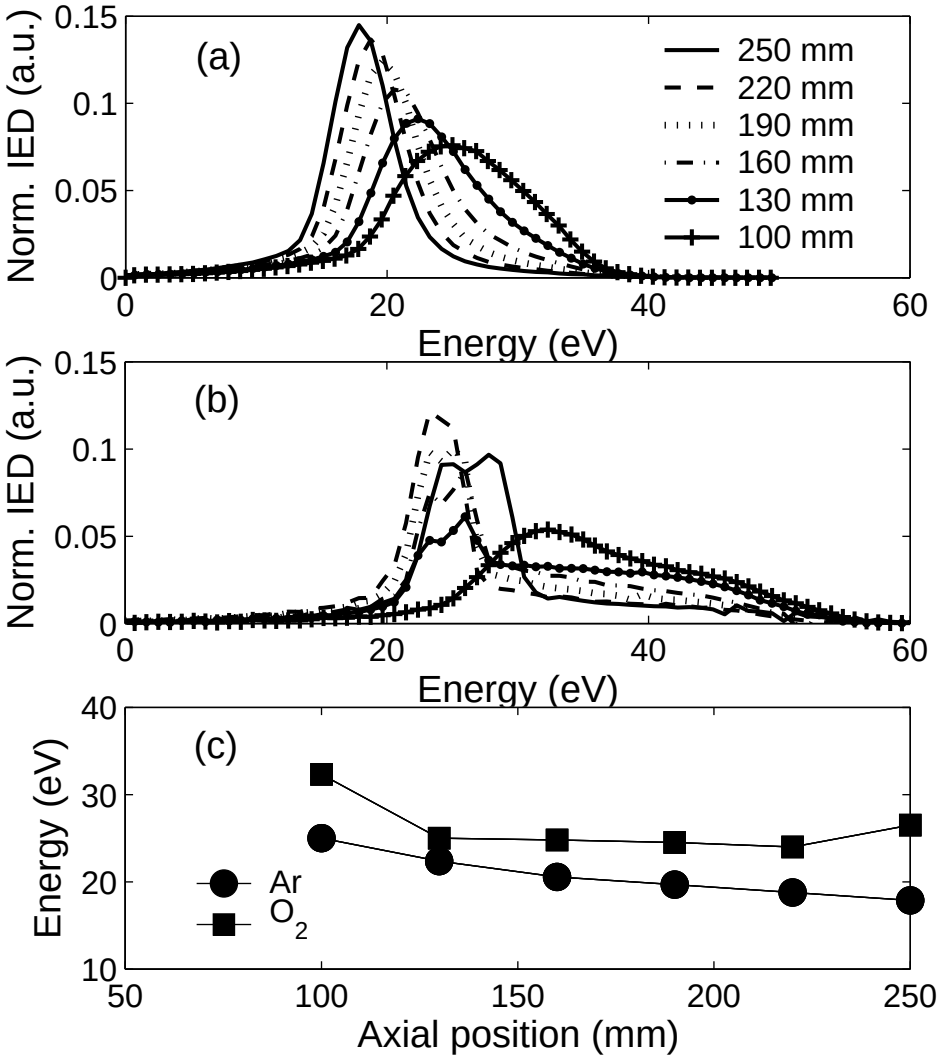

Figure 5.9: *IED's as a function of axial position for (a) Ar and (b) O_2 in a 0.2 Pa, 300 W, Ar discharge with the electrode at ground. (c) V_p as a function of axial position (mm) for Ar and O_2.*

than in argon. The plasma potential is now taken as the midpoint between the two peaks. The plasma potential in oxygen initially drops from 26.5 V then rises to 32.3 V closer to the source. For this reason we do not present capacitively and directly coupled data for oxygen as it doesn't exhibit the same dc-like sheath behavior as in argon.

Another interesting characteristic in the oxygen IED's is the presence of a high energy tail in the distribution, most prominent closest to the source. This effect is attributed to formation of a double layer (DL) [77] between the source region and the expanding region. This DL separates two plasma regions of significantly different composition and plasma potentials. The two regions are separated by a sheath potential that accelerates a beam of positive ions out of the source. These ions cause the high energy tail in the measured IED's.

Double layers in oxygen discharges

Double layers are encountered in a diverse range of plasmas, from discharge tubes to space plasmas [77, 80]. A double layer (DL) is a permeable structure in a plasma which separates two boundary layers of opposite sign with a large potential difference. Current-free double layers are formed at the interface between two plasma regions with dissimilar features, which in this case is the upstream source region and the downstream expansion region. Plihon [78] found that DL's formed for a particular density of negative ions with concentrations of SF_6 between 8% and 13%. Their DL separated the high electronegative downstream plasma $(n_-/n_e) \sim 12$ from the low electronegative upstream plasma $(n_-/n_e) \sim 2$ where n_- is the negative ion density.

It was proposed by Meige [80] that the source region is ionization dominated and the expansion region is attachment dominated due to electron

radial loss combined with heating in a localised area. This results in a DL separating plasmas of differing electron temperatures e.g. high T_e in upstream region and a low T_e in the expansion region downstream. Electron-neutral collisions limit plasma diffusion along the expansion axis leading to an electron density and plasma potential profile that decrease away from the source. As a result of this decrease in potential, positive ions are accelerated towards the expansion chamber and conversely, negative ions towards the source. When the respective charged species reach the Bohm velocity, quasineutrality breaks down and an internal sheath or double layer is formed. The electric field across a DL maintains a balance between accelerated electrons flowing upstream and ions flowing in the other direction [77].

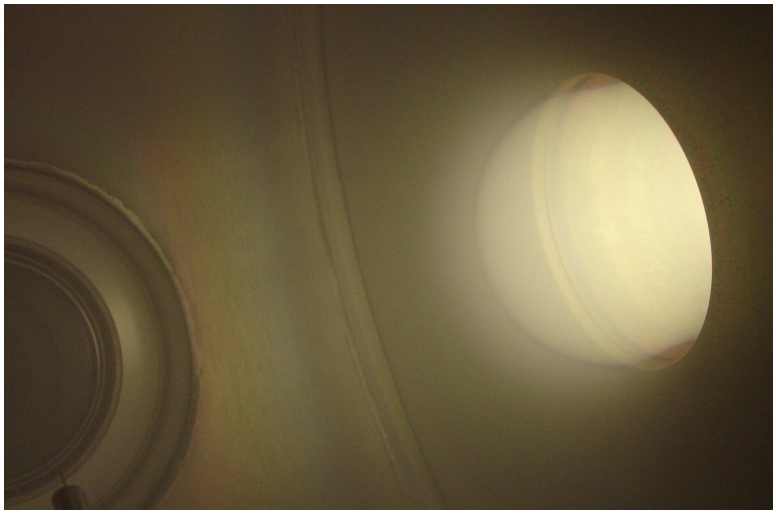

Figure 5.10: *Photograph of a Double Layer extruding from the source region at 0.2 Pa in an O_2 plasma at low power (55 W).*

In the experiments presented, a DL was observed for both high (300 W) and low power (55 W) modes of operation in a low pressure oxygen discharge. A photograph of a double layer taken in such a discharge at 55 W is given in figure 5.10. The double layer is seen to protrude from the source region

of the discharge chamber. A number of the measurements were taken in the presence of the double layer, these included operating the RFEA with the electrode at ground, and sustaining the plasma in inductive and capacitive mode. When the electrode is grounded, an rf modulated sheath is no longer present resulting in IED's that are narrow single peaks [69, 72] as discussed above.

The RFEA has been shown previously to be an important diagnostic for investigating discharges with double layers [77]. Figure 5.8 shows a schematic of the moveable RFEA. Figure 5.11(a)[1] and 5.11(b) show IED's for a grounded RFEA plotted as a function of position for high (300 W) and low (55 W) powers. In the latter case, the peaks are well defined and narrow unlike those at 300 W which are much broader and exhibit double peaks for most sensor positions. At 55 W the peaks are shifted to higher energies, compared to those at 300 W, corresponding to higher dc plasma potential (see figure 5.11(c)). For the high power case (5.11(a)), double peaks are visible. At 250 mm the IED is slightly bimodal indicating that the oxygen ions are able to respond to the plasma potential oscillation at 13.56 MHz. A small high energy tail is also present due to an ion beam accelerated from the source by the DL. At 160 mm the bimodal structure is lessened, indicating a reduction in plasma potential oscillation upstream. The high energy tail is more pronounced. At 100 mm the bimodal structure has disappeared but the high energy tail now resembles a peak which corresponds to the average beam energy accelerated across the DL. Figure 5.11(b) shows IED's taken at 55 W where no bimodal structure is present, meaning either the plasma potential oscillation is less or that due to a much lower plasma density the ion transit time across the sheath is much longer. The peaks due to the

[1]Note: figure 5.11(a) is the same as figure 5.9(b)

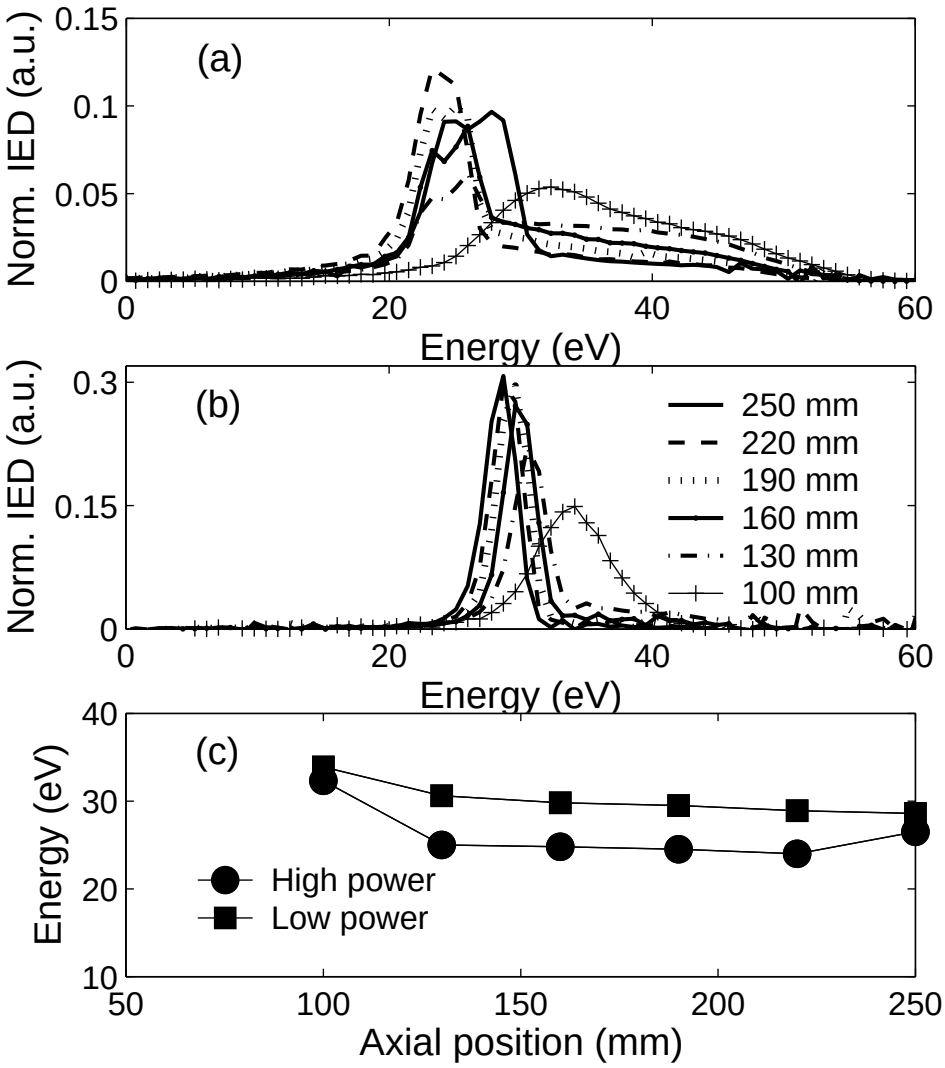

Figure 5.11: *IED's as a function of axial position for an O_2 discharge where (a) is at high power [300 W ICP power] and (b) is at low power [55 W] at 0.2 Pa. (c) V_p as a function of axial position (mm) for high and low ICP power coupling.*

thermal ions accelerated across the sheath potential are relatively large and therefore the ion beam component from the DL is hardly visible in the IED's at low power even though the DL is clearly visible (see figure 5.10).

As discussed by previous authors [77, 78] the DL in electronegative discharges is only present at low pressures (< 1.2 Pa). In figure 5.12(a) and 5.12(b) IED's are given for 300 W as a function of position at 0.2 Pa and 1 Pa respectively. At 0.2 Pa the high energy tail attributed to the DL accelerated ion beam is clearly visible at all RFEA positions. When the pressure is increased to 1 Pa the high energy tail decreases as the DL becomes insignificant. Figure 5.12(c) shows the plasma potential variation at both pressures as a function of position. In both cases the plasma potential initially drops moving towards the source.

5.4 IED at a rf biased electrode in argon

A comparison between a capacitively coupled and a directly coupled rf biased electrode

In the following sections IED's measured at an electrode with a capacitively coupled rf bias are compared to those measured at the same electrode with a directly coupled rf bias. For the capacitively coupled case the rf bias voltage is coupled to the electrode through a 0.47 pF blocking capacitor as shown in figure 5.1. This allows a dc self-bias to develop on the electrode surface. For the directly coupled case, the blocking capacitor is removed and the rf bias is applied directly to the electrode. In this configuration, no dc self-bias can develop since the electrode is now dc grounded. Base conditions for all measurements unless otherwise stated are as follows: 300

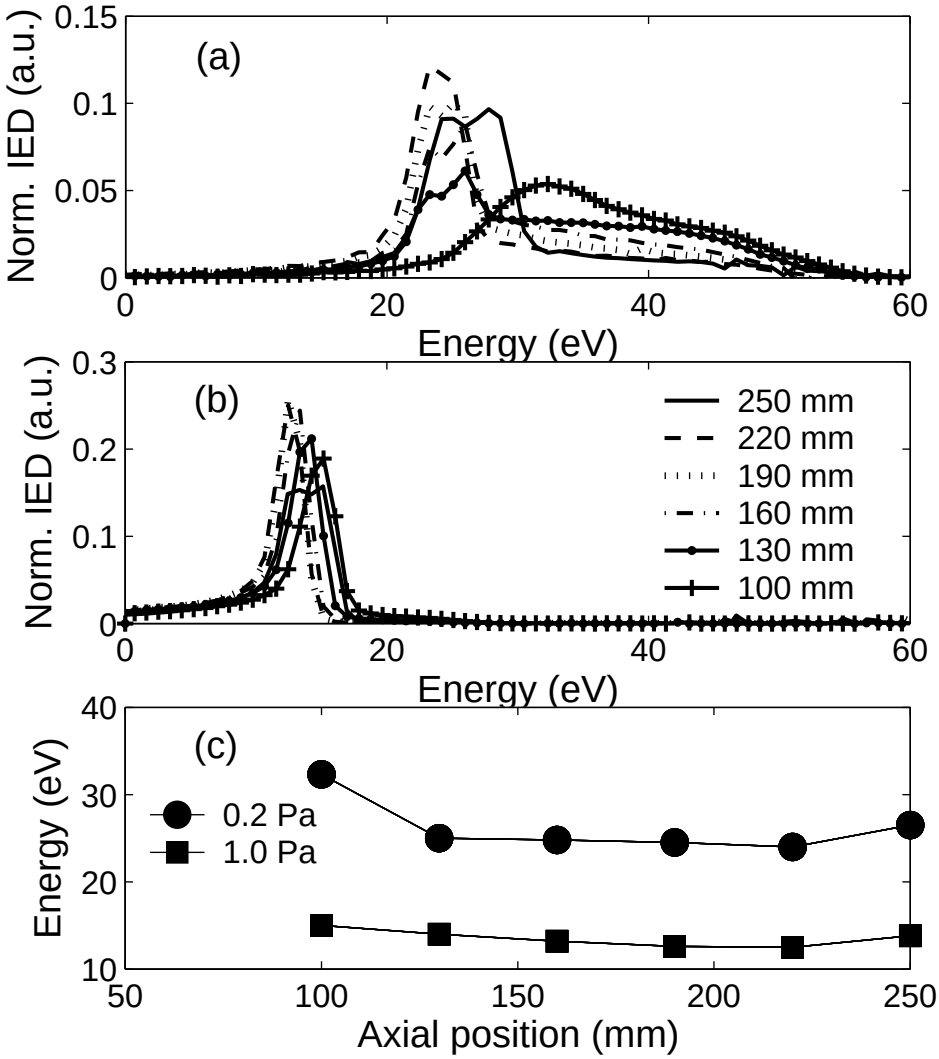

Figure 5.12: *IED's as a function of axial position for a (a) 0.2 and (b) 1.0 Pa, 300 W, O_2 discharge with the electrode at ground. (c) V_p as a function of axial position (mm) for 0.2 and 1.0 Pa.*

W ICP power, 37.5 V_{pk} rf bias potential, 2 MHz applied frequency and 0.2 Pa discharge pressure. Figures 5.13-5.16 and figure 5.18 show the IEDs obtained in an argon discharge as a function of pressure, rf bias, ICP power and bias frequency respectively. These figures compare capacitive and direct coupling of the rf bias for each of the above mentioned parameters. In each case the IED is obtained by taking the derivative of the normalized IV-trace. Figure 5.19 shows peak separation ΔE versus electrode rf bias potential and compares capacitively coupled measurements with those of the directly coupled configuration as well as theoretically calculated values for ΔE. In figure 5.17, an IED with an apparently negative energy peak is shown for data taken in an argon discharge in directly coupled mode. Figures 5.18 and 5.19 show IEDs as a function of frequency and the corresponding variations in ΔE respectively. Theoretical calculations to the measured IED's are made throughout the following sections using the Langmuir probe measurements shown in figure 5.5.

5.4.1 Effect of pressure

In figure 5.13, ion energy distributions as a function of pressure are shown for (a) capacitively coupled, and (b) directly coupled electrode rf bias. The IED peak separation, ΔE, decreases with increasing pressure in each case. The ion transit time, τ_i was calculated for the pressure range of interest. At 0.2 Pa, the capacitively coupled sheath width (from equation 5.1) $\bar{s} = 1.97$ mm where $\bar{V}_s = 41.8$ V is taken from the midpoint of the IED. The transit time is then $\tau_i = 3\bar{s}(m_i/2e\bar{V}_s)^{1/2} = 416$ ns. At 0.6 Pa and 1.2 Pa, $\tau_i =$ 587 ns and 663 ns respectively. The transit time for the directly coupled rf bias can be calculated in the same way. It is clear that the ion transit time increases as the pressure increases. Since the rf bias frequency and

amplitude remain fixed the result is an energy distribution which becomes less modulated and consequently narrower, with increasing pressure. The dc sheath potential is estimated from the center of the IED. In figure 5.13(a) this midpoint remains reasonably constant. As pressure is increased, the dc plasma potential decreases and consequently the applied rf bias changes the dc self bias of the electrode keeping the sheath potential constant. In figure 5.13(b) the center of the IED drops with increasing pressure. Here, the rf bias is directly coupled and the electrode is dc grounded. As a result the applied rf bias can no longer adjust the electrode self bias and so the dc sheath potential falls with decreasing dc plasma potential. A drop in energy of both the high and low energy peaks may be expected. However, during the positive excursion of the rf bias, when the instantaneous electrode potential approaches the plasma potential, the plasma potential appears to be pushed to a higher plasma potential [56, 57]. This is evident from the fact that the low energy peak remains constant. When the electrode potential tries to exceed the positive plasma potential, the plasma potential adjusts itself to remain the most positive potential in the discharge to prevent rapid plasma electron loss.

5.4.2 Effect of ICP power

Figure 5.14 shows the IEDs obtained for a series of ICP power inputs. In this case, the capacitively coupled IED has energy splitting that is slightly greater than those of directly coupled mode and both increase with power. In figure 5.14(a) ΔE increases with increasing ICP power because τ_i decreases (452 ns, 370 ns and 305 ns at ICP powers 300, 400 and 500 W respectively) with increasing power. From equation (5.5) ΔE = 41.5 eV, 46.0 eV and 47.8 eV respectively for each power setting. The sheath potential remains

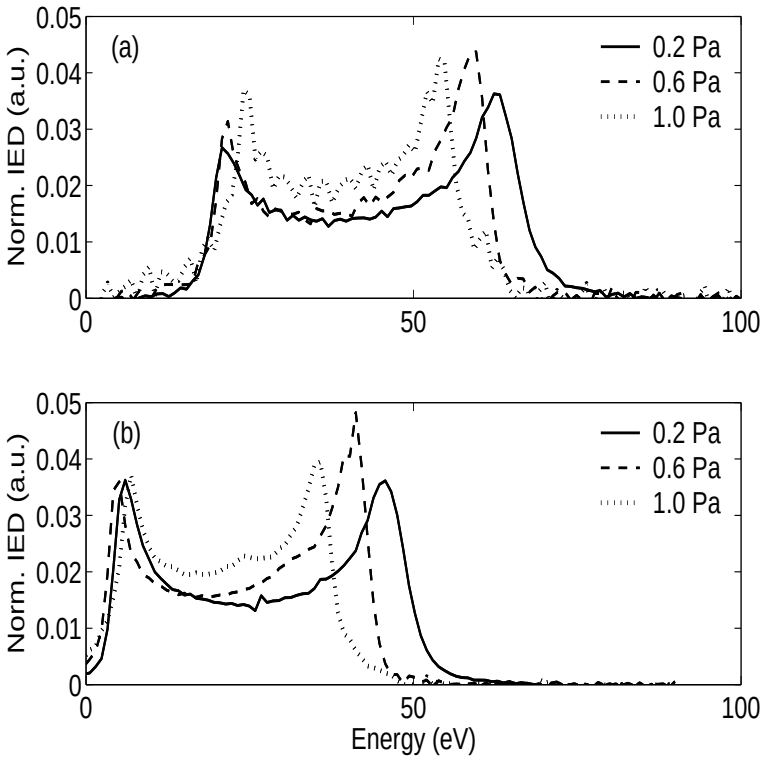

Figure 5.13: *Ar IED plots as a function of Pressure: (a) capacitively coupled; (b) directly coupled, at a fixed bias of 37.5 V_{pk} at 2 MHz and ICP power of 300 W.*

constant, not surprisingly as the plasma potential also remains constant as a function of power. In figure 5.14(b), again, the plasma potential adjusts in order to remain more positive than the instantaneous electrode potential. As the electrode potential approaches the plasma potential, it pushes the plasma potential more positive. There is also a decrease in ion transit time as a function of increasing power, causing an increase in the high energy peak location. Since it has been established that the low energy peak location is fixed directly coupled mode, the greater ΔE in capacitively coupled mode is explained because the low energy peak is free to move because the dc self-bias is adjusted by the rf bias potential (ΔE is 39.7 eV at 300 W and 44.2 eV at 500 W for the directly coupled case compared to 41.5 eV and 47.8 eV for the capacitively coupled case).

5.4.3 Effects of rf bias potential

Figure 5.15(a) and 5.15(b) show the ion energy distributions for a series of rf bias potentials applied to the electrode in a 300 W Ar discharge at 2 MHz. Both coupling modes show identical peak separation values. In 5.15(a), increasing rf bias causes both an increase in ΔE, described by equation (5.5), and an increase in sheath potential. Unlike the directly coupled rf bias, as in section 5.4.2, where the electrode bias forces the plasma potential more positive, the capacitively coupled rf bias causes the dc self bias electrode potential to become more negative. This also prevents significant plasma electron loss. Increasing the rf bias potential causes a more negative dc electrode self bias, with respect to the dc plasma potential, and therefore an increased dc sheath potential. In 5.15(b) the electrode is grounded so the self bias cannot develop. The positive excursion of the the electrode potential appears to push the plasma potential more positive in this portion of the

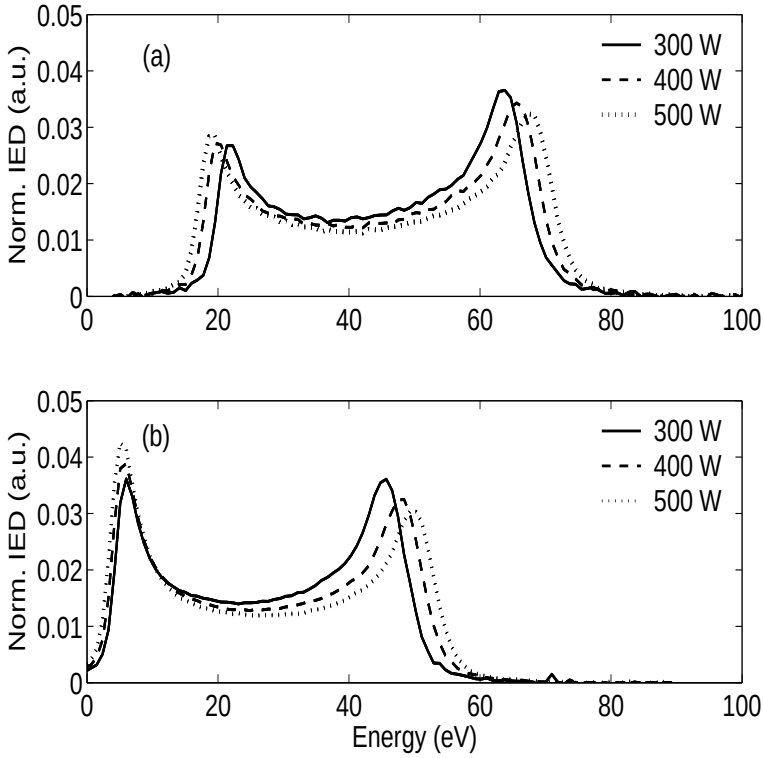

Figure 5.14: *Ar IED plots as a function of ICP power: (a) capacitively coupled; (b) directly coupled, at a fixed bias of 37.5 V_{pk} at 2 MHz and pressure of 0.2 Pa.*

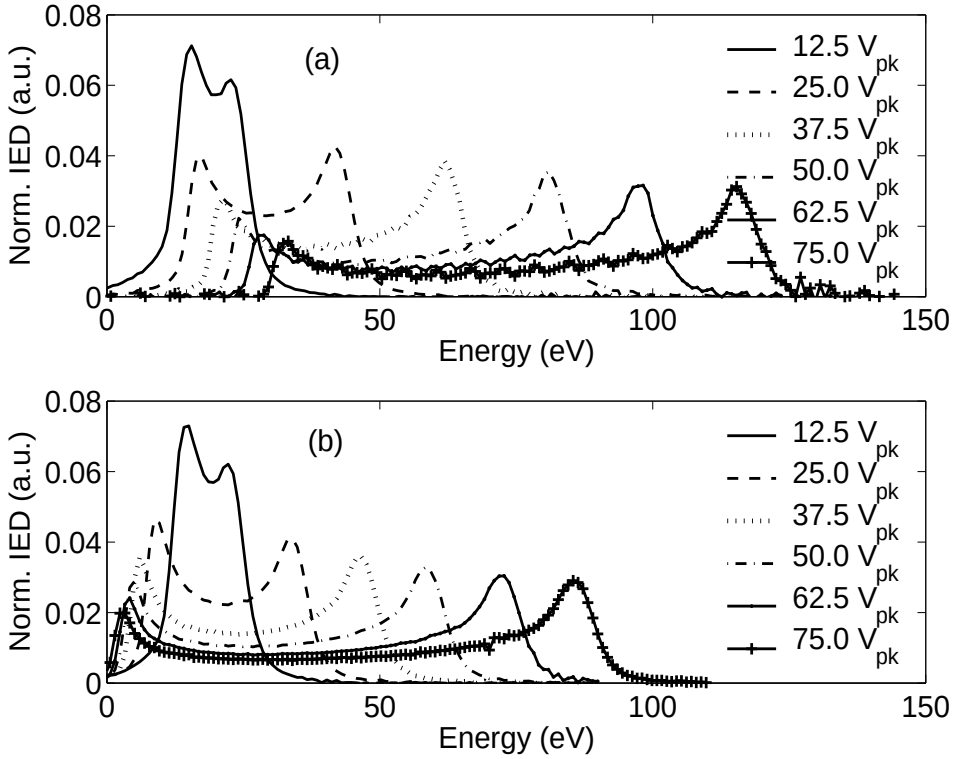

Figure 5.15: *Ar IED plots as a function of rf bias potential: (a) capacitively coupled; (b) directly coupled, at a fixed power of 300 W at 2 MHz and pressure of 0.2 Pa.*

rf cycle. It appears that as the rf bias potential is increased, the difference between the plasma potential and electrode potential becomes less and the low energy peak approaches zero. The high energy peak has more freedom since it occurs at the peak of the negative excursion of electrode potential, far from the plasma potential. Since the dc plasma potential is pushed more positive by the electrode potential an increase in the time averaged dc sheath potential is expected and clearly evident in the shifting to higher energies of the midpoint of the IED's with increasing rf bias potential.

Figure 5.16 shows the experimentally measured and calculated theoretical values of ΔE as a function of rf bias potential for capacitively coupled and

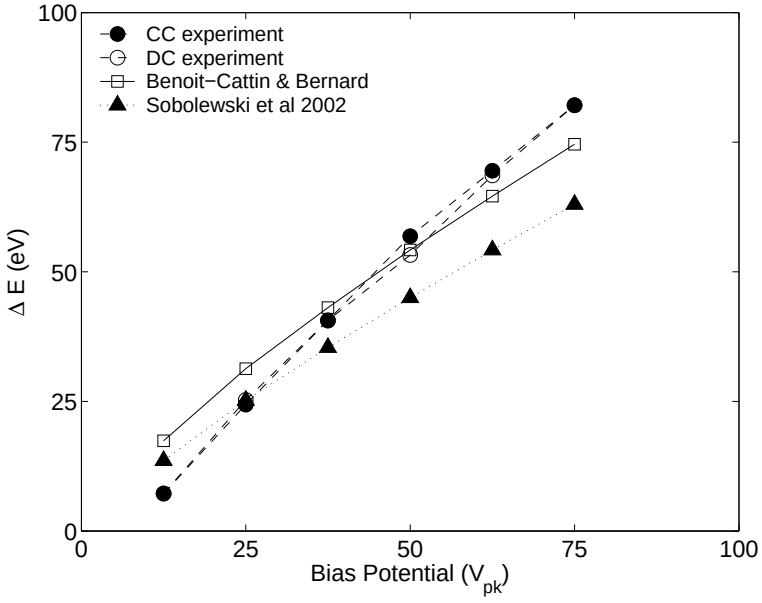

Figure 5.16: *Ar ΔE as a function of rf bias potential for capacitively coupled [CC] and directly coupled [DC] biasing modes at a fixed power of 300 W at 2 MHz and pressure of 0.2 Pa. Calculated values of ΔE are also shown from eqn.(5.5) and eqn.(5.7) are also shown.*

directly coupled biased modes. It is found that the experiment is in good agreement with theory. This figure shows an approximately linear dependence of ΔE with rf bias potential as expected from equation (5.5) which gives $\Delta E \propto V_{pk-pk}$. Sobolewski [87] found an approximate solution for ΔE for all values of τ_{rf}/τ_i

$$\Delta E = eV_{pk-pk}\left[1+\left(\frac{2.25\tau_i}{T}\right)^2\right]^{-1/2}, \tag{5.7}$$

where T is the rf period. A similar analytical solution can also be found in reference [88]. The results of this calculation are also in good agreement with experiment.

Figure 5.17 shows an IED obtained in an argon discharge with the electrode biased in directly coupled mode. Under certain conditions, when a

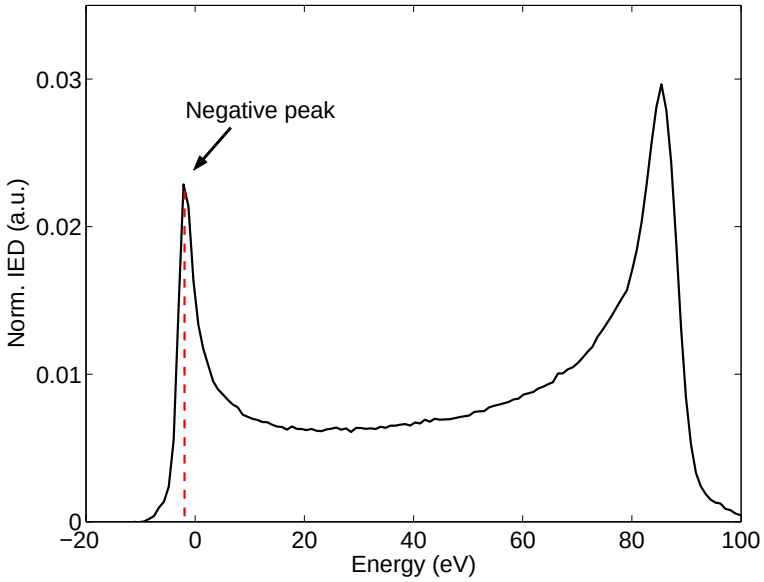

Figure 5.17: *Directly coupled biased electrode in an argon discharge [0.4 Pa, 500 W, 75 V_{pk}].*

large voltage amplitude is applied to the electrode, in directly coupled mode, the low energy peak becomes slightly negative. As discussed, the positive excursion of the electrode rf bias tends to push the plasma potential more positive to prevent rapid plasma electron loss. However it appears that in certain cases the electrode potential may become more positive than the plasma potential. In this case an ion that enters the sheath when the electrode is less positive than the plasma potential is collected when the electrode potential exceeds the plasma potential. When this happens the ion appears in the IED with negative energy as shown in figure 5.17. In a dynamic situation ion peaks at negative energies relative to the electrode potential are measurable and are caused by ion inertia.

5.4.4 Effects of frequency

Figure 5.18 shows IED's for a range of frequencies (0.5 - 20 MHz) taken at constant ICP power of 300 W, pressure 0.2 Pa and rf bias potential 37.5 V_{pk}. These measurements demonstrate how the distribution loses its broad, bimodal shape beyond a particular frequency when τ_i becomes significantly longer than τ_{rf}. Here, τ_i becomes single peaked at 20 MHz (τ_{rf} = 50 ns). Taking the time average sheath potential from the midpoint of the IED's, $\bar{V_s}$ = 42.6 V, then $\bar{s}$ = 2 mm, giving a value for τ_i = 418 ns that is significantly greater than τ_{rf}. In capacitively coupled mode, the distributions are all centered at 42.6 eV whereas in directly coupled mode the midpoints increase slightly at lower frequencies. Therefore the sheath potential remains constant as a function of frequency when capacitively coupled. Since the plasma potential is constant, the dc self bias of the electrode also remains constant. Again not surprising as the rf potential is fixed at 37.5 V_{pk}. For the directly coupled case, figure 5.18(b) shows that at low frequencies, the effect of the increased plasma potential is again seen in the low energy peak. The result is a smaller ΔE in directly coupled mode at low frequencies compared to capacitively coupled.

Figure 5.19 shows the experimentally measured and calculated theoretical values of ΔE as a function of frequency for capacitively coupled and directly coupled biased modes. There is excellent agreement between theory and experiment at frequencies greater than 2 MHz. Here, ΔE was calculated according to Benoit-Cattin's analytical model for a high frequency regime where $\tau_i/\tau_{rf} > 1$. In figure 5.19 it is clear that this model is no longer valid, for these experimental conditions, at frequencies below 2 MHz, when τ_i/τ_{rf} becomes less than 1.

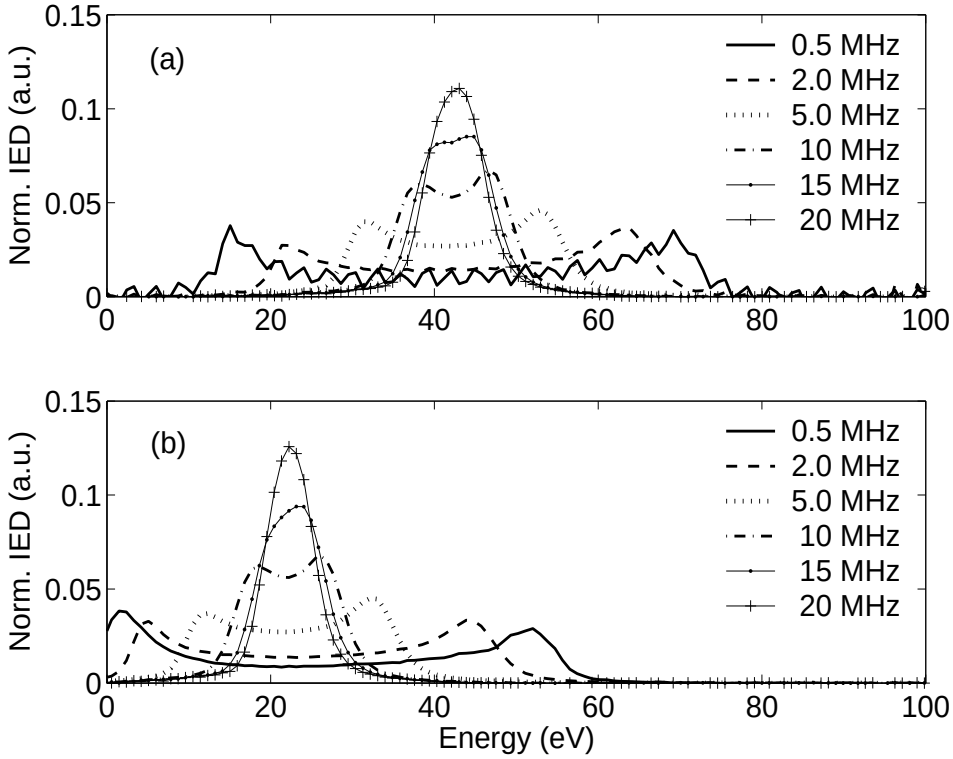

Figure 5.18: *Ar IED plots as a function of frequency: (a) capacitively coupled; (b) directly coupled, at a fixed bias of 37.5 V_{pk} at 300 W and pressure of 0.2 Pa.*

5.4.5 IEDs at an rf biased surface with two ion species

A discharge containing a mixture of helium and argon was used to investigate if the IED sampled at the capacitively coupled rf biased electrode could be mass resolved in a similar way to Edelberg and co-authors [68]. Since the ratio of the mass of argon ions to helium ions is ≈ 10 then the ratio of their transit times $\tau_{argon}/\tau_{helium}=\sqrt{M_{argon}/M_{helium}} \approx 3.2$ assuming that the time averaged sheath width and potential is the same for both ions. This indicates that the ΔE's for both ion types are sufficiently different to be resolved with the RFEA. Figure 5.20 shows IEDs taken in helium/argon mixture of 10:1. As expected two sets of energy peaks are detected, one for

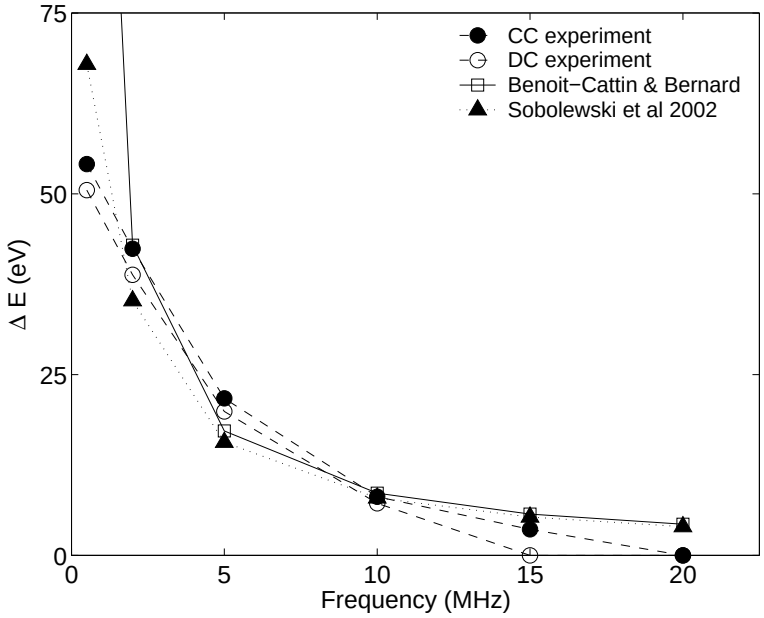

Figure 5.19: *Ar ΔE as a function of frequency for capacitively coupled [CC] and directly coupled [DC] biasing modes, at a fixed bias of 37.5 V_{pk} at 300 W and pressure of 0.2 Pa. ΔE values calculated from eqn.(5.5) and eqn.(5.7) are also shown.*

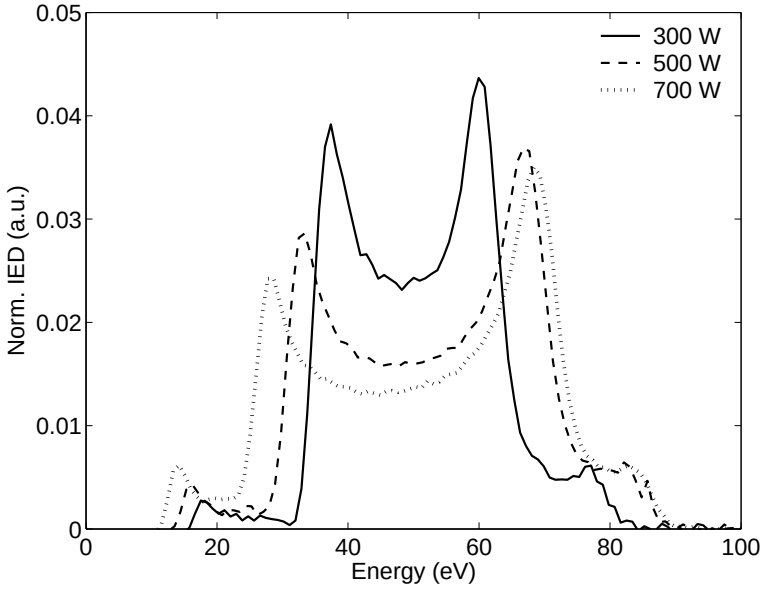

Figure 5.20: *He-Ar discharge: IED's as a function of ICP Power, at bias potential 100 V_{rf}, 5 MHz and 0.3 Pa.*

each ion species. The lighter helium energy peaks are significantly smaller due to the much higher ionization potential of helium. The ratio of helium ions to argon ions does increase with increasing power however. The ratio of $\Delta E_{helium}/\Delta E_{argon}$ is not constant as might be assumed from equation (5.5). However this model does not describe the variation of ΔE for all values of $\omega\tau_i$. The model described by equation (5.7) gives a better approximation of ΔE for all $\omega\tau_i$. Figure 5.21 gives $\Delta E/V_{pk-pk}$ as a function of $\omega\tau_i$ defined by equation (5.7). Also shown is the range of ΔE values for both argon and helium. Because of the non-linear relationship, ΔE for argon increases more rapidly with increasing power (decreasing ion transit time) than ΔE for helium as shown in figure 5.21.

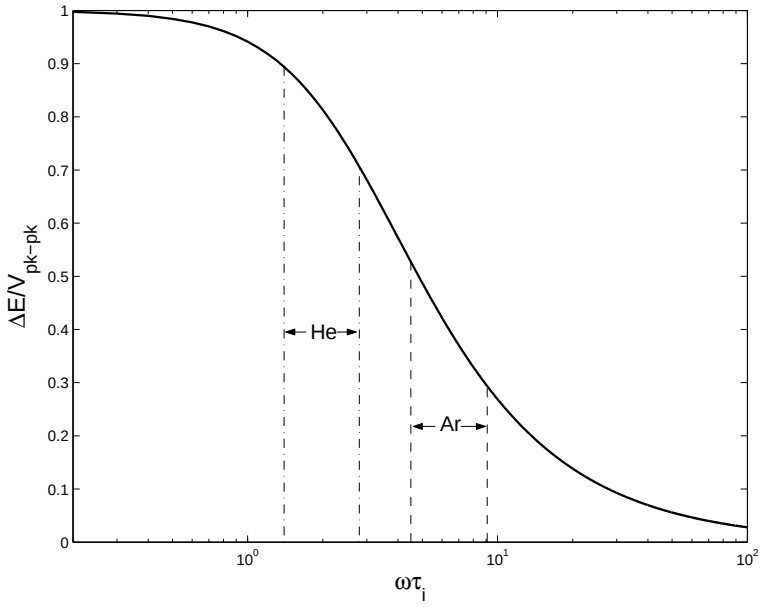

Figure 5.21: $\Delta E/V_{pk-pk}$ *as a function of* $\omega\tau_i$ *as defined by eqn.(5.7) for a He-Ar discharge.*

5.5 Summary

Ion energy distributions were investigated using a compact retarding field energy analyser in an expanding inductive discharge for a variety of conditions. The analyser was mounted on a downstream electrode in both capacitive and directly coupled modes. When the ion transit time is less than the time it takes to complete an rf cycle ($\tau_i \ll \tau_{rf}$), a bimodal ion energy distribution results. This is because the ion has time to respond to the instantaneous sheath potential rather than a time averaged potential.

This study investigates the ability of the RFEA to characterise the discharge as well as the capacitive sheath in front of the RFEA due to rf biasing of the electrode on which it is mounted.

The RFEA has been used to show the axial plasma potential variation in both argon and oxygen discharges. The existence of a double layer in

the oxygen discharge has been investigated in terms of discharge pressure and power. The characteristics of the double layer observed here will be the subject of future work in this discharge.

The comparison between the capacitively coupled and directly coupled rf bias potential gives insights into the sheath physics. On one hand the electrode develops a dc self bias to prevent rapid electron loss to the electrode and on the other, the electrode bias pushes the plasma potential more positive also to prevent significant electron loss. It has also been shown that under certain conditions, for directly coupled rf bias, an apparent negative ion energy peak is detected if the rf bias potential is sufficiently high. The origin of this peak is discussed. Experimentally measured ΔE for frequency and rf bias potential corresponds well with ΔE calculated from Benoit-Cattin's model as described by equation (5.5) except in the region where the ion transit time is less than the rf period. It has been shown that this model is not valid for frequencies where $\tau_i/\tau_{rf} < 1$. The model described by equation (5.7) is found to be in better agreement for all values of τ_i/τ_{rf}.

The RFEA is shown to be capable of mass resolution when a He-Ar discharge is used. Due to the different masses of the two ion species (and the nonlinear variation of ΔE with $\omega\tau_i$) ΔE for both species is found to vary differently as a function of power. From section 5.4.5 it has been shown that rf fields in the sheath allow mass discrimination.

CHAPTER 6

Conclusion

In conclusion to this thesis, a recap of the main results will be presented and where possible some suggestions for further work are made. The motivation behind this work was to investigate diagnostics for mass detection and extend the understanding of such in plasma discharges. Mass detection in any discharge cannot be accomplished by simple means. In commercial reactors where space for diagnostics is often limited, the installation of existing techniques can be difficult to achieve. The ability to measure ion abundance and behaviour in a process is of great importance as the ion plays a significant role in surface reactions.

6.1 Mass spectrometry and process control

Mass-spectrometers are complex instruments that are costly and often difficult to install in most situations. However the ability to produce a mass-spectrum of the gas phase is very advantageous. It is for this reason they are often used in analysis of etching systems, forensics and other analytical applications.

In chapter 2 closed loop control of ion flux and atomic oxygen density with a Langmuir probe and mass spectromter was described. Control was achieved by using two separate single input/single output (SISO) loops which were optimised experimentally (PID). The control model used for atomic oxygen density control combined the models for gas flow dynamics in the chamber (i.e. residence time and mass flow controller response time) through system identification with a simplified global model of atomic oxygen production. The global model used the chemical kinetic processes of dissociation of molecular oxygen and the recombination of atomic oxygen to describe the dynamics of atomic Oxygen production in the chamber. Given the response times of the SISO loops, it was found that the ion flux as measured by the Langmuir probe responded to changes in rf power almost instantaneously while response time of atomic oxygen density measured by the mass spectrometer to changes in O_2 flow rate was of the order of milliseconds.

Although real-time control was achieved, the signal from the mass spectrometer was somewhat unreliable. This was due to two major influences. Firstly, the electron emission filament in the mass spectrometer must be stabilised before taking measurements. This takes ~ 30 minutes so the emission must be ignited well in advance. This is not ideal for process control. Secondly, as a result of the discharge chamber heating up over time, drift in the measured ion current from the mass spectrometer was apparent during

testing. Accordingly, the mass spectrometer can be ruled out as a reliable sensor in process control.

6.2 The experimental set-up

The experimental reactor used to generate the discharge for the IMP and RFEA diagnostics was detailed in chapter 3. The plasma is ignited in a high density source region and subsequently expands into a much larger cylindrical chamber where various diagnostics are mounted. The feed gases used in the experiments are argon and oxygen of various combinations, at pressures of about 0.1 - 1.2 Pa. The rf power range used was $200 - 700$ W at a frequency of 13.56 MHz.

6.3 Ion mass probe

Following the failure of reliable measurements with the mass spectrometer in chapter 2 a novel ion mass probe was developed with a view to process control.

A novel electrostatic probe was described and tested. The probe consisted of a cylindrical Langmuir probe oriented at right angles to a planar probe. Each probe was dc biased independently. An investigation was carried out with the IMP on the ARIS II ICP chamber in pure Ar plasmas and Ar-O_2 mixtures under various plasma conditions i.e. pressures, powers and gas mixtures. This probe could be inserted directly into a plasma-processing chamber unlike the mass-spectrometer which requires a differential pumping system.

The idea is that biasing the planar probe will generate an ion flow along

the length of the cylindrical Langmuir probe. The ion trajectory in the sampling region will be dependent the ion mass and ion energy. Varying the relative bias between the planar probe and the Langmuir probe can alter this path resulting in a change in the collected ion currents at each probe. The rate of change of collected ion current with bias voltage is expected to vary with ion mass. The IMP shows that the rate of change of each IV trace from the cylindrical probe varies slightly with planar probe bias indicating a dependence of the slope on the average ion energy within the sampling region. Results show a change in slope but this is proven not to be important.

It was found that this probe could not differentiate ion mass by dc biasing alone. Simulations in SIMION confirmed this. In SIMION, when the KE of an ion is increased, the time-of-flight decreases for a fixed mass. If KE is fixed however, the time-of-flight increases for a fixed mass but the trajectory remains the same i.e. the same flight path is taken by ions of differing mass but a heavier ion will take longer to get there.

A possible method for measuring mass with the existing design configuration would be to use an rf bias on one of the probes. Ions entering the sample region would initially be accelerated by a negative bias on the Langmuir probe while an alternating bias on the planar probe would decelerate the ions according to their mass and the magnitude of the rf bias in much the same way a QMS filters ions of different m/z ratios.

6.4 RFEA

A retarding field energy analyser for investigating ion energy distributions (IEDs) at the sheath in an rf plasma is described in chapter 5. This investigation was performed with a remote rf driven electrode which was biased

independently of the ICP source in capacitive and direct coupling biasing modes. The electrode was driven at a separate frequency from the inductive source to avoid disturbance of the plasma. Power coupled through the resulting capacitive sheath in front of the electrode was analysed.

IEDs are dependent on sheath characteristics such as potential, sheath thickness and the number of rf cycles it takes for the ion to cross the sheath, τ_{ion}. Ions arriving at the surface of the analyser do so with a range of energies as a result of modulation by the time varying sheath potential. The shape of the IED was determined by τ_{ion}/τ_{rf} where τ_{rf} is the rf period.

The RFEA consists of a series of grids located behind a sampling aperture and terminated by a collector plate. The collector current for each bias step is recorded and an IED is obtained by taking the derivative of the collector current yielding the retarding potential characteristic.

When the ion transit time is less than the time it takes to complete an rf cycle ($\tau_i \ll \tau_{rf}$), a bimodal ion energy distribution results as the ion has time to respond to the instantaneous sheath potential rather than a time averaged potential.

A double layer was observed in an oxygen discharge and was investigated as a function of ICP power pressure.

The peak separation, ΔE, in a bimodal IED was measured as a function of frequency and rf bias potential and compared to ΔE calculated from the models developed by both Benoit-Cattin and Sobolewski as described by equation (5.5). Good agreement was found except in the region where the ion transit time is less than the rf period. It has been shown that this model is not valid for frequencies where $\tau_i/\tau_{rf} < 1$. The model described by equation (5.7) is found to be in better agreement for all values of τ_i/τ_{rf}.

The RFEA has shown potential for mass resolution when a He-Ar dis-

charge was used. Due to the different masses of the two ion species (and the nonlinear variation of ΔE with $\omega\tau_i$) ΔE for both species is found to vary differently as a function of power. From section 5.4.5 it has been shown that rf fields in the sheath allow mass discrimination.

The RFEA is an advantageous diagnostic in many ways. It has the ability to distinguish ions of differing mass and as it acts as a substrate it may not be as intrusive in the way a Langmuir probe is. Being able to monitor the ion energy distribution is invaluable in the plasma processing industry as ion energy plays a crucial role in modification of surface properties.

6.5 Future work

Future investigations of process control could include a more comprehensive process model as the current model may be an over-simplification of the actual kinetics in the discharge. In order to analyse these, a reliable mass detection system would be required. Techniques such as Laser Induced Fluorescence (LIF) could be employed to get absolute density of atomic oxygen and this in turn could be used to calibrate other sensors such as the mass-spectrometer.

Although the IMP probe failed, superimposing an rf pulse on a dc bias to one of the probes could alter the trajectory. As a first step, simulations should be carried out in SIMION to verify the concept.

Finally as the RFEA has shown real potential as a mass-detector from measurements taken in an Ar-He discharge this could be exploited by using a peak detection algorithm which cross references the IED peaks with a library of IEDs of various masses in a process control environment.

APPENDIX A

Process control

Flow rate experiments using analogue signals from the mass spectrometer

Initial testing of the controller was performed with the mass spectrometer and the response to changes in O_2 flow rate were monitored. O_2 flow was varied from 0 - 20 sccm with Ar flow fixed at 180 sccm and ICP power at 100 W as shown in figure A.1. V_O is measured directly whereas $V_{O_{2[difference]}}$ is the O signal inferred from the difference in the V_{O_2} signal when the plasma is on and the V_{O_2} signal with the plasma off. The plots obtained for V_O and [$V_{O_{2_{off}}}$ - $V_{O_{2_{on}}}$] v's a step in flow, are not the same. $f[V_{O_{2_{off}}}$ - $V_{O_{2_{on}}}]$ should equal V_O as a result of dissociation when the plasma is ignited. The difference plot is more linear than that of V_O and there is an offset between the two plots which increases with flow rate. Atomic oxygen resulting from dissociation of the neutral gas is in the mass spectrometer together with that

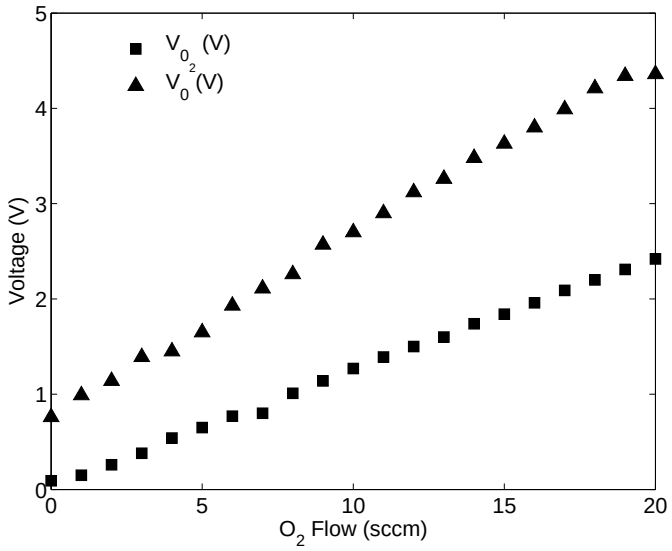

Figure A.1: *Voltage response for a stepped increase in molecular oxygen flow rate from 0-20 sccm, at ICP power 100 W and a fixed Ar flow rate of 180 sccm.*

coming from the discharge would yield a greater signal than the difference of the molecular signal alone (see figure A.1).

Residence time as a function of gate valve position

Figure A.2 shows the estimated residence times as a function of gate valve position.

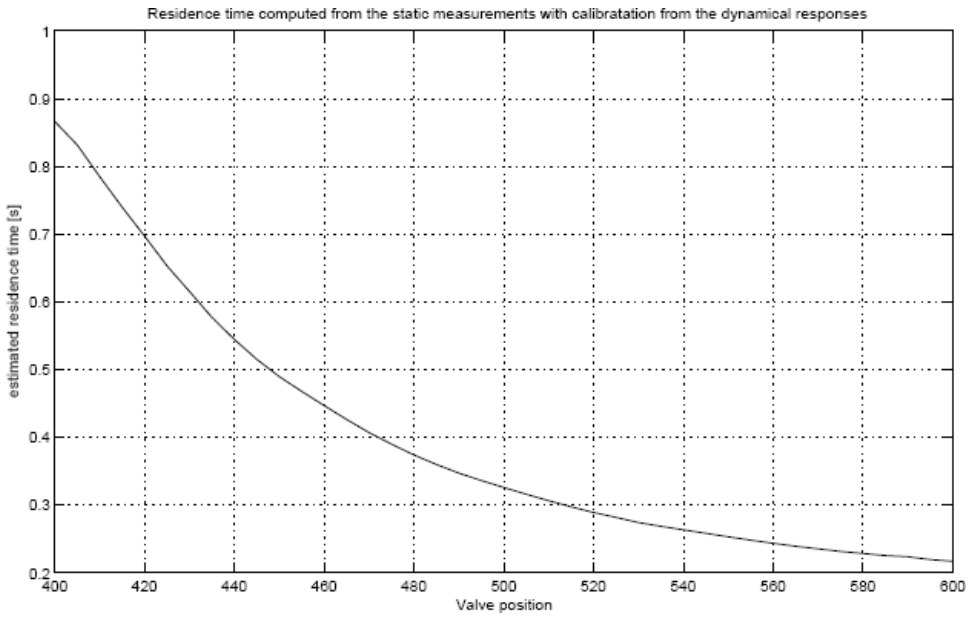

Figure A.2: *Residence times estimated from the static and dynamic measurements.*

APPENDIX B

RFEA models

B.1 Peak separation (ΔE) models

Edelberg *et al* Model [68]

$$\Delta E = \left(\frac{4eV_{rf}}{3ef_{rf}d_s} \right) \tag{B.1}$$

Benoit-Cattin and Bernard's Model [81]

$$\Delta E = \left(\frac{8e\tilde{V}_s}{3\omega d_s} \right) \left(\frac{2e\bar{V}_s}{m_i} \right)^{1/2} = \frac{3e\tilde{V}_s}{\pi} \left(\frac{\tau_{rf}}{\tau_i} \right) \tag{B.2}$$

Kawamura *et al* Model [71]

$$\Delta E = \left(\frac{8e\tilde{V}_s}{3\omega d_s} \right) \left(\frac{2e\bar{V}_s}{m_i} \right)^{1/2} = \frac{4e\tilde{V}_s}{\pi} \left(\frac{\tau_{rf}}{\tau_i} \right) \tag{B.3}$$

Sobolewski *et al* Model [87]

$$\Delta E = eV_{pp}\left[1+\left(\frac{2.25\tau_i}{T}\right)^2\right]^{-1/2} \tag{B.4}$$

Bibliography

[1] W. Crookes. On a fourth state of matter. *Proc. R. Soc. London*, 30:469, 1879-1880.

[2] I. Langmuir and H. M. Mott-Smith. Studies of Electric Discharges in Gases at Low Pressures. *Gen. Elec. Rev.*, 27:449, 1924.

[3] W. M. Greene, M. A. Hartley, and D. W. Hess. Ion transit through capacitively coupled ar sheaths: Ion current and energy distribution. *J. Appl. Phys.*, 63(5):1367–1371, 1988.

[4] P. C. Boyle, J. Robiche, and M. M. Turner. Modelling of the dual frequency capacitive sheath in the intermediate pressure range. *J. Phys. D: Appl. Phys.*, 37(10):1451–1458, 2004.

[5] Y. P. Raizer, M. N. Shneider, and N. A. Yatsenko. *Radio-frequency capacitive discharges*. CRC Press, Boca Raton, 1995.

[6] N. A. Krall and A. W. Trivelpiece. *Principle Of Plasma Physics*.

McGraw-Hill Kogakusha Ltd, Tokyo, International Student edition, 1973.

[7] M. A. Lieberman and A. J. Lichtenberg. *Principles of Plasma Discharges and Materials Processing.* Wiley, New Jersey, second edition, 2005.

[8] M. A. Lieberman. Analytical solution for capacitive rf sheath. *IEEE Trans. Plasma Sci.*, 16(6):638–644, 1988.

[9] D. Gahan. *Radio Frequency Discharge Power Measurement with emphasis on Collisionless Electron Heating in Capactive Sheaths.* PhD thesis, Physical Science, Dublin City University, 2006.

[10] I. D. Sudit and R. C. Woods. A study of the accuracy of various langmuir probe theories. *J. Appl. Phys.*, 76:4488–4498, 1994.

[11] J. G. Laframboise. Theory of spherical and cylindrical probe langmuir probes in a collisionless maxwellian plasma at rest. Technical Report 100, Institute of Aerospace Studies, Toronto, Canada, 1966.

[12] C. Steinbrüchel. A new method for analyzing langmuir probe data and the determination of ion densities and etch yields in an etching plasma. *J. Vac. Sci. Technol. A*, 8:1663, 1990.

[13] M. B. Hopkins. Langmuir probe measurements in the gaseous electronics conference rf reference cell. *J. Res. Natl. Inst. Stand. Technol.*, 100(4): 415–425, July-August 1995.

[14] M. B. Hopkins and W. G. Graham. Langmuir probe technique for plasma parameter measurement in a medium density discharge. *Rev. Sci. Instrum.*, 57:2210–2217, 1986.

[15] V. Pletnev and J. G. Laframboise. Current collection by a cylindrical probe in a partly ionized collisional plasma. *Phys. Plasmas*, 13:0735031, 2006.

[16] S. Linnane. *Investigation of Phase-Resolved Characteristics using an Uncompensated Langmuir Probe in Radio-Frequency Plasmas.* PhD thesis, Physical Science, Dublin City University, 2007.

[17] J. T. Gudmundsson, A. M. Marakhtanov, K. K. Patel, V. P. Gopinath, and M. A. Lieberman. On the plsama parameters of a planar inductive oxygen discharge. *J. Phys. D: Appl. Phys.*

[18] V. I. Demidov, S. V. Ratynskaia, and K. Rypdal. Electric probes for plasmas: the link between theory and instrument. *Rev. Sci. Instrum.*, 73:3309–3439, 2002.

[19] L. Oksuz, F. Sobéron, and A. R. Ellingboe. Analysis of uncompensated langmuir probe characteristics in radio-frequency discharges revisited. *J. Appl. Phys.*, 99:013304, 2006.

[20] R. R. J. Gagné and A. Cantin. Investigation of an RF plasma with symmetrical and asymmetrical electrostatic probes. *J. Appl. Phys.*, 43: 2639–2647, 1972.

[21] F. F. Chen and J. P. Chang. *Lecture Notes on the Principals of Plasma Processing.* Plenum, New York, 2002.

[22] V. A. Godyak and R. B. Piejak. Probe measurements of the space potential in a radio frequency discharge. *J. Appl. Phys.*, 68(7):3157–3162, October 1990.

[23] I. D. Sudit and F. F. Chen. Rf compensated probes for high density discharges. *Plasma Sources Sci. Technol.*, 3:162–168, 1994.

[24] A. E. Wendt. Passive external rf filter for langmuir probes. *Rev. Sci. Instrum.*, 72:2926–2930, 2001.

[25] J. Scanlan. *Probes in rf plasma*. PhD thesis, Physical Science, Dublin City University, 1990.

[26] F. Jovic. *Process Control Systems*. Kogan Page Ltd, London, 1986.

[27] C. J. Spanos, H-F. Guo, A. Miller, and J. Levine-Parrill. Real-Time Statistical Process Control Using Tool Data. *IEEE Trans. Semiconductor Manufacturing*, 5(4), 1992.

[28] E. de Hoffmann and V. Stroobant. *Mass Spectrometry: Principles and Applications*. Wiley, England, second edition, 2001.

[29] I. Howe, D. H. Williams, and R. D. Bowen. *Mass Spectrometry: Principles and Applications*. McGraw-Hill, second edition, 1981.

[30] A. J. McCarter. *Plasmoids and the E-H Transition in an Inductively Coupled Discharge*. PhD thesis, Physical Science, Dublin City University, 2005.

[31] M. M. Turner and M. B. Hopkins. Anomalous sheath heating in a low-pressure rf discharge in nitrogen. *Phys. Rev. Lett.*, 69:3511–3514, December 1992.

[32] J. V. Scanlan and M. B. Hopkins. Langmuir probe measurements of the electron energy distribution function in radio-frequency plasmas. *J. Vac. Sci. Technol. A*, 10(4):1207–1211, 1992.

[33] R. Faulkner, F. Sobeón, A. McCarter, D. Gahan, S. Karkari, V. Milosavljevic, C. Hayden, A. Islyaikin, V. J. Law, M. B. Hopkins, B. Keville, P. Iordanov, S. Doherty, and J. V. Ringwood. Real time closed loop control of an Ar and Ar/O_2 plasma in an ICP. Poster: 59th Annual Gaseous Electronics Conference, October 10-13, Columbus, OHIO, abstract #SRP1.100002, 2006. URL `http://meetings.aps.org/Meeting/GEC06/Event/51051`.

[34] B. Keville, P. Iordanov, J. Ringwood, S. Doherty, R. Faulkner, F. Soberón, and A. McCarter. On the Modeling and Closed Loop Control of an Inductively Coupled Plasma Chamber. In *IFAC Workshop on Advanced Process Control for Semiconductor Manufacturing*, pages 56–61, 2006.

[35] P. Iordanov, B. Keville, J. Ringwood, S. Doherty, and R. Faulkner. On the Closed-loop Control of an Argon Plasma Process. In *Irish Signals and Systems Conference, 2006. IET*, pages 439–444.

[36] A. Gambier. Real-time Control Systems: A Tutorial. In *Proceedings of The 5th Asian Control Conference*, Melbourne, Australia, July 2004.

[37] P. W. Murrill. *Fundamentals of Process Control Theory*. Instrument Society of America, USA, second edition, 1991.

[38] W. H. Ray. *Advanced Process Control*. McGraw-Hill, USA, 1981.

[39] Mathworks Inc. xPC Target for use with real-time workshop, User's Guide, 2002.

[40] F. Sobéron. *Plasma Transport and Development of Plasma Kinetics in ARIS*. PhD thesis, Physical Science, Dublin City University, 2005.

[41] C. B. Freidhoff, R. M. Young, S. Siriam, T. T. Braggins, T. W. O'Keefe, J. D. Adam, H. C. Nathanson, R. R. A. Syms, T. J. Tate, M. M. Ahmad, S. Taylor, and J. Tunstall. Chemical sensing using nonoptical microelectromechanical systems. *J. Vac. Sci. Technol. A*, 17(4), 1999.

[42] T. Kotiaho. On-site Environmental and *In Situ* Process Analysis by Mass Spectrometry. *J. Mass. Spectrom.*, 31:1–15, 1996.

[43] E. R. Badman and R. G. Cooks. Miniature mass analyzers. *J. Mass. Spectrom.*, 35:659–671, 2000.

[44] S. Taylor, R. F. Tindall, and R. R. A. Syms. Silicon based quadrupole mass spectrometry using microelectromechanical systems. *J. Vac. Sci. Technol. B*, 19(2), 2001.

[45] S. Taylor, F. R. Gibson, and B. Srigengan. Miniature mass spectrometry: implications for monitoring of gas discharges. *Sens. Review*, 23(2):150–154, 2003.

[46] R. R. A. Syms, L. Michelutti, and M. M. Ahmad. Two-dimensional microfabricated electrostatic einzel lens. *Sens. Actuators A*, 107:285–295, 2003.

[47] P. G. Turner, A. Dugdale, I. S. Young, and S. Taylor. Portable mass spectrometry for measurement of anaesthetic agents and methane in respiratory gases. *Vet. J*, 177(1):36–44, 2008.

[48] B. Doggett, C. Budtz-Joergensen, J. G. Lunney, P. Sheerin, and M. M. Turner. Behaviour of a planar langmuir probe in a laser ablation plasma. *Appl. Surf. Sci.*, 247:134–138, 2005.

[49] P. Sheerin. *Modeling Supersonic Plasma Flow.* PhD thesis, Physical Science, Dublin City University, 2008.

[50] Impedans Ltd. Invent Ctr, DCU, Glasnevin, Dublin 9, Ireland. URL `www.impedans.com`.

[51] D. A. Dahl. Simion for the personal computer in reflection. *Int. J. Mass. Spectrom.*, 200:3–25, 2000.

[52] Scientific Instrument Services Inc. 1027 Old York Rd, Ringoes, NJ 08551. URL `www.simion.com`.

[53] M. W. Forbes, M. Sharifi, T. Croley, Z. Lausevic, and R. E. March. Simulation of Ion Trajectories in a Quadrupole Ion Trap: a Comparison of Three Simulation Programs. *J. Mass. Spectrom.*, 34:1219–1239, 1999.

[54] J. A. Simpson. Design of Retarding Field Energy Analyzers. *Rev. Sci. Instrum.*, 32(12):1283, 1961.

[55] J. W. Coburn and E. Kay. Positive-ion bombardment of substrates in rf diode glow discharge sputtering. *J. Appl. Phys.*, 43(12):4965–4971, 1972.

[56] K. Köhler, J. W. Coburn, D. E. Horne, E. Kay, and J. H. Keller. Plasma potentials of 13.56-mhz rf argon glow discharges in a planar system. *J. Appl. Phys.*, 57(1):59, 1985.

[57] K. Köhler, D. E. Horne, and J. W. Coburn. Frequency dependence of ion bombardment of grounded surfaces in rf argon glow discharges in a planar system. *J. Appl. Phys.*, 58(9):3350, 1985.

[58] A. D. Kuypers and H. J. Hopman. Ion energy measurement at the powered electrode in an rf discharge. *J. Appl. Phys.*, 63(6):1894–8, 1988.

[59] S G Ingram and N St J Braithwaite. Ion and electron energy analysis at a surface in an RF discharge. *J. Phys. D: Appl. Phys.*, 21:1496, 1988.

[60] S. G. Ingram and N. S. J. Braithwaite. rf modulation of positive-ion energies in low-pressure discharges. *J. Appl. Phys.*, 68(11):5519, 1990.

[61] A. D. Kuypers and H. J. Hopman. Measurment of ion energy distributions at the powered rf electrode in a variable magnetic field. *J. Appl. Phys.*, 67(3):1229–1240, 1990.

[62] J. Liu, G. L. Huppert, and H. H. Sawin. Ion bombardment in rf plasmas. *J. Appl. Phys.*, 68(8):3916–3934, 1990.

[63] J. R. Woodworth, M. E. Riley, D. C. Meister, B. P. Aragon, M. S. Le, and H. H. Sawin. Ion energy and angular distributions in inductively driven radio frequency discharges in argon. *J. Appl. Phys.*, 80(3):1304–1311, 1996.

[64] J. R. Woodworth, B. P. Aragon, and T. W. Hamilton. Effect of bumps on the wafer on ion distribution functions in high density argon and argon-chlorine discharges. *Appl. Phys. Lett.*, 70(15):1947–9, 1997.

[65] J. R. Woodworth, M. E. Riley, P. A. Miller, G. A. Hebner, and T. W. Hamilton. Ion energy and angular distributions in inductively driven radio frequency discharges in chlorine. *J. Appl. Phys.*, 81(9):5950–9, 1997.

[66] J. R. Woodworth, M. E. Riley, P. A. Miller, C. A. Nichols, and T. W. Hamilton. Ion distribution functions in inductively coupled radio frequency discharges in argon-chlorine mixtures. *J. Vac. Sci. Technol. A*, 15(6):3015–3023, 1997.

[67] J. R. Woodworth, I. C. Abraham, M. E. Riley, P. A. Miller, T. W. Hamilton, B. P. Aragon, R. J. Shul, and C. G. Wilson. Ion energy distributions at rf-biased wafer surfaces. *J. Vac. Sci. Technol. A*, 20(3): 873–886, 2002.

[68] E. A. Edelberg, A. J. Perry, N. Benjamin, and E. S. Aydil. Energy distribution of ions bombarding biased electrodes in high density plasma reactors. *J. Vac. Sci. Technol. A*, 17(2):506–516, 1999.

[69] E. A. Edelberg, A. J. Perry, N. Benjamin, and E. S. Aydil. Compact floating ion energy analyzer for measuring energy distributions of ions bombarding radio-frequency biased electrode surfaces. *Rev. Sci. Instrum.*, 70(6):2689–2698, 1999.

[70] E. A. Edelberg and E. S. Aydil. Modeling of the sheath and the energy distribution of ions bombarding rf-biased substrates in high density plasma reactors and comparison to experimental measurements. *J. Appl. Phys.*, 86(9):4799–4812, 1999.

[71] E. Kawamura, V. Vahedi, M. A. Lieberman, and C. K. Birdsall. Ion energy distributions in rf sheaths; review, analysis and simulation. *Plasma Sources Sci. Technol.*, 8:R45, 1999.

[72] D. Gahan, B. Dolinaj, and M. B. Hopkins. Retarding field analyzer for ion energy distribution measurements at a radio-frequency biased electrode. *Rev. Sci. Instrum.*, 79:033502, 2008.

[73] Y. Zou, Y. Cui, V. Yun, A. Valfells, R. A. Kishek, S. Bernal, P. G. OShea I. Haber, M. Reiser, and J. G. Wang. Compact high-resolution retarding field energy analyzer for space-charge-dominated electron beams. *Phys. Rev. STAB.*, 5:072801, 2002.

[74] E. Séran. Reconstruction of the ion plasma paramters from the current measurements: mathematical tool. *Annal. Geophys.*, 21:1159, 2003.

[75] C. Hayden, D. Gahan, and M. B. Hopkins. Ion energy distributions at a capacitively and directly coupled electrode immersed in a plasma generated by a remote source. *Plasma Sources Sci. Technol.* submitted Sept'08.

[76] D. Gahan, B. Dolinaj, C. Hayden, and M. B. Hopkins. Retarding field analyzer for ion energy distribution measurements through a radio-frequency or pulsed biased sheath. *Plasma Process. Polym.* submitted Aug'08.

[77] C. Charles. A review of recent laboratory double layer experiments. *Plasma Sources Sci. Technol.*, 16:R1, 2007.

[78] N. Plihon, C. S. Corr, and P. Chabert. Double layer formation in the expanding region of an inductively coupled electronegative plasma. *Appl. Phys. Lett.*, 86:091501, 2005.

[79] M. A. Lieberman, C. Charles, and R. W. Boswell. A theory for formation of a low pressure, current-free double layer. *J. Phys. D: Appl. Phys.*, 39: 3294, 2006.

[80] A. Meige, N. Plihon, G. J. M. Hagelaar, J. P. Boeuf, P. Chabert, and R. W. Boswell. Propagating double layers in electronegative plasmas. *Phys. Plasmas*, 14:053508, 2007.

[81] P. Benoit-Cattin and L. C. Bernard. Anomalies of the energy of positive ions extracted from high-frequency ion sources. a theoreticl study. *J. Appl. Phys.*, 39(12):5723–6, 1968.

[82] D. Gahan and M. B. Hopkins. Collisionless electron power absorption in capacitive radio-frequency plasma sheaths. *J. Appl. Phys.*, 100:043304, 2006.

[83] D. Gahan and F. Soberón. Effect of dc bias control on the power absorption in low-pressure, radio-frequency capacitive sheaths. *J. Appl. Phys.*, 101:023303, 2007.

[84] D. Gahan and M. B. Hopkins. Electrical characterisation of a capacitive rf plasma sheath. *Rev. Sci. Instrum.*, 78:016102, 2007.

[85] D. Gahan, B. Dolinaj, and M. B. Hopkins. Comparison of plasma parameters determined with a langmuir probe with a retarding field energy analyzer. *Plasma Sources Sci. Technol.*, 17:035026, 2008.

[86] M. Dimitrova, N. Djermanova, Z. Kissovski, S. Kolev, A. Shivarova, and T. Tsankov. Probe diagnostics of expanding plasmas at low gas pressure. *Plasma Process. Polym.*, 3:156, 2006.

[87] M. A. Sobolewski, Y. Wang, and A. Goyette. Measurements and modeling of ion energy distributions in high-density, radio-frequency biased cf4 discharges. *J. Appl. Phys.*, 91(10):6303, April 2002.

[88] C. Charles, A. W. Degeling, T. E. Sheridan, J. H. Harris, M. A. Lieberman, and R. W. Boswell. Absolute measurements and modeling of radio frequency electric fields using a retarding field energy anlayzer. *Phys. Plasmas*, 7:5232, 2000.